UNIVERSIDAD COMPLUTENSE DE MADRID
FACULTAD DE CIENCIAS FÍSICAS

MAGNETOELASTIC AND MAGNETOELECTRIC COUPLING IN EPITAXIAL ULTRA-THIN FILMS OF FERROMAGNETIC LA0.7CA0.3.MNO3FERROELECTRIC BATIO3

MEMORIA PARA OPTAR AL GRADO DE DOCTOR
PRESENTADA POR

Aurora Alberca Carretero

Bajo la dirección de los doctores

Mar García Hernández
Norbert Marcel Nemes

Madrid, 2014

MAGNETOELASTIC AND MAGNETOELECTRIC COUPLING IN EPITAXIAL ULTRA-THIN FILMS OF FERROMAGNETIC $La_{0.7}Ca_{0.3}MnO_3$ ON FERROELECTRIC $BaTiO_3$

Memoria presentada por

AURORA ALBERCA CARRETERO

Para optar al grado de Doctor en Ciencias Físicas por la

Universidad Complutense de Madrid

Dirigida por

MAR GARCÍA HERNANDEZ

NORBERT MARCEL NEMES

Madrid, Junio de 2013

TABLE OF CONTENTS

CHAPTER 1
INTRODUCTION

We live in an information based society made possible by technology that progresses with nanoscale fabrication methods. The development of new solid-state devices to meet the increasing demands on miniaturization and functionalities keeps material science in constant growth. In particular, improving storage densities for the relentlessly increasing data receives much attention from the scientific community. In turn, advances in nanotechnology trigger the enthusiasm for unexplored opportunities of theoretical and experimental physicists with both academic and industrial purposes in mind. Spintronics, a new field that brings together basic physics, materials science and nano-science, births new technologies capable to improve, among others, the current strategies for low consumption random access memories (RAM).

In this chapter, we contextualize this thesis in the Spintronics scenario and describe some of the most important challenges met by Spintronics in recent years. Following the improvements in data storage and RAM applications as guidelines we describe the evolution of Spintronics from the use of magnetic fields and spin-polarized currents in the early years to the current approaches related to multiferroic materials and magnetoelectric coupling. At the end of the chapter the main motivations of this work are presented as well as the choice of the materials and the contribution of this thesis to the field of Spintronics and materials science.

SPINTRONICS

Spintronics is currently one of the most exciting and active research areas in condensed-matter physics [Sinova2012, Steil2013, Fert2013, Xue2013]. It is based on the control of the electron spins in addition to charges – hence, the name spin-transport electronics. Important applications of Spintronics run from spin field effect transistors to spin quantum computers. In particular, a highly successful result of Spintronics is the fabrication of devices such as read-heads that enable high density information management, with more Tbytes each year at lower cost. The key for novel Spintronics applications takes advantage of the exotic behavior appearing in nanomagnetic systems at ultrafast time-scales or under non-equilibrium configurations [Smart2011, Winpenny2013]. The success of giant magnetoresistance (GMR) and its broad application and commercial impact on information technology – which awarded Albert Fert and Peter Grünberg the Nobel Prize in Physics in 2007 [Fert2008, Grünberg2008] – boosted the interest of the scientific community in these systems over the past two decades. The discovery of GMR in 1988 is considered the starting point of Spintronics.

Recent discoveries in Spintronics have enabled the control and manipulation of magnetic moments in diverse manners [Bader2010]. Figure 1 shows some of the most important of these approaches classified according to the variable used to control and manipulate the spins in a magnetic specimen, that is, photonic, magnetic or electric fields as well as spin-polarized currents. In processes such as tunnelling magnetoresistance (TMR), spin transfer torque (STT) [Tay2013, Locatelli2013, Saidaoui2013, Stiles2002] and devices such as racetrack memories [Trinh2013, Parkin2008, Chappert2007], control is achieved through spin-polarized currents. Other control mechanisms are those found in topological insulators [Winpenny2013, Hasan2010, Cava2013,

Moore2010, Jozwiak2013] and quantum spin Hall Effect (QSHE) [Zhou2012, Qi2010, Kane2005] where photonic and magnetic fields are used. The work in thesis deals with questions arising in TMR strategies.

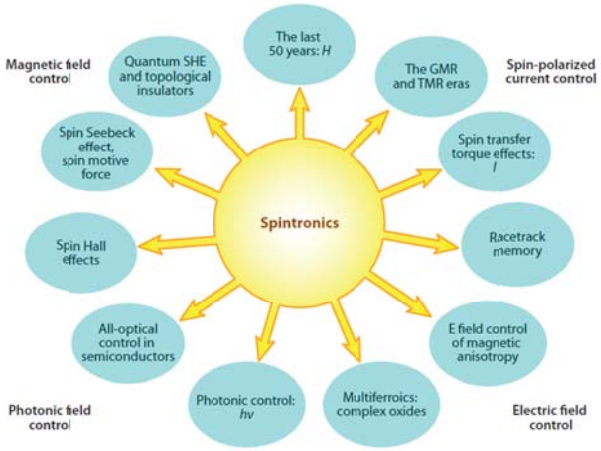

Fig.1. Diagram showing the different approaches to Spintronics. Adapted from Ref. [Parkin2008]

A major application of Spintronics is the development of new memory architectures that render improved non-volatile Random Access Memories (RAM). Seeking the "ultimate memory" [Scott2006] that incorporates all the desired properties (endurance, size, speed, energy consumption…), several types of RAM have been proposed ranging from Ferroelectric RAM (FeRAM) to Magnetoresistive RAM (MRAM). In a broad sense, FeRAMS use a ferroelectric thin film as a capacitor for storing data and MRAMS exploit the large magnetoresistance effect to write bits as two different resistance states (high and low resistance).

Just a short a decade after the discovery of GMR, IBM already introduced in 1997 the first GMR Hard-disk read-head. Soon afterwards, new and improved devices based on GMR and TMR were designed. New devices appeared, such as Spin-Valves and Magnetic Tunnel Junctions (MTJ) that required the control of magnetization using reasonably small magnetic fields. Spin-Valves consist of two or more conducting magnetic materials, whose electrical resistance can change between two values depending on the relative alignment of the magnetization in the two layers (see Fig. 2). One of the magnetic layers is "pinned" –for example to an antiferromagnetic (AF) layer– and the other "free" layer is tuned applying a small magnetic field. In an MJT, the pinned and free layers are separated by a very thin insulating layer. The tunneling resistance is modulated by a magnetic field in the same way as the resistance of a spin valve is. In a more recent method, the magnetic fields used to tune the "free" layer were substituted by spin-polarized currents. This can be achieved in devices based on the Spin Transfer Torque (STT) effect where the angular momentum of the spin polarized current is transferred to the "free" layer, thus changing its orientation (see Fig. 2 and figure caption).

Today, the practical problem of memory devices is addressed (among other possibilities) using electric fields to control and modify magnetic orders with the idea of writing data electrically and reading it magnetically in a single multiferroic bit [Dong2013, Ghidini2013, Evans2013, Tokunaga2012, Spaldin2010] (multiferroic materials will be described in the next section). This can be achieved, for example, by modifying the magnetic anisotropy [Parkin2008] of Fe-based structures or exploiting the influence between coupled ferroic orders [Bibes2012] in oxide based multiferroic heterostructures. The advantage of this new approach compared to magnetic based RAM is the considerable reduction of power consumption in the process of magnetic switching [Parkin2008, Bea2008]. In addition, the non-local character of magnetic fields used in earlier devices could affect surrounding memory bits, too. The use of electric fields – generated with voltages which are local – removes this disadvantage [Parkin2008].

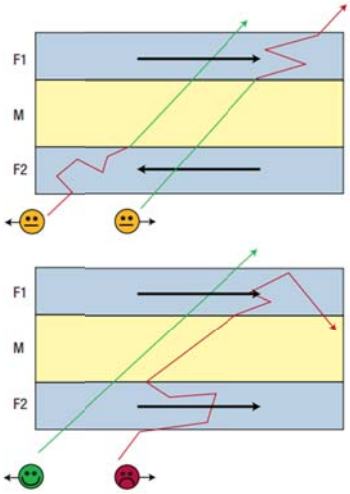

Fig.2. Simple spin-valve structure consisting in two magnetic layers (F1 and F2) separated by a non-magnetic metal (M) in two resistance states. When F1 and F2 are aligned antiparallel (upper figure), electrons of both polarization are scattered giving rise to the high resistance state, when they are aligned parallel (lower figure) only one of the polarizations is scattered providing the low resistance state. Figure adapted from Ref. [Chappert2007].

The promising applications of multiferroic materials extend to the design of memories based in four logic states [Fert2008, Gajek2007, Bibes2008, Velev2008]. Figure 3 shows a way to encode quaternary information in a device where ferromagnetic and ferroelectric orders are coupled. In these devices, four states of resistance can be obtained by combination of the parallel and antiparallel alignment the magnetic layers of a MTJ and the two possible polarization states of a ferroelectric barrier.

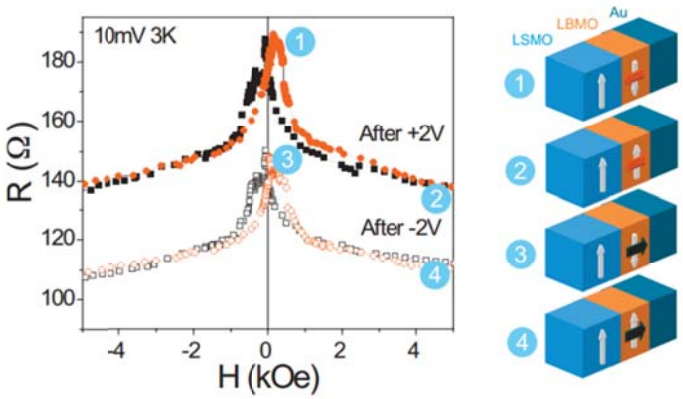

Fig.3. Four states logic in a device consisting in a MTJ with a ferroelectric barrier. In this device a biferroic thin film ($La_{0.1}Bi_{0.9}MnO_3$) was used as the ferroelectric barrier between the non-magnetic gold electrode and the $La_{0.66}Sr_{0.33}MnO_3$ magnetic thin film. Figure adapted from Refs. [Fert2008, Gajek2007].

Also, the successful fabrication of high-performance heterostructures (thin films) with high spatial coherence, the understanding of the new physic phenomena that result from structural changes – compared with their bulk counterparts – and interface effects enhanced with the reduction of device size [Ramesh2007] have had a major impact on the evolution of this field. In addition, strongly correlated materials, such as transition metal oxides, become convenient due to their versatility in magnetic, superconducting or other ferroic orders [Bibes2007]. An example of this is the possibility of using Colossal Magnetoresistance (CMR) effect, observed in manganite oxides, in data storage devices. In this sense, finding the appropriate materials and

heterostructures is one main motivation. Advancing from the single layer structure to more complex systems, say, multilayers or nano-patterned structures, these heterostructures are the focus of current strategies.

ELECTRIC FIELD CONTROL OF MAGNETIZATION

Briefly, multiferroics are materials exhibiting two or more primary ferroic orders [Spaldin2005, Eerenstein2006, Bea2008, Wang2009]. The four basic primary ferroic order parameters are ferromagnetism, ferroelectricity, ferroelasticity and ferrotoroidicity. In a ferromagnetic material, magnetization (M) can be modified by applying a magnetic field (H). Similarly, in a ferroelectric material, polarization (P) can be affected by an electric field (E), whereas in a ferroelastic material a stress (σ) is responsible for a change of strain (ε). In multiferroic materials exhibiting two of these order parameters in the same phase, more complicated interactions can appear through linear and quadratic couplings in the order parameters (see Fig. 4).

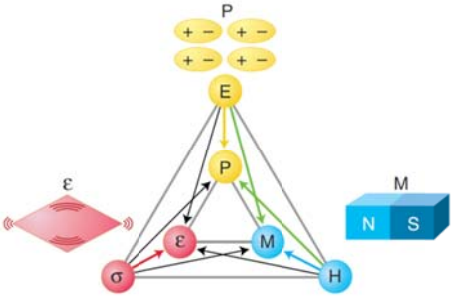

Fig.4. Phase control in multiferroics. In a "ferroic" exhibiting only one order parameter the electric field E, the magnetic field H or the stress σ control the polarization P, the magnetization M and the strain ε, to produce ferroelectricity, ferromagnetism and ferroelasticity, respectively. In a multiferroic, exhibiting two of these orders in the same phase, additional interactions occur. Figure adapted from Ref. [Spaldin2010].

One of the canonical multiferroic materials is $BiFeO_3$ [Wang2003, Catalan2009] which is ferroelectric and antiferromagnetic below 640 K. The room-temperature phase of $BiFeO_3$ is rhombohedral belonging to the space group R3c and has perovskite structure (see Fig. 5). The large electrical polarization in $BiFeO_3$ epitaxial thin films coupled to small magnetization originated the study of magnetoelectric multiferroics as an alternative to only magnetic RAMs [Zhao2006, Lebeugle2007].

Although $BiFeO_3$ is a great example of intrinsic multiferroic materials, these are very rare in nature. The limited availability of intrinsic multiferroics amongst transition-metal oxides was studied in Ref. [Hill2000, Wang2009]. Essentially, the incompatibility between ferroelectric and ferromagnetic orders in oxides seems to be the origin of this "rarity": a ferroelectric material, by definition, must be an insulator. However, many ferromagnets are often metallic (when ferromagnetic). In addition, microscopic factors, such as structural distortions (Jahn-Teller distortions), seem to be particularly unfavorable for the coexistence of ferroic orders in strongly correlated materials, (for example, in manganites, see Chapter 2). This is probably the most restricting factor: Common perovskite oxide ferroelectric materials have a formal charge corresponding to the d^0 electron; this favors the distortion between positive and negative charges that gives rise to the electric dipole moment and, thus, to ferroelectricity. However, as soon as the d shell is partially occupied (partially doped manganites), for example the tendency to develop a distortion that removes the center of symmetry is eliminated. Therefore, quite often, magnetism and conventional ferroelectricity are incompatible [Spaldin2010]. For this reason, the most extended strategy in the design of multiferroic based devices is combining ferroelectric and ferromagnetic materials in hybrid heterostructures.

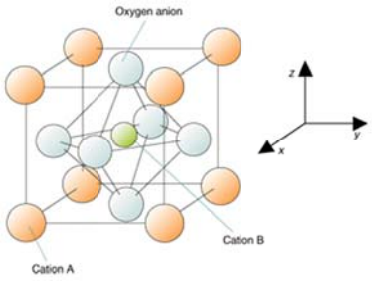

Fig.5. Perovskite structure ABO_3. In the ideal cubic-symmetry, cation B is surrounded by an octahedron of oxygen and A cations occupy the vertices of the cube.

The control of magnetic properties of materials via the application of an electric field is known as (inverse) magnetoelectric coupling [Bichurin2003, Fiebig2005]. Thermodynamically, the magnetoelectric effect in a single-phase crystal is traditionally described in the context of Landau theory by writing the free energy F of the system as a power series of the applied magnetic field **H** and the applied electric field **E** as follows:

$$-F(E,H) = \frac{1}{2}\varepsilon_0\varepsilon_{ij}E_iE_j + \frac{1}{2}\mu_0\mu_{ij}H_iH_j + \alpha_{ij}E_iH_j + \frac{1}{2}\beta_{ijk}E_iH_jH_k + \frac{1}{2}\gamma_{ijk}H_iE_jE_k + \ldots \quad [1]$$

The first term describes the electrical response to an electric field, where the permittivity of free space is denoted as ε_0 and the relative permittivity $\varepsilon_{ij}(T)$ is a second-rank tensor, function of the temperature T. Similarly, the magnetic response contribution corresponds to the second term, where μ_0 is the permeability of free space and $\mu_{ij}(T)$ is the relative permeability. The third term describes linear magnetoelectric coupling, with coupling constant $\alpha_{ij}(T)$; the third-rank tensors $\beta_{ijk}(T)$ and $\gamma_{ijk}(T)$ represent quadratic magnetoelectric coefficients [Fiebig2005, Wang2009].

Differentiating F with respect to E_i and then setting $E_i = 0$ allows us to obtain the electric polarization as a function of the magnetic field, $P_i(H_j)$, (direct magnetoelectric effect):

$$P_i = \alpha_{ij}H_j + \frac{1}{2}\beta_{ijk}H_jH_k + \ldots \quad [2]$$

Similarly, differentiating with respect to H_i and setting $H_i = 0$, the expression for $M_i(E_j)$, (inverse magnetoelectric effect) is obtained:

$$\mu_0 M_i = \alpha_{ij}E_j + \frac{1}{2}\gamma_{ijk}E_jE_k + \ldots \quad [3]$$

Values reported in literature for the magnetoelectric coupling constants α_{ij} are of the order of 10^{-9}-10^{-7} s/m [Eerenstein2007, Thiele2007, Vaz2010]. Finding heterostructures with higher coupling constants is essential to improve the functionality of new devices based on Multiferroics.

We detail two mechanisms that may render magnetoelectric coupling in heterostructures: strain induced coupling in two-phase composites and electronically-driven interface magnetoelectric effects.

STRAIN MEDIATED MAGNETOELECTRIC EFFECT

The strain mediated magnetoelectric effect usually involves heterostructures consisting of a magnetoelastic and a piezoelectric material, where the magnetoelastic properties of a thin ferromagnetic layer or composite are

modified through the piezoelectric effect of a ferroelectric substrate. In general, combining piezomagnetism, piezoelectricity (linear), magnetostriction or electrostriction (cuadratic), artificial magnetoelectric materials can be fabricated [Vaz2010, Eerenstein2006, Livesey2011]. Several examples of these systems are nano-patterned heterostructures [Lu2011], composites [Wang2011] or epitaxial multilayers [Li2009, Eerenstein2007, Moya2012, Thiele2007, Vaz2012].

As far as ferromagnetic layers on ferroelectric substrates are concerned, changes in the magnetism of the ferromagnetic layer are mediated by the piezoelectric effect of the substrate via magnetoelastic coupling (ME). Magnetoelasticity is a phenomenon in which the dimensions of a magnetic material – and its preferred direction of magnetization – change due to the applied stress.

Magnetoelectric coupling at the interface of a ferromagnetic/ferroelectric heterostructure may also involve changes in the magnetocrystalline anisotropy near the interface when an electric field is applied [Wang2013]. Since the magnetic anisotropy determines the preferential direction of the magnetization in a magnetic thin film, this phenomenon may allow switching the magnetic moment and, therefore, is interesting for applications.

Interface Reconstruction

Interfacial electronic reconstruction based magnetoelectric coupling occurs at the ferromagnet/insulator interface due to spin-dependent screening: at the interface, an applied electric field induces accumulation or depletion of spin-polarized electrons resulting in a change of the interface magnetization [Tsymbal]. Interface magnetoelectric effects may involve magnetic reconstruction, i.e. a change in how magnetic moments are ordered near the interface, leading to a significant change of the interface magnetization [Tsymbal2009, Dagotto2012, Sohrab2012].

Good examples of the interface reconstruction-based mechanism of magnetoelectric effect are $Fe/BaTiO_3$ or $Co/BaTiO_3$ multilayers [Bea2008]. In these heterostructures, the bond fluctuation at the ferroelectric/ferromagnetic interface modulates the interfacial magnetization upon polarization reversal due to the interface bonding sensitivity to the atomic displacements there.

MOTIVATION AND AIMS OF THIS THESIS

From a practical point of view, the study of new suitable materials and heterostructures for multiferroic systems is of great relevance [Wu2013, Streubel2013, Lahtinen2012, Perks2012], and the strategy of electrically modifying magnetic orders emerges as a good alternative for the needs of modern information technologies.

Presently, many of the actively studied multiferroic heterostructures combine different types of complex oxides, which comprise two or more transition metal cations (usually 3d) and oxygen [Spaldin2010, Bea2008, Bibes2007]. The interest in these materials resides in the highly localized electrons that lead to the so-called strong correlation physics, which, in consequence, lead to unusual magnetic and electronic phenomena, such as metal insulator transitions, superconductivity or half-metallicity, often used in technological applications.

In this thesis, we studied a particular case of multiferroic heterostructures consisting of a ferromagnetic thin film layer ($La_{0.7}Ca_{0.3}MnO_3$ manganite) grown on ferroelectric $BaTiO_3$ substrates. The choice of these materials is motivated by their similar perovskite structure (see Fig. 5) and lattice parameters, which allows epitaxial growth and, more importantly, by their intrinsic properties. Optimal doped manganite $La_{0.7}Ca_{0.3}MnO_3$ is a strongly correlated compound well known for exhibiting CMR effect. This manganite is particularly prone to phase separation [Dagotto2003] and, therefore, susceptible of being strongly affected by substrate strain and

ferroelectric polarization. On the other hand, $BaTiO_3$ is one of the most studied ferroelectric materials of the perovskite class [Shirane1993]. Bulk properties of $La_{0.7}Ca_{0.3}MnO_3$ and $BaTiO_3$ as well as the ferromagnetic and ferroelectric properties in these compounds will be reviewed in Chapter 2.

In thin film geometry, interfacial electronic reconstruction and strain mediated processes (magnetoelastic coupling) appearing between substrate and thin film (or between thin films in multilayers) drastically modifies the compound properties. As discussed before, taking advantage of these processes is the key in the design of new devices. Whether these effects alter the magnetic order of the whole thin film (magnetic anisotropy, electronic transport…) or are localized in the interface (interface reconstruction), the starting point is to study the properties of one single interface, and, later, the implementation in multilayered or more complex nano-patterned devices.

An important aim of this thesis is to explore the interfacial effects in $La_{0.7}Ca_{0.3}MnO_3$//$BaTiO_3$ ultra-thin films that arise from the interaction between the ferroelectric and magnetic orders at the discontinuity between thin film and substrate. In $La_{0.7}Ca_{0.3}MnO_3$//$BaTiO_3$, the effect of the substrate is prominent and the way to enhance the observation of interfacial effects is through reducing the thickness of the thin film. The other way is to explore the magnetoelectric effect in $La_{0.7}Ca_{0.3}MnO_3$//$BaTiO_3$ by modifying the magnetic phase via the polarization of the ferroelectric (electric field control of magnetization). The results shown throughout this thesis reveal new, unexpected, physics that are ultimately related to strong magnetoelastic coupling between substrate and thin film. This magnetoelastic coupling is also responsible for the strong magnetoelectric effects observed in $La_{0.7}Ca_{0.3}MnO_3$//$BaTiO_3$ systems.

THESIS OUTLINE

- Chapter 2: An introduction to the main properties of $La_{0.7}Ca_{0.3}MnO_3$ and $BaTiO_3$ bulk compounds is given, highlighting those characteristics relevant to the rest of the thesis.
- Chapter 3: The experimental techniques used throughout the thesis is reviewed
- Chapter 4: The structural characterization of $La_{0.7}Ca_{0.3}MnO_3$//$BaTiO_3$ is discussed. The presence of ferroelectric domains and surface corrugation in $BaTiO_3$ bulk results in enhanced interface effects with the ferromagnetic thin film. X-ray diffraction and atomic force microscope topography techniques reveal the characteristics of $La_{0.7}Ca_{0.3}MnO_3$//$BaTiO_3$ heterostructures.
- Chapter 5: The magnetic properties of $La_{0.7}Ca_{0.3}MnO_3$//$BaTiO_3$ are presented. Magnetism suggests strong magnetoelastic coupling in $La_{0.7}Ca_{0.3}MnO_3$//$BaTiO_3$ systems and magnetic granularity. Matteucci magnetic loops observed in $La_{0.7}Ca_{0.3}MnO_3$//$BaTiO_3$ in ultra-thin films are described in this chapter.
- Chapter 6: In this chapter we study transport properties in $La_{0.7}Ca_{0.3}MnO_3$//$BaTiO_3$ heterostructures. Magnetotransport, electro-resistance and poling effect of the substrate are studied. Hints of an antiferromagnetic phase near the interface with $BaTiO_3$ are given.
- Chapter 7: This chapter deals with magnetoelastic coupling in $La_{0.7}Ca_{0.3}MnO_3$//$BaTiO_3$. Here, a two-layer model to describe ferromagnetic resonance experiments is proposed. This model is supported by Polarized Neutron Reflectometry results.

- Chapter 8: Finally, magnetoelectric coupling in $La_{0.7}Ca_{0.3}MnO_3$ thin films on poled and unpoled $BaTiO_3$ substrates is studied.

REFERENCES

[Bader2010] Bader, S. D., and S. S. P. Parkin. "Spintronics." Annu. Rev. Condens. Matter Phys. 1.1 (2010): 71-88.

[Bea2008] Bea, H., et al. "Spintronics with multiferroics." Journal of Physics: Condensed Matter 20.43 (2008): 434221.

[Bibes2007] M. Bibes and Agnes Barthelemy. "Oxide spintronics." Electron Devices, IEEE Transactions on 54.5 (2007): 1003-1023.

[Bibes2008] Bibes, Manuel, and Agnès Barthélémy. "Multiferroics: Towards a magnetoelectric memory." Nature materials 7.6 (2008): 425-426.

[Bibes2012] M. Bibes, Nature Mat, 11, 354 (2012)

[Bichurin2003] Bichurin, M. I., V. M. Petrov, and G. Srinivasan. "Theory of low-frequency magnetoelectric coupling in magnetostrictive-piezoelectric bilayers." Physical Review B 68.5 (2003): 054402.

[Catalan2009] Catalan, Gustau, and James F. Scott. "Physics and applications of bismuth ferrite." Advanced Materials 21.24 (2009): 2463-2485.

[Cava2013] Cava, Robert J. "Topological insulators: Chemists join in." Nature Materials (2013).

[Chappert2007] Chappert, Claude, Albert Fert, and Frédéric Nguyen Van Dau. "The emergence of spin electronics in data storage." Nature materials 6.11 (2007): 813-823.

[Dagotto2003] E. Dagotto, "Nanoscale phase separation and colossal magnetoresistance: the physics of manganites and related compounds." Vol. 136 Springer, (2003)

[Dagotto2011] Dong, Shuai, et al. "Microscopic model for the ferroelectric field effect in oxide heterostructures." Physical Review B 84.15 (2011): 155117.

[Dong2013] Dong, Si-Ning, et al. "Room temperature multiferroicity in Bi4. 2K0. 8Fe2O9+ [dgr]." Scientific reports 3 (2013).

[Eerenstein2006] Eerenstein, W., N. D. Mathur, and James F. Scott. "Multiferroic and magnetoelectric materials." Nature 442.7104 (2006): 759-765.

[Eerenstein2007] Eerenstein, W., et al. "Giant sharp and persistent converse magnetoelectric effects in multiferroic epitaxial heterostructures." Nature materials 6.5 (2007): 348-351.

[Evans2013] Evans, D. M., et al. "Magnetic switching of ferroelectric domains at room temperature in multiferroic PZTFT." Nature Communications 4 (2013): 1534.

[Fert2008] Fert, Albert. "Nobel Lecture: Origin, development, and future of spintronics." Reviews of Modern Physics 80.4 (2008): 1517.

[Fert2013] Fert, Albert, Vincent Cros, and João Sampaio. "Skyrmions on the track." Nature Nanotechnology 8.3 (2013): 152-156.

[Fiebig2005] Fiebig, Manfred. "Revival of the magnetoelectric effect." Journal of Physics D: Applied Physics 38.8 (2005): R123.

[Gajek2007] Gajek, Martin, et al. "Tunnel junctions with multiferroic barriers." Nature materials 6.4 (2007): 296-302.

[Ghidini2013] Ghidini, M., et al. "Non-volatile electrically-driven repeatable magnetization reversal with no applied magnetic field." Nature communications 4 (2013): 1453.

[Grünberg2008] Grünberg, Peter A. "From spinwaves to Giant Magnetoresistance (GMR) and beyond." Bulletin of the American Physical Society 53 (2008).

[Hasan2010] Hasan, M. Zahid, and Charles L. Kane. "Colloquium: topological insulators." Reviews of modern physics 82.4 (2010): 3045.

[Hill2000] Hill, Nicola A. "Why are there so few magnetic ferroelectrics?." The Journal of Physical Chemistry B 104.29 (2000): 6694-6709.

[Jozwiak2013] Jozwiak, Chris, et al. "Photoelectron spin-flipping and texture manipulation in a topological insulator." Nature Physics (2013).

[Kane2005] Kane, Charles L., and Eugene J. Mele. "Z_ {2} Topological Order and the Quantum Spin Hall Effect." Physical review letters 95.14 (2005): 146802.

[Lahtinen2012] Lahtinen, Tuomas HE, Kévin JA Franke, and Sebastiaan van Dijken. "Electric-field control of magnetic domain wall motion and local magnetization reversal." Scientific reports 2 (2012).

[Lebeugle2007] Lebeugle, D., et al. "Very large spontaneous electric polarization in BiFeO single crystals at room temperature and its evolution under cycling fields." Applied physics letters 91 (2007): 022907.

[Li2009] Li, Zheng, et al. "Evidence for stress-mediated magnetoelectric coupling in multiferroic bilayer films from magnetic-field-dependent Raman scattering." Physical Review B 79.18 (2009): 180406.

[Livesey2011] Livesey, K. L. "Strain-mediated magnetoelectric coupling in magnetostrictive/piezoelectric heterostructures and resulting high-frequency effects." Physical Review B 83.22 (2011): 224420.

[Locatelli2013] Locatelli, N., et al. "Reversal process of a magnetic vortex core under the combined action of a perpendicular field and spin transfer torque." Applied Physics Letters 102.6 (2013): 062401-062401.

[Lu2011] Lu, Xiaoli, et al. "Magnetoelectric Coupling in Ordered Arrays of Multilayered Heteroepitaxial BaTiO3/CoFe2O4 Nanodots." Nano letters 11.8 (2011): 3202-3206.

[Moore2010] Moore, Joel E. "The birth of topological insulators." Nature 464.7286 (2010): 194-198.

[Moya2012] Moya, X., et al. "Giant and reversible extrinsic magnetocaloric effects in La0. 7Ca0. 3MnO3 films due to strain." Nature materials (2012).

[Parkin2008] Parkin, Stuart SP, Masamitsu Hayashi, and Luc Thomas. "Magnetic domain-wall racetrack memory." Science 320.5873 (2008): 190-194.

[Perks2012] Perks, N. J., et al. "Magneto-orbital helices as a route to coupling magnetism and ferroelectricity in multiferroic CaMn7O12." Nature Communications 3 (2012): 1277.

[Qi2010] Qi, Xiao-Liang, and Shou-Cheng Zhang. "The quantum spin Hall effect and topological insulators." Physics Today 63.1 (2010): 33-38.

[Ramesh2007] Ramesh, Ramaroorthy, and Nicola A. Spaldin. "Multiferroics: progress and prospects in thin films." Nature materials 6.1 (2007): 21-29.

[Saidaoui2013] Saidaoui, Hamed, Xavier Waintal, and Aurelien Manchon. "Spin Transfer torques in Antiferromagnets." Bulletin of the American Physical Society (2013).

[Scott2006] Scott, J. F. "TOPICAL REVIEW: Nanoferroelectrics: statics and dynamics." Journal of Physics Condensed Matter 18 (2006): 361.

[Shirane1993] Jona, Franco, and Gen Shirane. Ferroelectric crystals. New York: Dover Publications, 1993.

[Sinova2012] Sinova, Jairo, and Igor Žutić. "New moves of the spintronics tango." Nature Materials 11.5 (2012): 368-371.

[Smart2011] Smart, Ashley G. "Current-driven magnetic domain walls gather speed" Physics Today 64.7 (2011): 18.

[Sohrab2012] Chen, Hanghui, and Sohrab Ismail-Beigi. "Ferroelectric control of magnetization in La_ {1− x} Sr_ {x} MnO_ {3} manganites: A first-principles study." Physical Review B 86.2 (2012): 024433.

[Spaldin2005] Nicola A. Spaldin and Manfred Fiebig, Science 309, 391 (2005)

[Spaldin2010] Spaldin, Nicola A., Sang-Wook Cheong, and Ramamoorthy Ramesh. "Multiferroics: Past, present, and future." Phys. Today 63 (2010): 38-43.

[Steil2013] Steil, Sabine, et al. "Spin-dependent trapping of electrons at spinterfaces." Nature Physics (2013).

[Stiles2002] Stiles, M. D., and A. Zangwill. "Anatomy of spin-transfer torque." Physical Review B 66.1 (2002): 014407.

[Streubel2013] Streubel, Robert, et al. "Strain-mediated elastic coupling in magnetoelectric nickel/barium-titanate heterostructures." Physical Review B 87.5 (2013): 054410.

[Tay2013] Tay, Tiamhock, and L. J. Sham. "Theory of atomistic simulation of spin-transfer torque in nanomagnets." arXiv preprint arXiv:1303.1775 (2013).

[Thiele2007] Thiele, C., et al. "Influence of strain on the magnetization and magnetoelectric effect in La0.7A0.3MnO3/ PMN-PT (001) (A= Sr, Ca)." Physical Review B 75.5 (2007): 054408.

[Tokunaga2012] Tokunaga, Yusuke, et al. "Electric-field-induced generation and reversal of ferromagnetic moment in ferrites." Nature Physics (2012).

[Trinh2013] Trinh, H-P., et al. "Magnetic Adder Based on Racetrack Memory." (2013): 1-9.

[Tsymbal2009] Burton, John D., and Evgeny Y. Tsymbal. "Prediction of electrically induced magnetic reconstruction at the manganite/ferroelectric interface." Physical Review B 80.17 (2009): 174406.

[Vaz2010] Vaz, Carlos AF, et al. "Magnetoelectric coupling effects in multiferroic complex oxide composite structures." Advanced Materials 22.26-27 (2010): 2900-2918.

[Vaz2012] Vaz, Carlos AF. "Electric field control of magnetism in multiferroic heterostructures." Journal of Physics: Condensed Matter 24.33 (2012): 333201.

[Velev2008] Velev, Julian P., et al. "Magnetic tunnel junctions with ferroelectric barriers: Prediction of four resistance states from first principles." Nano Letters 9.1 (2008): 427-432.

[Wang2003] Wang, J. B. N. J., et al. "Epitaxial BiFeO3 multiferroic thin film heterostructures." Science 299.5613 (2003): 1719-1722.

[Wang2009] Wang, K. F., J-M. Liu, and Z. F. Ren. "Multiferroicity: the coupling between magnetic and polarization orders." Advances in Physics 58.4 (2009): 321-448.

[Wang2011] Wang, T-H., et al. "Magnetoelectric coupling and phase transition in BiFeO3 and (BiFeO3) 0.95(BaTiO3)0.05 ceramics." Journal of Applied Physics 109.4 (2011): 044101-044101.

[Wang2013] Wang, J. W., et al. "Ferroelectric-domain-controlled magnetic anisotropy in Co 40 Fe 40 B 20/YMnO 3 multiferroic heterostructure." Applied Physics Letters 102.10 (2013): 102906-102906.

[Winpenny2013] Winpenny, Richard EP. "Molecular spintronics: Stretch for a moment." Nature Nanotechnology 8.3 (2013): 159-160.

[Wu2013] Wu, S. M., et al. "Full Electric Control of Exchange Bias." Physical review letters 110.6 (2013): 067202.

[Xue2013] Xue, Qi-Kun. "Topological insulators: Full spin ahead for photoelectrons." Nature Physics (2013).

[Zhao2006] Zhao, T., et al. "Electrical control of antiferromagnetic domains in multiferroic BiFeO3 films at room temperature." Nature materials 5.10 (2006): 823-829.

[Zhou2012] Zhou, Yi, and Fu-Chun Zhang. "Quantum spin Hall effect: Left up right down." Nature Physics 8.6 (2012): 448-449.

CHAPTER 2

MATERIALS OVERVIEW

In this chapter, a brief introduction to manganites (specifically $La_{0.7}Ca_{0.3}MnO_3$) and $BaTiO_3$ is given. The first part is focused on the key concepts of phase separation and cooperative effects (from the Zener double exchange model to the Jahn-Teller effects) that lead to coexistence of metallic and ferromagnetic phases in the ferromagnetic $La_{0.7}Ca_{0.3}MnO_3$. In the second part, the bulk properties of the ferroelectric $BaTiO_3$ substrates are considered (bulk structure, ferroelectricity and piezoelectricity at all temperatures) emphasizing the origin of corrugation and surface morphology. The purpose of this chapter is to review the basic phenomenology of these materials that lead to the complex behavior presented later in this thesis.

MANGANITE OXIDES. $La_{1-X}Ca_XMnO_3$

The family of materials with chemical composition $A_{1-x}R_xMnO_3$ is named manganites, where A ≡ La, Pr, Nd… and R ≡ Sr, Ca, Ba… They were first described in 1950 by Jonner and van Santen [vanSanten1950, Kresin2004]. In manganites the ferromagnetic phase is only found at a finite doping, $x \neq 0$ and the Curie temperature in which this transition occurs coincide with a transition from an insulating to a metallic phase. In $La_{1-x}Ca_xMnO_3$ manganites, for example, the FM phase is found in the interval $0.2<x<0.5$. This is a fundamental property of manganites and was explained for the first time by Zener in 1951 [Zener1951]. In his paper, the connection between the metallic and the ferromagnetic phase was explained in terms of the Double Exchange mechanism. The second fundamental property of manganites is the colossal magnetoresistance effect, discovered by Jin *et al*. in 1994 [Jin1994].

Manganite compounds are members of a broader set of compounds known as strongly correlated systems. One of the basic properties of these systems is the generation of energy gaps different than the band gaps that lead to insulating behavior in other materials. For example, cooperative effects may take place conditioning the appearance of phase transitions.

As we will see two key concepts become relevant in manganites: 1) competition between phases and 2) inhomogeneously distributed carriers resulting from phase competition. In this theoretical framework, the fundamental properties of manganites have been studied [Dagotto2003] in order to understand the rich phase diagrams (exhibiting unusual spin, charge, lattice and orbital orders) and colossal magnetoresistance.

PARENT COMPOUNDS

The zero doping parent compound of manganites is $LaMnO_3$ [Dagotto2003, Salomon2001], with perovskite structure (see Fig. 1) in which the Mn ion is in the center of an oxygen octahedron. The electronic configuration of the Mn ion is $[Ar]3d^54s^2$. Due to the crystal field splitting, the five d electron levels are separated in 2 degenerated sets: 2 orbitals of higher level, denoted as e_g (d_z^2, $d_{x^2-y^2}$) and three orbitals denoted as t_{2g} (d_{xy}, d_{yz}, d_{zx}). Mn^{3+} has 4 electrons in d-orbitals. Three of them occupy the t_{2g} orbitals according to Hund's coupling with spin S = 3/2. The remaining e_g electron is free to hop in the crystal. Manganites are classified as large, intermediate and low bandwidth, according to the magnitude of the hopping amplitude of the e_g electron. As the hopping amplitude increases more metallic (and ferromagnetic) the manganite will be.

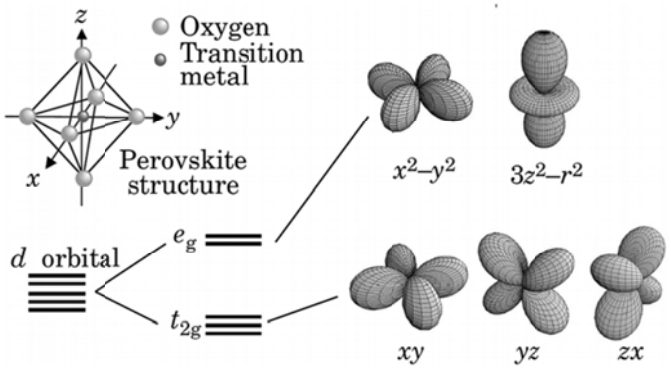

Fig.1. Perovskite structure, crystal splitting and the corresponding orbitals for the d-shell. Adapted from [Dagotto2003]

The ground state of $LaMnO_3$ is insulating antiferromagnetic (A type) with orthorhombic unit cell, (space group Pnma) [Salomon2001]. The magnetic moments lie in the a-c plane and are ferromagnetically aligned along the a-axis and antiparallel aligned in successive planes along the b-axis. Upon doping a rich phase diagram arises with different magnetic, charge and orbital orders. Replacing a fraction x of La^+ ions by a divalent ion is equivalent to doping with x holes. In the particular case of doping with Ca+ cations, the end-member of the series is $CaMnO_3$, when x = 1, which is cubic (space group Pm3m), also antiferromagnetic and G-type (the inter-plane and the intra-plane couplings are antiferromagnetic) [Maezono1998]. The magnetic phases of $LaMnO_3$ and $CaMnO_3$ and intermediate doped compounds (see Fig. 2), were first studied by Goodenough [Goodenough1955] in terms of covalent and semicovalent bonds between Mn-O-Mn bond angles and the corresponding lattice distortions.

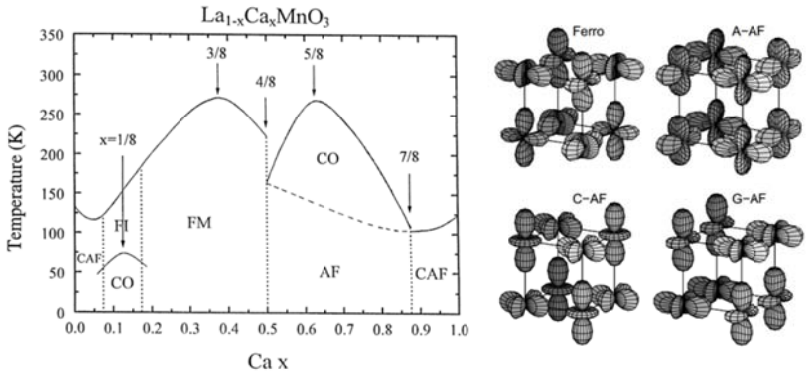

Fig.2. $La_{1-x}Ca_xMnO_3$ Phase Diagram (left) and antiferromagnetic orderings. Adapted from [Dagotto2003] and [Maezono1998]

$La_{1-X}Ca_XMnO_3$

$La_{1-x}Ca_xMnO_3$ compounds are one of the most extensively studied intermediate bandwidth manganites [Dagotto2003]. From now on, we will only consider Ca^{2+} substitutions. In the optimal doping region, the most relevant properties of these manganites are: 1) The insulating state over the T_c, in the paramagnetic regime, which is not well explained by the double-exchange mechanism. 2) A sharp transition from the insulating phase to the metallic phase observed around the Curie temperature, making the metal insulator transition coincidental with the paramagnetic-ferromagnetic transition. 3) At very low temperatures, the resistivity is still several orders of magnitude higher than most common. For reference and easy comparison in the following chapter, the basic phenomenology from Ref. [Schiffer1995] is shown, in Figure 3.

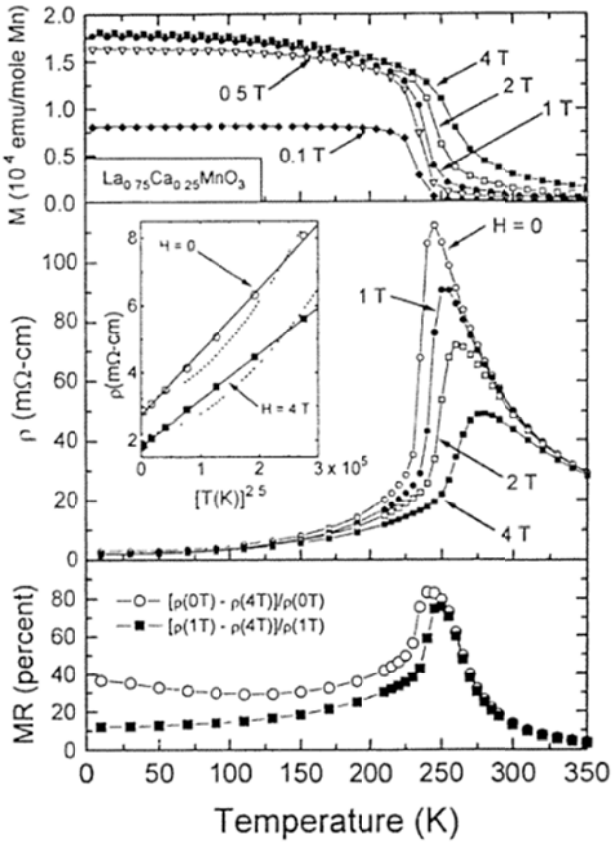

Fig. 3. Magnetization, resistivity and magnetoresistance of $La_{0.75}Ca_{0.25}MnO_3$, as a function of temperature, at various magnetic fields. Adapted from Ref. [Schiffer1995].

COLOSSAL MAGNETORESISTANCE

Colossal magnetoresistance is one of the fundamental properties of manganites. It was first described in Volger's paper [Volger1954], but, as already mentioned, the real magnitude of the effect was recognized by Jin *et al*. [Jin1994]. The magnetoresistance ratio is often expressed as:

$$\frac{\Delta R}{R} = \frac{(R_H - R_0)}{R_H} \qquad [1]$$

where R_0 is the resistance when no external magnetic field is applied and R_H is the resistance under a certain applied magnetic field. In Ref. [Jin1994], a thousand fold change in resistivity was reported. An example of magnetoresistance observed in manganites can be seen in Fig. 3, middle panel. Early theoretical works based solely on double exchange and one orbital model do not explain the colossal magnetoresistance effect. In fact, only theories based on the strong competition between nearly degenerate ground states, proposed in the last two decades, have successfully explained the observations [Dagotto2003].

DOUBLE EXCHANGE MECHANISM

As mentioned above, one of the early attempts to explain the correlation between ferromagnetic and metallic phases was the Double Exchange mechanism proposed by Zener. In doped manganese oxides the two possible configurations are degenerate:

$$\psi_1 : Mn^{3+}O^{2-}Mn^{4+} \quad and \quad \psi_2 : Mn^{4+}O^{2-}Mn^{3+} \qquad [2]$$

and connected by the "double Exchange" matrix. The elements of this matrix arise from the process in which an e_g electron moves from one Mn ion to another through the O ion in between. Figure 4 shows this process as thought of by Zener: one e_g electron moves from the oxygen to the Mn in one side and another one from the Mn in the other side to the oxygen ("double exchange"), giving a net transport of one electron. Several factors favor this exchange: first, the electrons preserve their spin during the transfer; second, the conducting electron lowers its kinetic energy (regulated by the hopping amplitude, t, if the t_{2g} electron band (d-shell) is fully polarized, because the t_{2g} electrons are indirectly coupled (Hund coupling, J_H) with the e_g electrons; third, the direct coupling between d-shells is antiferromagnetic (J_{AF}). The coupling lifts the degeneracy and the system resonates between ψ_1 and ψ_2 if the core spins are parallel. This process leads to the ferromagnetic-conducting ground state [Salomon2001, Dagotto2003].

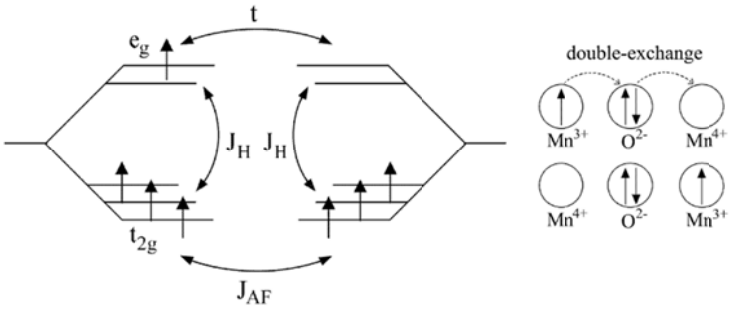

Fig.4. Main interactions and couplings considered in the Zener model (left) and a scheme of the process of double exchange. Figure adapted from Ref. [Dagotto2003].

JAHN-TELLER EFFECT

Until this moment, we have considered only crystal field splitting of the five degenerate d orbitals of the isolated ion Mn^{3+}. That is, once in a crystal with cubic symmetry, Mn^{3+} orbitals split into two sets of degenerate orbitals, t_{2g} and e_g. Estimations of this splitting energy can be found if Ref. [Dagotto2003].There, the well-known expression for the energy gap is derived: $\Delta = 10Dq$, where D is given by $Z\langle r^4\rangle / 6a^5$, Zq is the charge of the oxygen ions located at a distance "a" of the Mn-ion and responsible of the perturbing potential. Typical results for the gap Δ are between 1 and 2 eV. If the symmetry is lower than cubic, other splittings can appear. For example, in the case of a tetragonal distorted lattice, the t_{2g} triplet can split as the d_{xy} and d_{xz} and d_{yz} are not equivalent. The same happens with the e_g doublet: $d_{x^2-y^2}$ has most of its relevant weight in the x-y plane while the $d_{3z^2-r^2}$ is elongated along the c axis (when considering a distortion such as $a = b \neq c$).

However, the degeneracy left in cubic symmetry is usually broken by lattice displacements. The ligand ions surrounding the Mn ion can move slightly to adjust their position, breaking the symmetry, lowering the energy of the system and effectively removing the degeneracy. This is the Jahn-Teller cooperative effect. Although this distortion is small, this effect becomes crucial in the understanding of the physics of manganites. Again, in Ref. [Dagotto2003], a detailed analysis of the possible modes of distortion and their effect in breaking the degeneracy of the different orbitals is given. The most interesting distortions to consider are those in which the octahedra either elongate or contract in one of the three spatial directions (denoted by Kanamori [Kanamori1960] by Q_2 and Q_3). The Jahn-Teller effect in a crystal becomes a cooperative effect since each oxygen atom in the lattice is shared with its neighbor.

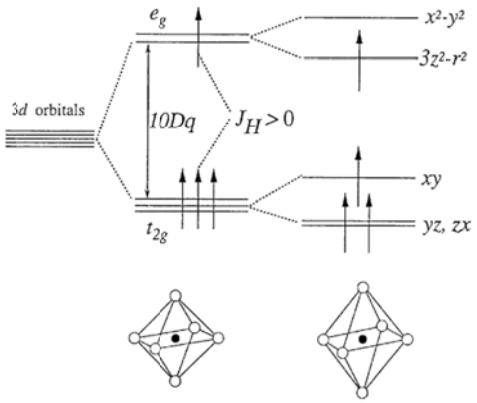

Fig.5. Crystal Field Splitting and tetragonal distortion. Figure adapted from Ref. [Dagotto2003].

PERCOLATIVE PHENOMENA

The random character of the ion-substitution in the process of doping leads to a statistical distribution of clusters that can be treated in the context of percolation theory. Starting at the x = 0 parent compound $LaMnO_3$, substitutions of the La^{3+} by Ca^{2+} creates a hole in the manganite unit cell that remains localized due to Coulomb repulsion. Then, as the doping is increased, the number of holes increases until the formation of clusters. Now these holes are delocalized within the cluster and according to the Zener double exchange the Mn spins align ferromagnetically.

As the doping level increases further, the number of clusters increases and they start to overlap. When a critical value is reached (percolation threshold, at $x = x_c$) the system appears as a macroscopic metallic ferromagnetic phase of connected islands. This percolative insulator-metal transition is described in works by Kresin [Kresin2004] and more recently in [Salomon2001, Dagotto2003]. A relevant aspect of this percolative behavior is the intrinsic inhomogeneity that leads to "phase separation", or the simultaneous existence of mutually interpenetrating sub-phases. Percolation can be understood as a case of phase separation of coexisting phases in a mesoscopic scale where macroscopic properties are determined by one of the sub-phases.

PERCOLATIVE PHASE SEPARATION AND COLOSSAL MAGNETORESISTANCE

After the previous considerations, we are now in a position to describe qualitatively the process taking place near T_c that results in colossal magnetoresistance in optimally doped optimal doping manganites.

Mayr *et al.* [Mayr2001] addresses the problem of explaining the resistivity in manganites by using a random resistor-network and phase separation theory. The manganite state in the colossal magnetoresistance regime was assumed to be percolative, with metallic filaments across the sample. They considered an array of resistors arranged in a cubic system with resistances with either metallic (percolative) or insulating characteristics. At low temperatures, the resistance of the insulating regions ($R^I(T)$) is higher than the percolative resististance ($R^{per}(T)$), thus transport is mostly due to the conductance paths. As temperature increases, the percolative paths are easily suppressed by temperature effects that may cut off the line of transport across the sample, resulting in an increase of $R^{per}(T)$. At room temperature, $R^I(T) < R^{per}(T)$ and conduction occurs through the insulator. The combination of these two effective resistances leads to the metal-insulator transition occurring at T_c.
In the percolative regime small perturbations can drastically change the conductivity. In the random-network proposed by [Mayr2001], an applied magnetic field will increase the fraction of ferromagnetic clusters in a certain amount, thus, near the percolation, these small changes can induce a large change in the resistance. Then, colossal magnetoresistance is explained by means of enhanced ferromagnetic regime when applying magnetic fields.

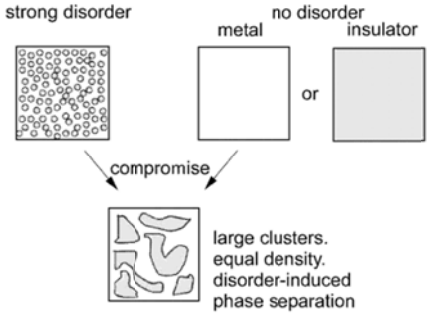

Fig.6. Scheme of phase separation, the number of clusters of the different coexisting phases is a compromise to reduce the energy at the domain walls. Adapted from Ref. [Dagotto2003].

In summary, the main properties of mixed doped manganites have been summarized. We considered the relevant aspects of cooperative effects and phase separation and their implications in the physics of manganites. We described the models of "double exchange" mechanism, able to explain the formation of ferromagnetic and antiferromagnetic phases, and phase separation. Competition between coexisting phases in mixed doped manganites is the key concept at the origin of a great majority of manganite properties such as colossal magnetoresistance.

BARIUM TITANATE, $BaTiO_3$

This section is devoted to $BaTiO_3$ used as substrate in the heterostructures studied in this thesis. As one of the most studied ferroelectric materials of the perovskite class, two factors are of crucial importance: ferroelectricity and structural properties.

STRUCTURAL PROPERTIES

The Curie temperature of $BaTiO_3$ is at 393 K [Shirane1996]. The symmetry of the non-polar phase is **cubic** (point group m3m), thus centrosymmetrical and non-piezoelectric. This phase has a perovkite-type structure. The coordinates of the atoms in this structure are given by the following spatial positions: Ba at (0,0,0), Ti at (1/2,1/2,1/2) and 3 O at (1/2,1/2,0), (1/2,0 ,1/2) and (0,1/2,1/2) and the cell edge is about 4 Å. Another equivalent visualization is as a face-centered-cubic close-packed arrangement with the Ti in the center surrounded by an octahedral of oxygen and the Ba-ions in the vertices of the cube (as schematized in Fig. 1 for manganites).

Below 393K, $BaTiO_3$ undergoes three ferroelectric phases with spontaneous polarization along the three axes possibilities discussed by Devonshire in ref. [Devonshire1949]: tetragonal, orthorhombic and rhombohedral phases The spontaneous polarization, which is electrostictive in nature, lowers the cubic symmetry to **tetragonal** (C_{4v}, point group 4mm, c > a) by an elongation in the direction of the polar axis (along the edge of the cube, identified as the "c" axis) and a contraction in the directions perpendicular to it. The actual unit cell can be in one of the six equivalent spatial crystallographic configurations of strain and polarization (Fig. 9). Domains separated by 90° and 180° walls appear. External electric fields can move the actual domains or nucleate them through the ferroelastic effect of domain switching [Burcsu2001]. Therefore, $BaTiO_3$ transition to the ferroelectric phase is displacive in nature and it is due to the non-cubic surroundings of the oxygen ions [Kittel1996]. In the tetragonal phase, a displacement between the positive Ba^{2+}, Ti^{4+} ions with respect to the negative O^{2-} implies a cell dipole moment of $p \approx 2 \cdot 10^{-29}$ Cm. The tetragonality of this phase is of the order $c/a \approx 1.011$, with a spontaneous strain of 1.1%. The spatial positions of the atoms are: Ba at (0,0,0), Ti at $(1/2,1/2,1/2+\delta z_{Ti})$, one oxygen at $(1/2,1/2, \delta z_{OI})$ and the second $(1/2,0 ,1/2+ \delta z_{OII})$ and $(0,1/2, 1/2+ \delta z_{OII})$, where the displacement between ions is parameterized as δz_{Ti}, δz_{OI}, δz_{OII} (see Table I). The lattice parameters of this phase are a = 3.992 Å and c = 4.036 Å. The lattice parameters of $BaTiO_3$ in the four phases, as obtained by Kay and Vouden in Ref. [Kay1949], appear in figure 10.

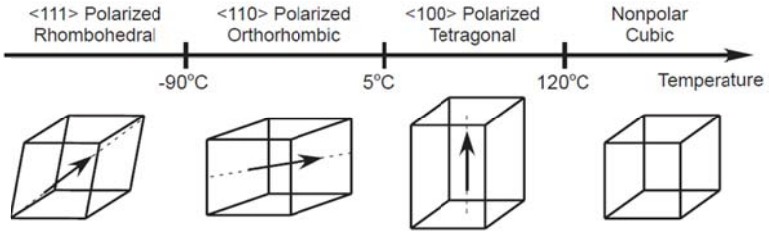

Fig.9. Phases of barium titanate. The arrow indicates the direction of spontaneous polarization. Adapted from Ref. [Burcsu2001]

At lower temperatures (183 K < T < 278 K) the symmetry lowers to **orthorhombic** (C_{2v}) with polarization axis is along a face diagonal [110], (point group 2mm). Referring to the cubic unit cell, the orthorhombic distortion appears as an elongation of one of the face diagonals and a compression of the other. The twelve equivalent [110] directions are then the twelve possible directions of the spontaneous polarization in this phase (Fig. 9). Orthorhombic lattice parameters at 273 K are: a_0 = 5.682 Å, b_0 = 5.669 Å and c_0 = 3.990 Å. The displacement of the ions in this phase is summarized in Table I. The orthorhombic unit cell can be described as a monoclinic unit cell, conserving the edges of the unit cell almost parallel to the original cubic edges, the relation between the monoclinic lattice parameters (a_m ,b_m ,c_m and γ) and the orthorhombic ones is given by:

$$\begin{aligned} a_0 &= 2a_m \sin(\gamma/2) \\ b_0 &= 2b_m \cos(\gamma/2) \\ c_0 &= c_m \end{aligned} \qquad [3]$$

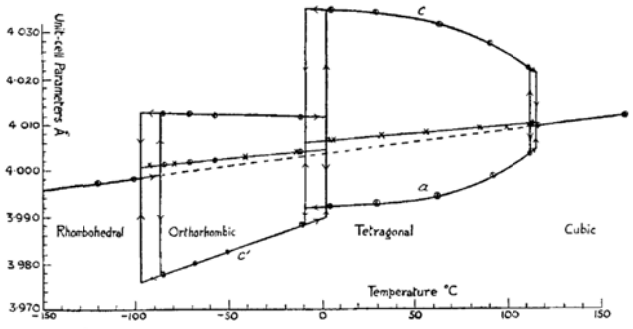

Fig.10. Lattice constants of BaTiO3 as functions of temperature. Adapted from Ref. [Kay1949].

Finally, at lower temperatures (T < 183 K) polarization along the body diagonals reduces the symmetry to **rhombohedral** (C_{3v}). In this phase (space group R3m) the polar axis lies along one of the original cubic diagonal [111]. The rhombohedral distortion consists of a stretch along one of the body diagonals and the eight equivalent [111] directions become the possible directions of the spontaneous polarization (Fig. 9). Again, lattice parameters and structural displacements are listed in Table I.

TABLE I. $BaTiO_3$ lattice parameters and atomic extracted from Refs. [Billinge1993]. Peudomonoclinic parameter in the orthorhombic phase is c_m = 4.017 Å and γ = 89.824º.

	RHOMBOHEDRAL	ORTHOROMBIC	TETRAGONAL	CUBIC
Parameters (Å)	a = 4.004 α = 89.837°	a_0 = 3.984 b_0 = 5.674 c_0 = 5.692	a = 3.992 c = 4.036	a = 4
Atomic Shifts (Å)	δx_{Ti} = -0.011 δx_{OI} = +0.011 δz_{OI} = -0.018	δz_{Ti} = +0.008; δy_{OII} = +0.004 δz_{OI} = -0.015; δz_{OII} = -0.019	δz_{Ti} = +0.022 δz_{OI} = -0.024 δz_{OII} = -0.011	-

FERROELECTRIC AND DIELECTRIC PROPERTIES

The **dielectric properties** of $BaTiO_3$ single crystals were studied first by Merz in 1949 [Merz1949]. Figure 11 shows the initial dielectric constants in the a- and c-directions as a function of temperature in the three ferroelectric phases and at the phase transitions. In the cubic phase only one dielectric constant is expected. This dielectric constant follows the Curie-Weiss law $\varepsilon = C/(T-T_0)$. At lower temperatures, spontaneous polarization causes the single crystal to split into multiple ferroelectric domains with different dielectric constants. [Wang2011].

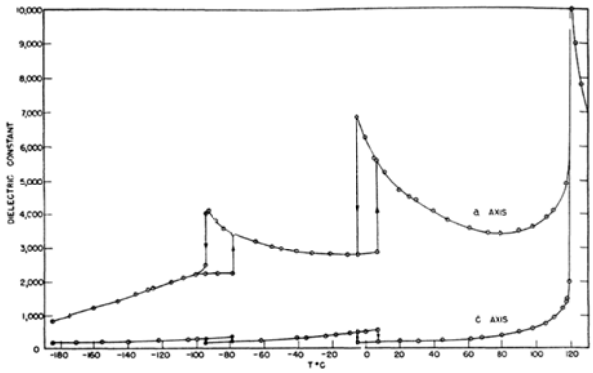

Fig.11. Dielectric constant of $BaTiO_3$ as function of temperature. Adapted from [Merz]

Results of $BaTiO_3$ **spontaneous polarization** obtained by measuring hysteresis loops can be found in Ref. [Merz1949] and in Fig. 12. The value of the spontaneous polarization at room temperature is typically $16 \cdot 10^{-6}$ C cm^{-2}. The lower values obtained at the lower temperature phases are partially due to the inferior quality of the crystals.

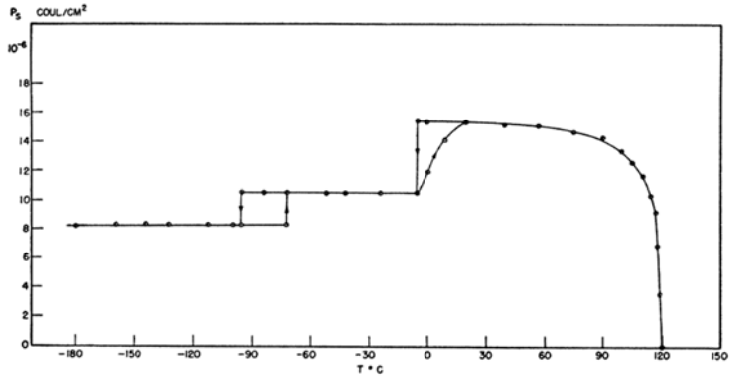

Fig.12. Spontaneous polarization as function of temperature. The magnitude of the spontaneous polarization, P_s, must be multiplied by $\sqrt{2}$ in the orthorhombic phase and by $\sqrt{3}$ in the rhombohedral phase, since P_s is aligned along the [110] and [111] directions, respectively. Adapted from [Merz1949]

Hysteresis loops of single crystal $BaTiO_3$ exhibit sharp corners and a marked rectangular appearance. Early values of the **coercive fields** were obtained by H.H. Wieder [Wieder1957] and can be seen in Figure 13. The experimental values of the coercive fields were found to be smaller (0.05 kV/mm – 0.2 kV/mm) than expected from Landau-Devonshire theory, ~1 kV/mm [Shirane1996]. Merz found experimentally that the field at which the polarization reverses depends on the time in which the polarization vector changes its orientation.

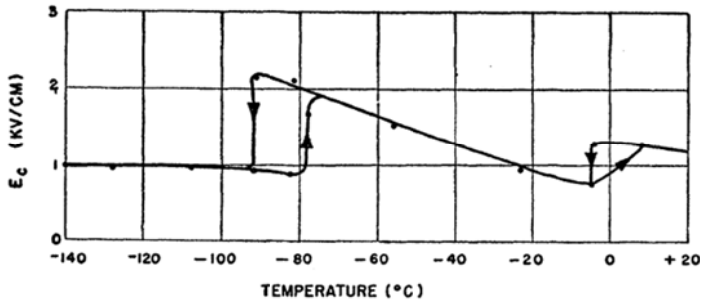

Fig.13. Coercive field of BaTiO3 as a function of temperature. The values shown here were extracted from hysteresis loops measured at 60 cycles/s. Figure adapted from [Wieder1957]

The complicated **domain patterns** present in $BaTiO_3$ bulk were initially observed using polarizing microscope in Refs. [Kay1949, Forsberg1949, Merz1949, Shirane1996]. In the tetragonal phase it is possible for adjacent domains to be polarized at 90º to each other (Fig. 14). When the polar axis is perpendicular to the observation plane the domain is called "c"-domain. When it lies within plane it is called "a"-domain. In a square shaped sample the distribution of domains can be observed parallel to one of the edges of the sample or at 45º. In the first case, consecutive "a" and "c" domains appear separated by a 90º wall; in the second case, only "a"-domains are observed in the sample plane. The first condition for these walls to be stable is that no charge may be accumulated on the wall. This requires a "head-to-tail" arrangement of the polar axes of adjacent domains.

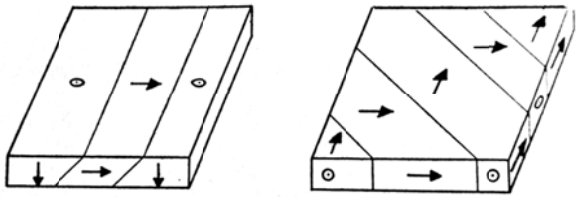

Fig.14. Domains patterns in the tetragonal phase. Accommodation of domains in the configuration of the left give rise to the tetragonal corrugation of 0.6°; a-domains as in right figure show an almost flat surface. [Shirane1996]

The second condition is the continuity and the matching of the lattice at the wall. The accommodation of domains in the tetragonal phase can be seen in Figure 15 [Shirane1996]. As the tetragonality of the $BaTiO_3$ is ~1% the angle between two adjacent 90º domains is not exactly 90º. The **corrugation** angle is given by 2 arctan(c/a) ≈ 0.6º. When adjacent domains are oriented antiparallel the domain wall is called (logically) 180º wall. 180º walls are very thin since the spontaneous polarization can reverse within one unit-cell and the periodicity of the lattice is practically undisturbed.

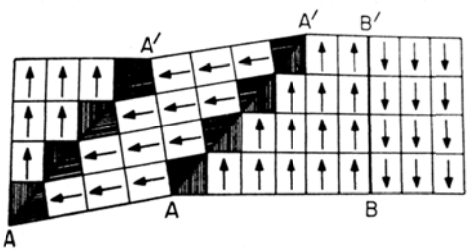

Fig.15. Corrugation in the tetragonal phase. Figure adapted from Ref. [Shirane]

Kay and Vousden [Kay1949] and Forsbergh [Forsbergh1949] also studied the domain structure in the orthorhombic and rhombohedral phases. In the orthorhombic phase, 90º walls are parallel to pseudo-cubic [001] planes and 60º walls are parallel to the [011] pseudo-cubic planes. In the rhombohedral phase domain walls of 180º, 71º and 109º are expected (see Fig. 16). However, recent studies by Marton *et al.* [Marton2010] predict that only 71º and 109º domain walls are as thin and stable as the 180º domain walls in the tetragonal

phase. The expected corrugation of the 109º walls by reflection twinning in [001] **R** planes is 2*(90-α)=0.3º, with α being the rhombohedral angle.

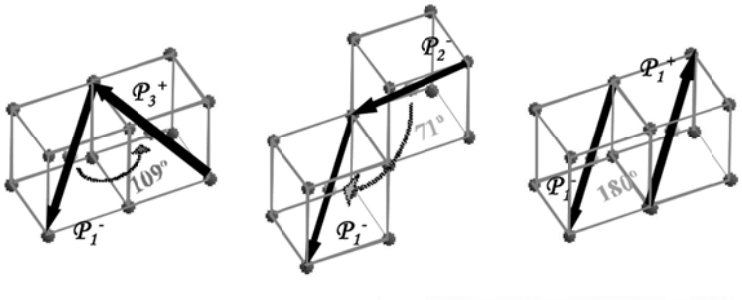

Fig.16. Domains at lower temperature. Figure adapted from Ref. [Catalan2012]

PIEZOELECTRICITY IN $BaTiO_3$

Piezoelectricity is the property of some crystals to exhibit electric polarity under applied stress. Piezoelectricity appears in all twenty-one crystal classes that do not have a center of symmetry with the exception of the cubic class 232 (due to its other symmetry elements) [Devonshire1954]. The piezoelectric effect is understood as the linear electromechanical interaction between the mechanical and the electrical state in crystalline materials:

$$D_i = D_{ijk}\sigma_{jk} \qquad [4]$$

Where D_i is the electric displacement vector (first-rank tensor), σ_{jk} is the stress tensor (second-rank) and D_{ijk} the piezoelectric coefficient (a third-rank tensor). Using the reduced matrix Voigt notation [Nye1985], D_{ijk} is expressed as D_{km}, where k denotes the component of electric displacement **D** in the Cartesian reference frame (x_1, x_2, x_3) and the index $m = 1, \ldots, 6$ is used to define the mechanical stress or strain. D_i is related to the polarization, **P**, by $D_i = P_i + \varepsilon_0 E_i$ where ε_0 is the permittivity of free space and E is the electric field vector [Nye1985].

In materials exhibiting the opposite effect, called converse piezoelectric effect, the application of an electrical field creates a mechanical deformation in the crystal:

$$\varepsilon_{ij} = d_{ijk}E_k \qquad [5]$$

where ε is the strain tensor. Note that the coefficient "d" for the direct and the converse piezoelectric effects is thermodynamically equivalent and the piezoelectric effect is reversible [Nye1985]. The number of independent elements of d_{ijk} is determined by the symmetry of the crystal studied. What is commonly found in literature is the longitudinal d_{33} piezoelectric coefficient that accounts for the deformation expected along the x_3 axis of the crystal system, ε_{33}, due to an electric field component along the same axis, P_3.

We now concentrate on the piezoelectric properties of $BaTiO_3$ single crystals. As we discussed above, ferroelectric phases of $BaTiO_3$ can be considered as small distortions of the cubic paraelectric perovskite structure and, therefore, studied in terms of the orthogonal components of polarization, P_j. Then, by using the Landau-Ginzburg-Devonshire approach and the free energy F=U-**P**·**E,** the temperature dependence of the piezoelectric coefficients can be predicted [Damjanovic2006, Damjanovic2002], while, experimentally, d_{km} can be calculated from the slope of strain vs E-field curves. Typical values reported in literature for $BaTiO_3$ longitudinal d_{33} coefficient are 100 pC/N in the tetragonal phase and 350 pC/N in the rhombohedral phase [Park1999].

There are two types of contributions to the piezoelectric effect: the intrinsic and extrinsic contributions. The former refers to the piezoelectric effect of the lattice and the latter is due mainly to motion of non-180º domain walls. For example, in tetragonal $BaTiO_3$, this domain wall contribution comes from the rotation of "a"-

domains to "c"-domains when applying an electric field along the x_3 axis. In this case, a strain of 1% can be reached [Fu2000]. Furthermore, the domain wall contribution to d_{33} is significantly larger in coarse-grained $BaTiO_3$ crystals, while this is small in fine-grained crystals [Damjanovic1997].

The enhancement of d_{33} when applying the electric field along a direction different than the polar axis observed by Park [Park1999] in $BaTiO_3$ is not explained in terms of these two contributions. In fact, in $BaTiO_3$ rhombohedral phase the irreversible displacement of domain walls is expected to be low (~30 pC/N) [Damjanovic1997] compared with the experimental value observed. This enhancement has been observed in several ferroelectric crystals as $KNbO_3$ [Budimir2005] and solid solutions as PZT-PT and PMN-PT [Park1999, Fu2000, Bell2001].

There are several possible mechanisms at the origin of enhanced piezoelectric response along axes different than the polar axis [Damjanovic2002]. Some of them are: field induced polarization rotation and engineered domain configuration.

- *Field Induced Polarization Rotation*

A detailed analysis of the field induced polarization rotation mechanism is given in Ref. [Fu2000b]. Three main ideas are extracted from that work: First, rotating the polarization from spontaneous direction in the rhombohedral phase to the [001] (spontaneous direction in the tetragonal phase) enhances the piezoelectric effect; second, this enhanced piezoelectric effect is path dependent, that is, depends on the history followed by the polarization when aligning with the applied electric field and, third, this effect is possible because applied electric fields flatten the internal energy surface profile [Budimir2005].

- *Engineered domain configuration*

When a sufficiently large field is applied along one of the possible polar axes (of the ground state or zero-field state), domain polarization aligns minimizing the angle with respect the electric field. Then, an engineered domain configuration is reached. When applying electric fields parallel to the poling direction, all domains are equivalent and the crystal behaves as a single domain. When this happens, possible changes in polarization and strain may be considered as changes to the crystal symmetry [Bell2001]

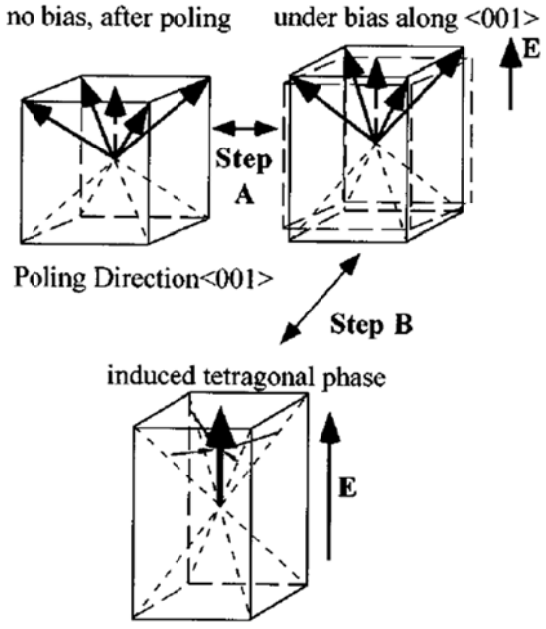

Fig.17. Schematic diagram of domain configurations in [001] oriented rhombohedral crystals under bias. Adapted from Ref. [Park1997]

Consequently, the mechanism of piezoelectricity in the rhombohedral phase of $BaTiO_3$ in engineered domain configuration can be understood as a two-steps process (see Fig. 17). In the first step (step A), piezoelectricity is due to either intrinsic contribution or to 71º domain switching (extrinsic contribution). In this step, the change in strains reached is relatively low. Then, before electric breakdown of the substrate, with high enough electric fields [Bell] a phase transition to a tetragonal phase can be induced [Park1997, Fu2000, Fu2000b, Bellaiche2001, Damjanovic 2006] and the polarization vector rotated to be parallel to the applied electric field. In this case, longitudinal piezoelectric strains as high as 2% are expected [Fu2000b]

In summary, in this section we described bulk $BaTiO_3$ properties. The basic structural characterization and the ferroelectric properties of this compound at room temperature are well known for decades. However, the complexity derived from the multi-domain formation (and quality loss) complicate the proper characterization at low temperature. One example of this is the disparity found in the literature of the piezoelectric coefficient of $BaTiO_3$, affected by the predominant mechanism of switching.
The scenario appearing in the rhombohedral phase has been described. In this phase, the polarization vector is directed along the longest diagonal of the pseudocubic unit cell. The resulting corrugation angle is 0.3º and the formation of 71º and 109º domain walls is expected. The ferroelectric switching in the rhombohedral phase is affected by several factors (domain, wall and polarization rotations) that depend on the domain configuration and sample history. Finally, the piezoelectric response appearing when applying the electric field along axes different than the ground state polar axis has been studied. This will be of great interest for future discussion in Chapter 8 of this thesis.

REFERENCES

[Bell2001] Bell, A. J. "Phenomenologically derived electric field-temperature phase diagrams and piezoelectric coefficients for single crystal barium titanate under fields along different axes." Journal of Applied Physics 89.7 (2001): 3907-3914.

[Bellaiche2001] Bellaiche, L., Alberto García, and David Vanderbilt. "Electric-field induced polarization paths in Pb (Zr_ {1-x} Ti_ {x}) O_ {3} alloys." Physical Review B 64.6 (2001): 060103.

[Billinge1993] Kwei, G. H., et al. "Structures of the ferroelectric phases of barium titanate." The Journal of Physical Chemistry, 97.10, 2368-2377, (1993)

[Budimir2005] Budimir, Marko, Dragan Damjanovic, and Nava Setter. "Enhancement of the piezoelectric response of tetragonal perovskite single crystals by uniaxial stress applied along the polar axis: A free-energy approach." Physical Review B 72.6 (2005): 064107.

[Budimir2005] Budimir, Marko, Dragan Damjanovic, and Nava Setter. "Enhancement of the piezoelectric response of tetragonal perovskite single crystals by uniaxial stress applied along the polar axis: A free-energy approach." Physical Review B 72.6 (2005): 064107.

[Burcsu2001] Burcsu, Eric Noboru. "Investigation of large strain actuation in barium titanate". Diss. California Institute of Technology, 2001.

[Catalan2012] Catalan, Gustau, et al. "Domain wall nanoelectronics." Reviews of Modern Physics 84.1 (2012): 119.

[Dagotto2003] E. Dagotto, "Nanoscale phase separation and colossal magnetoresistance: the physics of manganites and related compounds." Vol. 136. Springer, (2003)

[Damjanovic1997] Damjanovic, Dragan, and Marlyse Demartin. "Contribution of the irreversible displacement of domain walls to the piezoelectric effect in barium titanate and lead zirconate titanate ceramics." Journal of Physics: Condensed Matter 9.23 (1997): 4943.

[Damjanovic2002] Damjanovic, Dragan, Franziska Brem, and Nava Setter. "Crystal orientation dependence of the piezoelectric d coefficient in tetragonal BaTiO as a function of temperature." Applied physics letters 80 (2002): 652.

[Damjanovic2006] Damjanovic, D., et al. "Piezoelectric anisotropy: Enhanced piezoelectric response along nonpolar directions in perovskite crystals." Journal of materials science 41.1 (2006): 65-76.

[Devonshire1949] Devonshire, Albert Frederick. "XCVI. Theory of barium titanate: Part I." Philosophical Magazine 40.309 (1949): 1040-1063 & Devonshire, Albert Frederick. "CIX. Theory of barium titanate—Part II." Philosophical Magazine 42.333 (1951): 1065-1079.

[Devonshire1954] Devonshire, A. F. "Theory of ferroelectrics." Advances in physics 3.10 (1954): 85-130.

[Forsbergh1949] Forsbergh Jr, Peter W. "Domain structures and phase transitions in barium titanate." Physical Review, 76.8, 1187, (1949)

[Fu2000] Fu, Huaxiang, and Ronald E. Cohen. "Polarization rotation mechanism for ultrahigh electromechanical response in single-crystal piezoelectrics." Nature 403.6767 (2000): 281-283.

[Fu2000b] Huaxiang Fu and R. E. Cohen. "Piezoelectric response from rotating polarization." AIP Conference Proceedings, 535, (2000)

[Goodenough1955] Goodenough, John B. "Theory of the role of covalence in the perovskite-type manganites [La, M (II)] MnO_ {3}." Physical Review 100.2 (1955): 564.

[Jin1994] Jin, S., et al. "Thousandfold change in resistivity in magnetoresistive La-Ca-Mn-O films." Science 264.5157 (1994): 413-415.

[Kanamori1960] Kanamori, J., Phys., 31, 145 (1960)

[Kay1949] Kay, H.F. and Vousden, P., Phil. Mag., 40, 1019, (1949)

[Kittel1996] C. Kittel and P. McEuen, "Introduction to solid state physics" New York: Wiley, 1996.

[Kresin2004] Gor'kov, Lev P., and Vladimir Z. Kresin. "Mixed-valence manganites: fundamentals and main properties." Physics reports 400.3 (2004): 149-208.

[Maezono1998] Maezono, Ryo, Sumio Ishihara, and Naoto Nagaosa. "Orbital polarization in manganese oxides." Physical Review B 57.22 (1998): R13993-R13996.

[Marton2010] Marton, P., I. Rychetsky, and J. Hlinka. "Domain walls of ferroelectric BaTiO_ {3} within the Ginzburg-Landau-Devonshire phenomenological model." Physical Review B 81.14 (2010): 144125.

[Mayr2001] Mayr, Matthias, et al. "Resistivity of mixed-phase manganites." Physical Review Letters 86.1 (2001): 135-138.

[Merz1949] W.J. Merz, J. Phys. Rev., 76, 1221, (1949); W.J. Merz, J. Phys. Rev., 88, 421 (1952) and W.J. Merz, J. Phys. Rev., 95, 690 (1954)

[Nye1985] Nye, John Frederick. Physical properties of crystals: their representation by tensors and matrices. Oxford University Press, 1985.

[Park1997] Park, Seung-Eek, and Thomas R. Shrout. "Ultrahigh strain and piezoelectric behavior in relaxor based ferroelectric single crystals." Journal of Applied Physics 82 (1997): 1804.

[Park1999] Park, Seung Eek E., et al. "Crystallographic engineering in high-performance piezoelectric crystals." 1999 Symposium on Smart Structures and Materials. International Society for Optics and Photonics, 1999.

[Salomon2001] Salomon, Myron B., and Marcelo Jaime. "The physics of manganites: Structure and transport." Reviews of Modern Physics 73.3 (2001): 583.

[Schiffer1995] Schiffer, P., et al. "Low Temperature Magnetoresistance and the Magnetic Phase Diagram of La_ {1-x} Ca_ {x} MnO_ {3}." Physical Review Letters 75.18 (1995): 3336-3339.

[Shirane1996] Jona, Franco and Shirane, G. "Ferroelectric Crystals", Pergamon Press, Oxford (1962)

[vanSanten1950] Jonker, G. H., and J. H. Van Santen. "Ferromagnetic compounds of manganese with perovskite structure." physica 16.3 (1950): 337-349.

[Volger1954] Volger, J. "Further experimental investigations on some ferromagnetic oxidic compounds of manganese with perovskite structure." Physica 20.1 (1954): 49-66.

[Wang2011] Wang, Y. L., et al. "Unusual dielectric behavior and domain structure in rhombohedral phase of BaTiO< inf> 3</inf> single crystals." Journal of Applied Physics 110.1 (2011): 014101-014101.

[Wieder1957] Wieder H.H., J. Appl. Phys., 26, 1479 (1955); Wieder H.H., J. Appl. Phys., 27, 413 (1956) and Wieder H.H., J. Appl. Phys., 28, 367 (1957)

[Zener1951] Zener, Clarence. "Interaction between the d-shells in the transition metals. II. Ferromagnetic compounds of manganese with perovskite structure." Physical Review 82.3 (1951): 403.

CHAPTER 3

CHARACTERIZATION METHODS

SAMPLE PREPARATION

Samples were prepared by sputter deposition [Dam1996]. Sputtering is used extensively in industry and material science research to deposit high quality thin films. In this process atoms are ejected from a solid target material due to bombardment by, most typically Ar^+ atoms from a plasma. The ejected atoms diffuse through the plasma towards a substrate where the thin-film is deposited.

Deposition took place inside a chamber in which a high vacuum of around 10^{-6} mbar was previously realized using a turbo-molecular pump supported by a roughing pump. For oxide thin film deposition, the sputtering process was realized in high O_2 partial pressure to guarantee the proper stoichiometry as well as the oxide thin film quality. The flow of oxygen was controlled by a system of needle valves. The pressure of the highly oxidizing plasma was of 3.4 mbar and the constant growth temperature was of 1173 K. The sputtered material came from a target of manganite with the stoichiometry desired, $La_{0.7}Ca_{0.3}MnO_3$. The result of the deposition strongly depends on the magnetron, target, plasma and substrate conditions and, therefore, several parameters influence the growth of the epitaxial thin film such as the temperature of the substrate, the applied power and the pressure inside the chamber. Sample batches were annealed in situ in 700 mbar O_2 during 1 hour at 1173 K. The deposition rate was 5 Å/min.

In this thesis we used two different substrates: unpoled and/or poled $BaTiO_3$, nominally (001)-oriented, and $SrTiO_3$, (100)-oriented. Samples in both cases where grown simultaneously in exactly the same conditions. All substrates come from MaTeck and are one side polished, cut along (100) edges. Unpoled $BaTiO_3$ were used for samples described in Chapters 4-7. These substrates exhibit "a"-domains and "c"-domains in the tetragonal phase (see Chapter 2), resulting in a highly corrugated interface.

In addition, poled $BaTiO_3$ were used for the magnetoelectric coupling experiments described in Chapter 8. During fabrication, $BaTiO_3$ crystals are poled, and then sliced in pieces of 5x5x1 mm^3. This process ensures the best single crystal quality possible (see Chapter 2). In the tetragonal phase, poled $BaTiO_3$ exhibit mainly either "c"-type or "a"-type (but not both) ferroelectric domains, as confirmed with XR diffraction and atomic force microscopy. Through this text, we denote these substrates as "pre-poled" $BaTiO_3$.

STRUCTURAL CHARACTERIZATION

X-RAY DIFFRACTION

X-Ray diffraction is a fundamental technique to characterize the crystallographic structure of any solid state material and is indispensable in epitaxial thin films characterization. This technique gives information of all the important parameters that describe these systems: epitaxy, lattice parameter, relaxation ratios, strains, structural domain size, etc.

We performed X-ray characterization of $La_{0.7}Ca_{0.3}MnO_3$//$BaTiO_3$ and $La_{0.7}Ca_{0.3}MnO_3$//$SrTiO_3$ in two different geometries: coplanar (symmetric and asymmetric XRD) and grazing-incidence diffraction (GIXD). Figure 1 shows the geometry and angles definition in GIXD. Room temperature characterization was done using a Bruker four-circle XRD system with Cu $K_{\alpha 1}$ radiation (yielding an extinction length of 6.8 μm in our samples) and beam size 2 x 5 mm^2 in coplanar (XRD) geometry. Grazing-incidence (GIXD) diffraction at low temperatures was done at the ESRF SpLine beamline (BM25B) [Rubio2013, Ferrer2013], with a 6-circle diffractometer in vertical geometry. Low temperature measurements were possible thanks to a UHV "baby" chamber equipped with Beryllium walls. All synchrotron measurements were done with incident energy of 15 keV (resulting in extinction lengths close to 0.4 μm for our samples for GIXD and 1.2 μm for high resolution XRD).

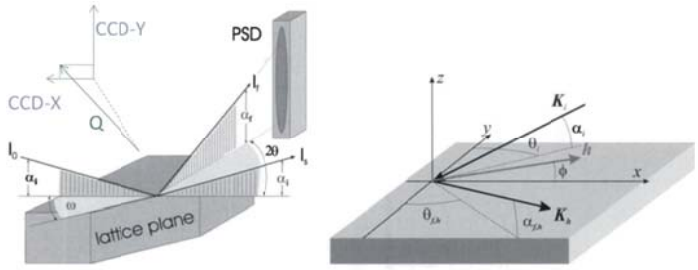

Fig.1. Geometry in GIXRD (left) and definitions of angles. Adapted from Ref. [Pietsch2004]

Two different detectors available at the ESRF Spanish beamline were used: a point detector arm for the determination of the diffraction peaks and a CCD camera for reciprocal space mapping with pixel size of 32.8 microns square and resolution 7651 x 3825 pixels. The experimental setup in the BM25B is shown in Fig. 2.

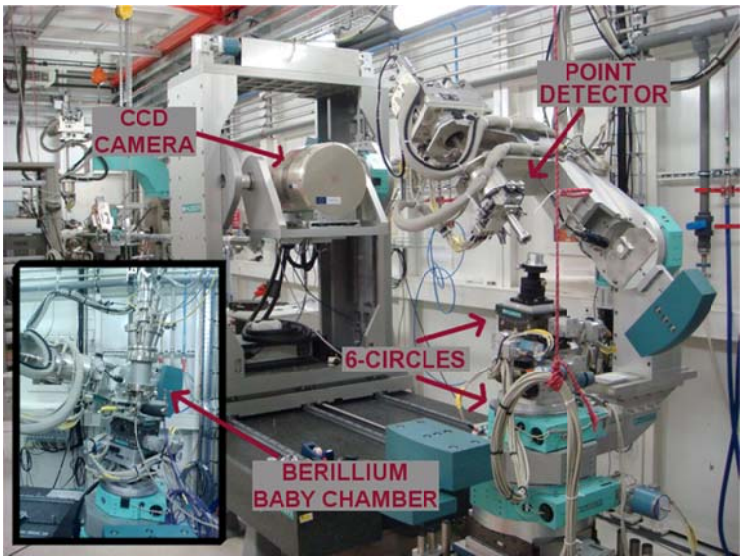

Fig.2. View of the ESRF SpLine BM25B diffractometer.

In the process of obtaining reciprocal space maps with the CCD camera, this protocol was followed: first, using the point detector, the exact position of the substrate peak (i.e. [h,k,l] of the particular reflection selected) was determined. That is, the angles $\{\mu, \theta, \varphi, \chi, \delta, \gamma\}_{lab}$ were determined (See Fig. 3), where μ is the incident angle (denoted as α_i in Fig. 1.), θ is the Bragg angle of the [h,k,l] reflection in the lab reference system, φ and χ are used to adjust the sample surface and, δ and γ the point detector angles in the horizontal and vertical rotations respectively. Then the point detector was moved away and substituted by the CCD camera. The pictures taken with the CCD were always at least two for each reflection and temperature: one for the substrate peak (short exposure time) and another for the thin film peak (long exposure time and masked substrate peak).

Thus, the position of the substrate and thin film peaks were determined with the maximum experimental accuracy available.

Each peak registered in GIXD in a CCD camera picture is defined by two coordinates $\{x_{CCD}, z_{CCD}\}$, that is, its position with respect to the CCD origin. These positions are linked to the detector angles $\{\delta, \gamma\}$ by trigonometric relations (see Fig. 1). After transforming the set of angles $\{\theta, \varphi, \chi, \delta, \gamma\}_{lab}$ to the sample reference system $\{\theta, \varphi, \chi, \delta, \gamma\}_{sample}$, via the orientation matrix [Rubio2013, Ferrer2013], it is possible, using x-ray diffraction theory to calculate the indexes [h,k,l], lattice parameters (a,b,c) or the vector **Q** for both substrate and thin film [Pietsch2004]. The general equations needed are:

$$\begin{aligned} Q_x &= K(\cos\alpha_f \sin\theta_f + \cos\alpha_i \sin\theta_i) \\ Q_y &= -K(\cos\alpha_f \cos\theta_f + \cos\alpha_i \cos\theta_i) \\ Q_z &= K(\sin\alpha_f + \sin\alpha_i) \end{aligned} \qquad [1]$$

Throughout this thesis, the nomenclature used in relation to structural characterization is the one used in Ref. [Pietsch2004].

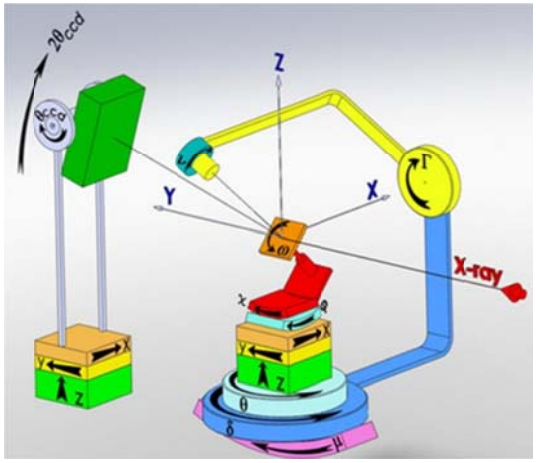

Fig.3. Scheme and angles definition of the BM25B Spanish Beamline at ESRF 6-circles station. Adapted from Ref. [Rubio2013]

ATOMIC FORCE MICROSCOPE

Atomic Force Microscope (AFM) [Binnig1982, Binnig6] is a high resolution technique used in surface characterization. AFM measures the interaction between a sharp probe (the tip) and the studied sample with nanometric or even atomic lateral resolution giving three dimensional profiles of the sample surface. The nm range distance between the tip and the sample enables sensing very small forces in the 10^{-13}-10^{-5} N range. The specific property being measured depends on the nature of the force sensed by the tip (repulsive, attractive Van der Waals, magnetic, electrostatic…)[Meyer2004]. In this thesis the AFM technique has been used mainly to characterize the morphology of the sample surface, sensing the attractive Van der Waals forces between tip and sample, in dynamic mode.

Two AFM systems have been employed for morphological characterization: a room-temperature commercial AFM (RT-AFM) from Nanotec™ and a low-temperature commercial AFM (LT-AFM) from Nanomagnetics Instruments. The latter allows performing measurements in a temperature range from 300K to 1.7K. The measurements have been performed in the dynamic operation mode, which includes intermittent and non-

contact mode. In this mode cantilever is set to oscillate near its resonance frequency, at distance typically below 30nm from the sample surface. The forces between tip and sample are thus sensed by measuring the changes produced in the cantilever´s oscillation amplitude, frequency and phase when the tip gets close to the sample.

In the RT-AFM system, this is achieved with the beam deflection method in which a laser beam is focused on the rear side of the cantilever and its reflection detected by a Position Sensitive Photodiode [Meyer1990]. On the contrary, our LT-AFM employs optical interferometry in order to detect changes in cantilever´s oscillation due to tip-sample interaction [Rugar1989]. Upon comparing the signal measured (amplitude, in this work) with a user-specified set-point, and electronic feedback systems sends a signal to a piezoelectric tube located under the sample, to retract or expand in order to re-establish the value of the set-point. Such contractions/expansions are registered and when plotted as a function of the scanning area represent the topography image of the sample. The piezoelectric tubes mentioned above control not only the z movement, but also the xy scans. Maximum scan area at RT is 100µm x 100µm. At low temperatures this value decreases to 18µm x 18µm at 4.2K.

Cantilevers with integrated tips are commercially produced by standard microfabrication techniques, mostly from silicon or silicon nitride. The later use of a coating layer allows producing tips with different surface properties (conductive, magnetic…). In this work, sharp silicon AFM probes from Nanosensors (tips radii below 10nm) have been used with force constants, *k*, around 2.8N/m and resonance frequencies in the 150-180 kHz range. Prior to imaging, samples were systematically cleaned with acetone and isopropanol in an ultrasonic bath. Image processing was done using the WSxM commercial software[Horcas2007].

POLARIZED NEUTRON REFLECTOMETRY

Polarized neutron reflectometry (PNR) is a widely used technique in the study of magnetic surfaces and interfaces [Majkrzak2004]. In the general sense, measuring reflectivities implies measuring the variation of the intensity of a reflected beam in a process that varies with the depth dependent refractive index of the material. When using polarized neutrons [Squires2012], the interaction of the magnetic moment of the neutron with the magnetic moments in the specimen allows the magnetic characterization and the magnetic depth profiles can be obtained. In these magnetic profiles the lateral dimensions are averaged. PNR can measure magnetic densities as small as 30 emu/cm^3 and it is sensitive to fractions of nanometer [Majkrzak2005]. For this reason, PNR is of great interest in the study of magnetic thin films as the heterostructures studied in this thesis.

Neutron reflectometry is studied in terms of the reflection of neutrons by the scattering potential of the material, which includes two interactions: nuclear interaction (V_n) and the interaction with the atomic magnetism (V_m) of the material. This second interaction is fundamental in PNR and it is expressed as $V_m = \mp \underline{\mu} \mathbf{B}$, where $\underline{\mu}$ is the magnetic moment of the neutron and $\mathbf{B}$ is the magnetic induction which is related to the intensity of the magnetization in the material by $\mathbf{B} = \mu_0 \mathbf{H} + \mathbf{M}$. The sign of this interaction is chosen to be negative (positive) when the neutron spin is parallel (antiparallel) to the laboratory magnetic field of reference ($\mathbf{H}$).

The neutron scattering length density (ρ, in Å^{-2}) is expressed as the sum of two terms, nuclear and magnetic. When using polarized neutrons two cases can be encountered depending of the relative orientation of the magnetization of the material: non-spin-flip (NSF) and spin-flip (SF) scattering potentials. In the first case, the neutron magnetic moment is either parallel or antiparallel to $\mathbf{M}$ and no rotation of the neutron spin occurs, then, the cross sections are R^{++} and R^{--} (see Fig. 4). If the magnetization of the material forms an angle θ with the

magnetic field, the neutron spin can be rotated when interacting with the material, the reflectivities in this case are R^{+-} and R^{-+} as shown in Fig. 4.

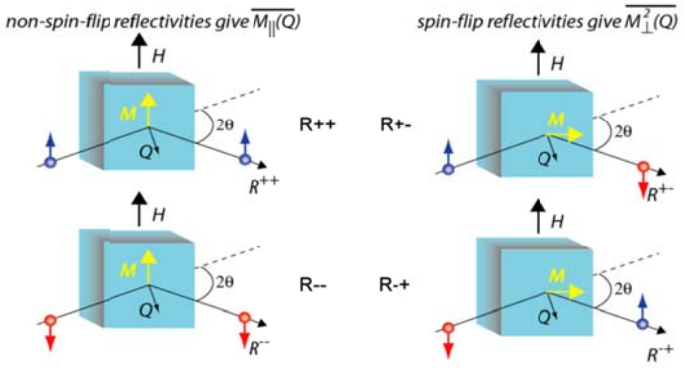

Fig.4. Spin flip and non-spin flip reflectivities. Adapted from Ref. [PynnTalk]

PNR was performed at the Asterix reflectometer (Lujan Neutron Scattering Center at LANSCE) in order to investigate the depth profiles of magnetization for both $La_{0.7}Ca_{0.3}MnO_3$//$BaTiO_3$ and $La_{0.7}Ca_{0.3}MnO_3$//$SrTiO_3$. For this purpose, 10 x 10 mm^2 samples were prepared in the same conditions specified in Section I. For polarized neutron reflectometry experiments, samples were cooled in zero field to 120 and 30 K ($La_{0.7}Ca_{0.3}MnO_3$//$BaTiO_3$) and 90 K ($La_{0.7}Ca_{0.3}MnO_3$//$SrTiO_3$), that is, at the same temperature relative to the Curie temperature for each sample. Subsequently, a saturating magnetic field (0.6 T or 1.0 T) was applied in-plane, along the sample easy axis. Both NSF and SF neutron cross sections were explored near the critical angle. In the absence of measurable SF signals, only NSF (R^{++} and R^{--}) reflectivities were recorded as a function of momentum transfer, **Q**. This implies that, within the sensitivity of the technique, all detected magnetic moment is in-plane and aligned with the applied field (M||). PNR NSF Reflectivities were analyzed using the *co_nevot_croce* code which implements Parrat's formulation to extract nuclear and M|| magnetic scattering length profiles [Majkrzak2004]

FERROMAGNETIC RESONANCE

The magnetic anisotropy of magnetic materials and thin films can be studied using Ferromagnetic Resonance (FMR). One of the major advantages of this technique is that it allows the exact determination of the magnetic anisotropy constants of a magnetic system (and their dependence with temperature) by solving its equations of motion. The second advantage is that FMR allows the study of the magnetic interaction (ferromagnetic coupling) between different magnetic materials in multilayered structures.

FMR determines magnetic properties by measuring the absorption of microwaves due to the precessional motion of the magnetization (**M**) in a ferromagnetic sample around the internal magnetic field ($\mathbf{B}_{eff}$) due to the externally applied magnetic field ($\mathbf{B}_{applied}$). Since sweeping the microwave frequency is experimentally difficult over large ranges, FMR is often measured by irradiating the sample with a fixed microwave (typically on the order of tens of GHz) and sweeping the applied magnetic field. When the precessional or Larmor frequency at a certain magnetic field coincides with the microwave frequency (resonance condition) the microwave power absorption takes place [Kittel1948, Slichter1992], see Fig. 5. The absortion signal has the shape of a Lorentzian. The resonance field and the width of the absorption curve depend of the relative angle between $\mathbf{B}_{applied}$ and the thin film crystallographic axis, which is related to the anisotropy of the system, the gyromagnetic factor and the magnetization of the sample. Usually, the derivative spectra are recorded at several orientations angles [Zsolt2008].

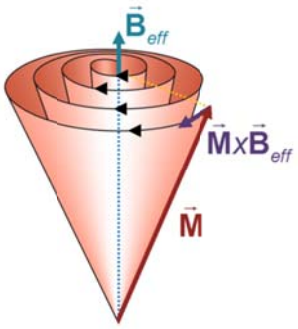

Fig.5. Illustration of the precession motion of the magnetization vector due to $\mathbf{B}_{eff}$ in the process of ferromagnetic resonance.

For the FMR studies in Chapter 7, twin samples of t = 120 Å thick $La_{0.7}Ca_{0.3}MnO_3$ were grown on $SrTiO_3$ [100] and $BaTiO_3$ [100] substrates. A thicker, t = 150 Å $La_{0.7}Ca_{0.3}MnO_3$//$BaTiO_3$ was also studied. After growth, the 1mm thick substrates were cut to 2mm*2mm areas with a diamond saw. The samples were fixed with vacuum grease (DowCorning) to small cylindrical Teflon® pieces and finally sealed in 4mm OD quartz EPR tubes under 20mbar He exchange gas. This arrangement permitted both placing the ampoules directly into liquid nitrogen at 77K their rotation around an axis perpendicular to the applied magnetic field. The rotation axis was chosen along either of the various crystallographic axes of the substrate: [001] for field rotating in-plane and [100] or [110] for field rotating away from the film plane along one or the other principal directions. The sample holders allowed 1° accuracy for the alignment of the sample axis with respect to the rotation axis, whereas the manual rotation of the ampoules invoked an angular accuracy of approx. 3°. For each orientation, spectra were recorded as a function of rotation angle (θ) at every approx. 5° over almost the full 360°. Each recorded spectrum is a derivative of the magnetic field dependent microwave absorption. The spectra are analyzed with least squares fitting of derivative Lorentzian lines, using an admixture of absorptive and dispersive contributions to account for the metallic and dielectric distortion effects of the film and ferroelectric substrate.

Fig.6. View of the FMR spectrometer in Budapest, adapted from Ref. [Zsolt2008]

MAGNETIC AND TRANSPORT MEASUREMENTS

MAGNETISM

Temperature- and magnetic-field-dependent magnetization dependence was measured using a vibrating sample magnetometer (VSM) and a Physical Property Magnetic System (PPMS) or, alternatively, a superconducting quantum interference device (SQUID) magnetometer, both from Quantum Design, and equipped with 9-14T and 5-T coils, respectively.

The PPMS Dewar consists of an inner liquid helium reservoir and outer liquid nitrogen jacket, to reduce excessive liquid helium to boil off. The liquid helium is used both for maintaining the superconducting state and of cooling the sample space. PPMS systems allow characterization of several physical properties, such as resistivity, magnetism, specific heat… just by connecting each option to the inner electronic of the PPMS using pucks as the one show in Fig. 7 for the VSM.

VSM basic measurement is accomplished by oscillating the sample near a detection (pickup) coil and synchronously detecting the voltage induced. By using a compact gradiometer pickup coil configuration, relatively large oscillation amplitudes (2mm) and a frequency of 40 Hz, the system is able to resolve magnetization changes around 10^{-6} emu. This feature is relevant when measuring ultra-thin films. The sample is attached to the end of a sample rod that is driven sinusoidally (see Fig. 7) the field being always in the plane of the $La_{0.7}Ca_{0.3}MnO_3$ film, unless indicated otherwise.

Fig.7. Schematic representation of the linear motor and coil-set of the standard quantum design VSM option. Adapted from QD instrumentation notes.

The magnetization is usually reported here as magnetic moment per Mn ion of the $La_{0.7}Ca_{0.3}MnO_3$ films in Bohr magnetons (μB/Mn). The bulk saturation value in $La_{0.7}Ca_{0.3}MnO_3$ is 3.7 μB/Mn. Magnetization hysteresis loops were recorded at various temperatures, after cooling to 10 K in 1 T, between ±1 T with a slow sweep rate of 1–2 mT/s. The diamagnetic contribution of the substrates was subtracted by estimating the high field linear dependence above the saturating field of $La_{0.7}Ca_{0.3}MnO_3$.

Zero field cooled (ZFC) and field cooled (FC) temperature dependent magnetization for 120 Å $La_{0.7}Ca_{0.3}MnO_3$//$SrTiO_3$ and $La_{0.7}Ca_{0.3}MnO_3$//$BaTiO_3$ were recorded in two different magnetic fields 100 Oe and 1000 Oe. In a typical ZFC, the sample is cooled in 0 Oe and then warmed in 100 or 1000 Oe; in a FC, the sample is cooled and warmed in the same magnetic field (100 or 1000 Oe, in our case). Curves considered as ZFC-FC are the ones taken while warming after cooling in zero or non-zero field.

DIAMAGNETIC AND PARAMAGNETIC CORRECTIONS

When characterizing magnetism in thin films with macroscopic probes, as in the case of the PPMS-VSM systems, it shall be noted that the signal measured includes not only the thin film magnetic moment but all possible diamagnetic or paramagnetic moments coming from the substrate or impurities/contaminations in the sample and sample-holder. Therefore, proper characterization of the thin film requires the subtraction of all the extra moments not related to the thin film.

The case of the diamagnetic substrates is simple. The diamagnetic moment is constant with temperature and depends linearly with the magnetic field: $\mathbf{M}=\chi\mathbf{H}$, where χ is the magnetic susceptibility and negative, then the subtraction of this component is straightforward. Paramagnetism, on the other hand, may be more complicated, especially when due to impurities or contamination (commonly with silver paint or similar) in the sample. In any case, paramagnetism appears as an extra component with $\chi > 0$ that is proportional to the inverse of the temperature ($\chi \propto 1/T$, Curie's law) [Cullity2011]. Finally, to correct the raw data the following expression must be used:

$$m(T,H) = m_{raw}(T,H) - \chi(T,H)H \qquad [2]$$

Where m(T,H) is the magnetic moment at each temperature and applied magnetic field of the thin film after correcting the extra components from the signal measured with the VSM or SQUID, m_{raw}, given in emu. $\chi(T)$ in expression [2] denotes de slope of the magnetic loop in emu/Tesla.

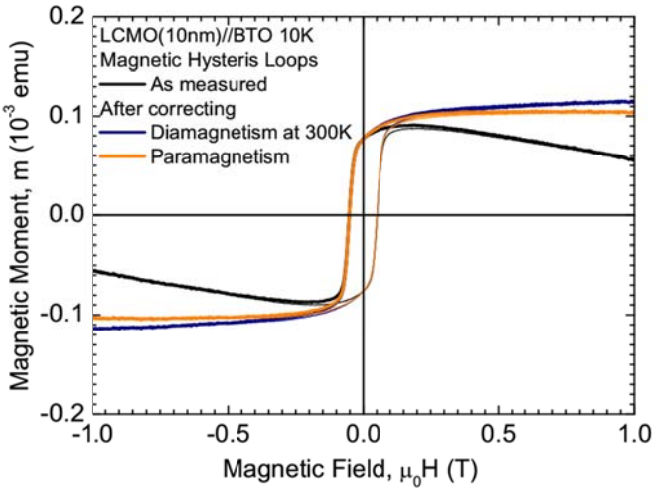

Fig.8. Magnetic hysteresis loops measured at 10K for a sample of $La_{0.7}Ca_{0.3}MnO_3$//$BaTiO_3$ of 10 nm showing the different signals extracted during the diamagnetism and paramagnetism correction.

In Figure 8 we show an illustrative example. Black curve is the magnetic loop as measured using the SQUID, in this case. The magnetic hysteresis loop shown in blue is obtained after correcting with the diamagnetic signal at 300K (where the manganite is not ferromagnetic). An identifiable paramagnetic contamination with silver paint (used in a previous measurement of this sample) can be appreciated as a steady increase of the magnetization with magnetic field in the magnetic loop branch. The magnetic loop shown in orange is the final curve after correcting the paramagnetic and diamagnetic signals. It shall be noted that similar corrections must be applied to the moment versus temperature curves.

CORRECTION OF THE MAGNETIC FIELD OFFSET IN PPMS SYSTEMS

The magnetic field reported in Quantum Design PPMS systems is based solely on the current flowing from magnet power supply and is not measured directly. But superconducting magnets, especially those that reach high magnetic fields (up to 14T in our lab) may be affected by pinned magnetic flux lines and flux movement within the magnet that in turn may change the magnetic field near the sample. That is, the reported magnetic field is different than the real magnetic field applied [QD1070-207]. The offset in the magnetic field reported is defined as:

$$H_{offset} = H_{real} - H_{PPMS} \qquad [3]$$

where H_{real} is the real magnetic field applied, H_{PPMS} is the reported magnetic field and H_{offset} is the resultant offset. The offsets in the PPMS-9T and PPMS-14T used in this thesis are of the order of 13 Oe and 100 Oe, respectively. Nevertheless, due to variation in the pinned currents when sweeping to high magnetic fields these offsets may change from one measurement to the other and in consequence, if experiments at low magnetic fields are intended, it is important to previously characterize these offsets. H_{offset} will be different when sweeping the magnetic field at different speeds (the available options range between 13 Oe/s to 113 Oe/s); it may be different decreasing or increasing the magnetic field and may be slightly affected by temperature.

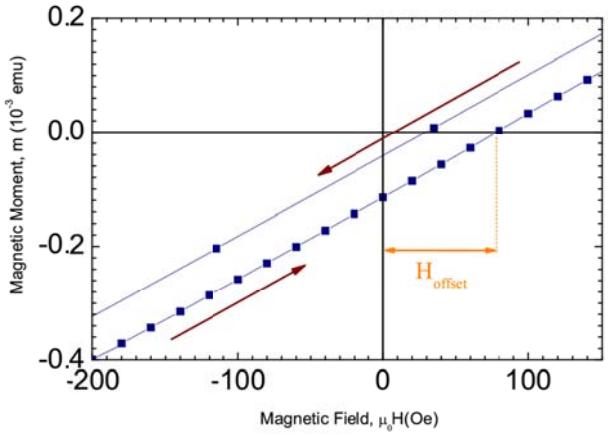

Fig.9. Moment vs. magnetic field measured at room temperature for a pure paramagnetic Pd sample. The sequence in this case was as follows: 1) sweeping down in field from 10^4 Oe at 131 Oe/s to -10^3 Oe; 2) Sweeping up to 100 Oe at the lowest speed allowed (13 Oe/s). Notice that the H_{offset} is different for different sweeping speeds.

The determination of the offsets when using the VSM option can be realized by previously measuring a standard pure paramagnetic Pd sample at room temperature (or any other T), following the exact sequence that is going to be used later.

- *Magnetic Hysteresis Loops*

Since the magnetic field sweeping speed may change the offset, it is important to measure the m(H) curves exactly as they are going to be measured in the experiment of interest. As a pure paramagnetic sample (free of ferromagnetic impurities), the m(H) curves measured in Pd samples must look like an straight line with zero coercive field and positive slope, however, due to the magnet offset, a deviation from zero will be found, this is our H_{offset} for these magnetic hysteresis loops. Note that this offset may be slightly different between up and down sweeps in magnetic field.

- *Moment versus Temperature Curves*

When measuring moment vs. temperature curves at very low magnetic fields (ZFC or FC at 100 Oe, for example) the accurate determination, previous to the experiment, of H_{offset} is essential. Figure 9 shows a way to do this correction. By following the same magnetic field path and exact sweeping speeds it is possible to set the desired magnetic field with an error of just 3 Oe. For example, for a ZFC measurement, setting the magnetic field to zero implies setting the field to H_{offset} after following a path as the one described in Fig. 9. This path is not unique and may be adapted according to the interest of the measurement desired.

ELETRONIC AND MAGNETIC TRANSPORT

Characterization of electronic transport in manganites is essential since in these compounds ferromagnetism and conductivity are strongly related (see Chapter 2). In this sense, transport measurements are an excellent macroscopic probe to study the microscopic magnetic ordering in $La_{0.7}Ca_{0.3}MnO_3$ thin films due to the high sensitivity to conducting paths that may appear in the phase segregated manganite.

Electronic transport and magnetoresistance were characterized by measuring the resistance of the film in plane with the van der Pauw method [Pauw1958], with contacts placed in the four corners of the square shaped samples and using PPMS systems for low temperature and high magnetic fields experiments. When required due to high resistance of the thinner samples, a Keithley 2410 source meter connected to the PPMS was used. Magnetoresistance (MR) was calculated by normalizing to the zero-field resistance.

In electroresistance measurements, we used a Keithley 6221 (low AC and DC current source) to apply a dc excitation current alternating its direction to eliminate thermoelectric voltages, in combination with a Keithley 2182A nanovoltmeter to measure the voltage. Furthermore, readings were taken quasi-simultaneously, with the excitation current passed along one or the other perpendicular edges of the sample, parallel to the applied magnetic field. In order to discern and eliminate Joule-heating effects, at several temperatures, pulsed I-V curves were recorded. Electroresistance (ER) was calculated from the nonlinear I-V curves as described in Chapter 6.

EXPERIMENTAL SET UP FOR CONVERSE MAGNETO-ELECTRIC EFFECT MEASUREMENTS

Magnetic measurements of the converse magnetoelectric effect were performed using the VSM-PPMS as described before. For the application of external voltages, we built a sample holder and sample rod modified accordingly: two wires of Manganin® alloy were attached along the rod with dental floss and contacted to the sample with silver paint. Voltages up to 500 V/mm were applied externally using a Keithley 2410. To avoid electric currents and sparking, the PPMS sample chamber was put at high vacuum when applying the voltages. Figure 10 shows a sample holder and a sample attached to it. Silver paint or epoxy was used to contact the bottom and top of the sample to the Manganin® wires.

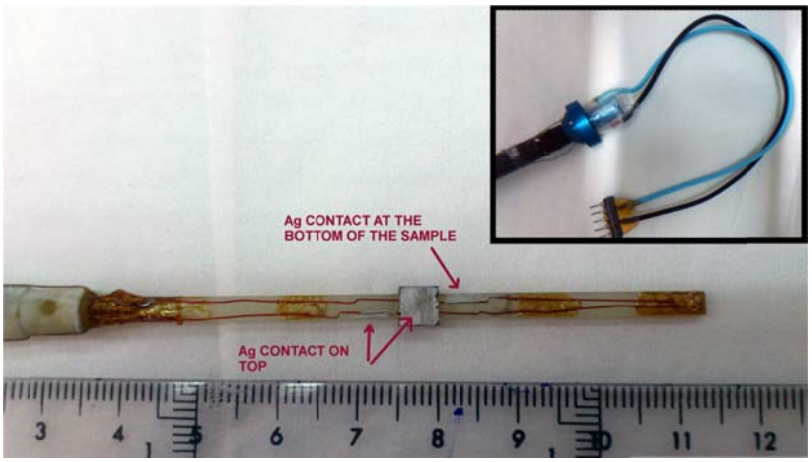

Fig.10. View of the sample holder and modified VSM rod used in the Inverse Magnetoelectric Measurements. Manganin® wires were attached along the sample rod to the sample and then contacted with Ag. Inset shows the upper side of the sample rod with pins that connect the sample.

REFERENCES

[Binnig1982] Binnig, Gerd, et al. "Surface studies by scanning tunneling microscopy." Physical review letters 49.1 (1982): 57-61.

[Binnig1986] Binnig, Gerd, Calvin F. Quate, and Ch Gerber. "Atomic force microscope." Physical review letters 56.9 (1986): 930-933.

[Cullity2011] Cullity, Bernard Dennis, and Chad D. Graham. Introduction to magnetic materials. Wiley-IEEE Press, 2011.

[Dam1996] Dam, B., et al. "Growth and etching phenomena observed by STM/AFM on pulsed-laser deposited YBa2Cu3O 7− δ films." Physica C: Superconductivity 261.1 (1996): 1-11.

[Ferrer2013] Pilar Ferrer, et al., J. Synchrotron Rad., 20, 474–481, (2013)

[Horcas2007] Horcas, I., et al. "WSXM: A software for scanning probe microscopy and a tool for nanotechnology." Review of Scientific Instruments 78 (2007): 013705.

[Kittel1948] Kittel, Charles. "On the theory of ferromagnetic resonance absorption." Physical Review 73.2 (1948): 155.

[Majkrzak2004] C.F. Majkrzak, K.V. O'Donovan and N.F. Berk "Polarized Neutron Reflectometry" Chapter 1, April 16, (2004)

[Majkrzak2005] M.R. Fitzsimmons and C.F. Majkrzak, "Application of polarized neutron reflectometry to studies of artificially structured magnetic materials, in Modern Techniques for Characterizing Magnetic Materials", ed. by Y. Zhu (Kluwer, Boston 2005), pp. 107-152.

[Meyer1990] G. Meyer, N. M. Amer. "Simultaneous measurement of lateral and normal forces with an optical-beam-deflection atomic force microscope" 1990 Appl. Phys. Lett. 57; 2089.

[Meyer2004] E. Meyer, H. J. Hug, R. Bennewitz. "Scanning Probe Microscopy. The lab on a tip" 2004, Springe-Verlag, Berlin, Germany.

[Pauw1958] van der PAUW, L. J. "A method of measuring specific resistivity and Hall effect of discs of arbitrary shape." (1958).

[Pietsch2004] Pietsch, Ullrich, Vaclav Holy, and Tilo Baumbach. "High-resolution X-ray scattering: from thin films to lateral nanostructures". Springer, 2004.

[Poole1967] C. P. Poole: Electron Spin Resonance – A Comprehensive Treatise on Experimental Techniques (Interscience Publishers, New York, 1967).

[PynnTalk] R. Pynn lecture on "Neutron Reflectometry" that can be found at http://www.che.udel.edu/cns/pdf/Reflectometry.pdf

[QD1070-207] Quantum Design Application Note 1070-207 "Using PPMS Superconducting Magnets at Low Fields" that can be found at http://www.qdusa.com/sitedocs/appNotes/ppms/1070-207.pdf

[Rubio2013] J.Rubio Zuazo, et al., Nuclear Instruments & Methods In Physics Research A, (2013)

[Rugar1989] Rugar, D., H. J. Mamin, and Peter Guethner. "Improved fiber-optic interferometer for atomic force microscopy." Applied Physics Letters 55.25 (1989): 2588-2590.

[Slichter1992] C. P. Slichter: Principles of Magnetic Resonance, 3rd Enlarged and Updated Edition (Springer-Verlag, Berlin, 1992).

[Squires2012] Squires, Gordon Leslie. Introduction to the theory of thermal neutron scattering. Cambridge University Press, 2012.

[Zsolt2008] Szatmári Zsolt, "Mágneses vékonyrétegek elektronspin-rezonanciás vizsgálata", Diplomamunka, (2008)

CHAPTER 4

$La_{0.7}Ca_{0.3}MnO_3$//$BaTiO_3$ STRUCTURAL CHARACTERIZATION

In this chapter we concentrate on the structural characteristics of $La_{0.7}Ca_{0.3}MnO_3$//$BaTiO_3$ thin films and we compare them with $La_{0.7}Ca_{0.3}MnO_3$//$SrTiO_3$ control samples.

As described in Chapter 2, $BaTiO_3$ substrates are ferroelectric at all temperatures below the Curie point, T_c = 393K, in the tetragonal, orthorhombic and rhombohedral phases. Misfit strain due to differences in lattice parameters between the $La_{0.7}Ca_{0.3}MnO_3$ layer and the substrate, ferroelectric domain walls, corrugation at the interface, and a manganite especially prone to phase separation, trigger new magnetic and transport phenomena. The microscopic properties described in this chapter are at the origin of the strong magnetoelastic and magnetoelectric coupling studied later in this thesis.

STRUCTURE AT ROOM TEMPERATURE

In the following, we summarize the room temperature characterization of $La_{0.7}Ca_{0.3}MnO_3$//$SrTiO_3$ and $La_{0.7}Ca_{0.3}MnO_3$//$BaTiO_3$ heterostructures as published in Ref. [Alberca2012]. In this text, we follow the terminology and definitions found in Ref. [Pietsch2004], unless indicated otherwise, for all the variables considered.

We first start with samples grown on $SrTiO_3$ substrates. $SrTiO_3$ bulk has a cubic perovskite structure above 105 K (space group $Pm\bar{3}m$), with unit cell parameter a = 3.905 Å. Below that temperature, a transition to tetragonal phase takes place. The maximum tetragonality is found at the lowest temperature measured (~10K) with lattice parameters a = 3.897 Å and c = 3.903 Å, and tetragonality c/a = 0.15% [Loetzsch2010].

Room temperature reciprocal space maps of $La_{0.7}Ca_{0.3}MnO_3$//$SrTiO_3$ samples are shown in Fig. 1 for two different reflections: near the symmetric (200) and near the asymmetric ($\bar{1}03$). $La_{0.7}Ca_{0.3}MnO_3$ grows epitaxially on $SrTiO_3$ and exhibits a large degree of spatial coherence. The full width at half maximum (FWHM) in the H-direction for the $La_{0.7}Ca_{0.3}MnO_3$ peak near the (200) reflection is limited by instrument resolution, indicating the quality of these thin films, and the FWHM of the L-direction allow us to determine the thin film coherence length [Pietsch2004] in the out of plane direction which is 120Å, that is, basically the thickness of the thin film. The asymmetric ($\bar{1}03$) reflection [Fig. 1(b)] shows the $La_{0.7}Ca_{0.3}MnO_3$ peak aligned along the $SrTiO_3$ crystal truncation rod, at H = -1. The in-plane parameter of the thin film is exactly the substrate parameter, resulting in a fully constrained sample with R = 0. R is the relaxation coefficient, defined as $R = (a_L - a_S)/(a_P - a_S)$ with a_L the layer in plane lattice parameter, a_P the bulk parameter and a_S the substrate in plane parameter [Pietsch2004].

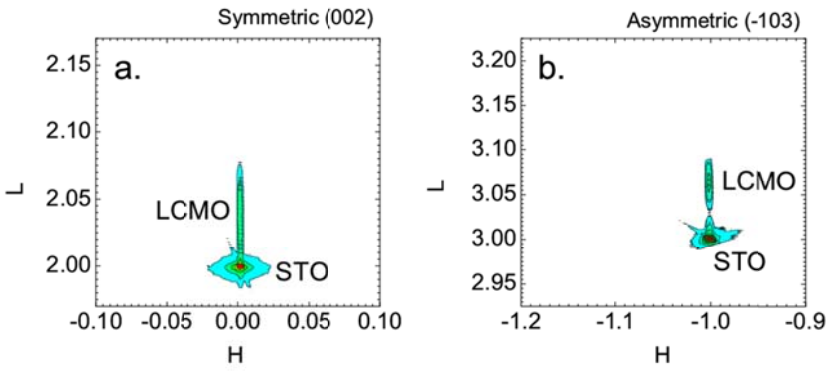

Fig.1. Room temperature coplanar XRD reciprocal space maps of a) the symmetric reflection [002] and b) the asymmetric reflection (-103) of $La_{0.7}Ca_{0.3}MnO_3$//$SrTiO_3$.

TABLE I. Room temperature parameters for 120Å thick $La_{0.7}Ca_{0.3}MnO_3$//$SrTiO_3$ and $La_{0.7}Ca_{0.3}MnO_3$//$BaTiO_3$. In-plane parameters extracted from the asymmetric reflections near ($\bar{1}03$) and out-of-plane parameters extracted from the symmetric reflections near (200).

SAMPLE		LCMO Pseudocubic Lattice Parameters (Å)		L_a	L_c	R
		In-plane	Out-of-plane			
LCMO/STO		3.905	3.824 (±0.003)	--	105	0.00
LCMO/BTO (relaxed)	"a" domains	3.91 (±0.02)	3.83 (±0.01)	78	93	0.69
	"c" domains		3.85 (±0.01)		93	
LCMO/BTO (unrelax.)		3.96 (±0.02)	3.85 (±0.01)	40	99	0.19

We now concentrate on the case of $La_{0.7}Ca_{0.3}MnO_3$//$BaTiO_3$. As discussed in Chapter 2, at room temperature $BaTiO_3$ substrates are tetragonal with a tetragonality of c/a = ~1%. Consequently, for each nominal reflection at least two peaks are expected, corresponding to "a" and "c" domains of tetragonal $BaTiO_3$. Figures 2(a) and (c) show reciprocal space maps near the nominal (002) reflection. The peaks labeled as (200) correspond to the "a" domains (for these domains the polar axis lies in plane) and the peaks labeled as (002) correspond to "c" domains (with polar axis aligned normal to the substrate surface). We observed that not only as-received unpoled $BaTiO_3$ substrates but also *freshly prepared* samples showed these two peaks. But upon thermal cycling and switching, each of these peaks evolved into several less intense peaks with different H values [Fig. 2(c)]. This is due to the formation of "slabs" (macroscopic flat areas in the substrate separated by defects) with slightly different orientations, and therefore, slightly different Bragg angles. The angle between domains labeled (200) and (002) in Figure 2(a), is the expected corrugation angle 0.6º in agreement with observations in $BaTiO_3$ single crystals described in Chapter 2.

The differences with respect to $La_{0.7}Ca_{0.3}MnO_3$//$SrTiO_3$ are noticeable. First, their considerably broader peaks [Fig. 2(c), and Table I] result in smaller coherence lengths of 200 Å (in-plane) and (70-90) Å (out-of-plane). $La_{0.7}Ca_{0.3}MnO_3$ thin films are partially relaxed. The relaxation coefficient R varies in the range between 0.2 and 0.7. In Figure 2, upper panels belong to a highly relaxed sample (R = 0.7) and lower panels show a less relaxed sample (R = 0.2).

In the next section, we shall describe how $La_{0.7}Ca_{0.3}MnO_3$ adapts closely to the structural changes of $BaTiO_3$. A hint of these can be seen in the symmetric reflection depicted in Figure 2(a), where two different slabs of

$BaTiO_3$ that belong to "a"- and "c"-domains result in two resolved $La_{0.7}Ca_{0.3}MnO_3$ peaks. Considering these two $La_{0.7}Ca_{0.3}MnO_3$ peaks we calculate their associated out of plane parameters as $c_a = 3.83 \pm 0.01$ Å and $c_c = 3.85 \pm 0.01$ Å on "a"- and "c"-domains, respectively. Thus, the change in the out of plane parameter of the $La_{0.7}Ca_{0.3}MnO_3$ is ~0.5%.

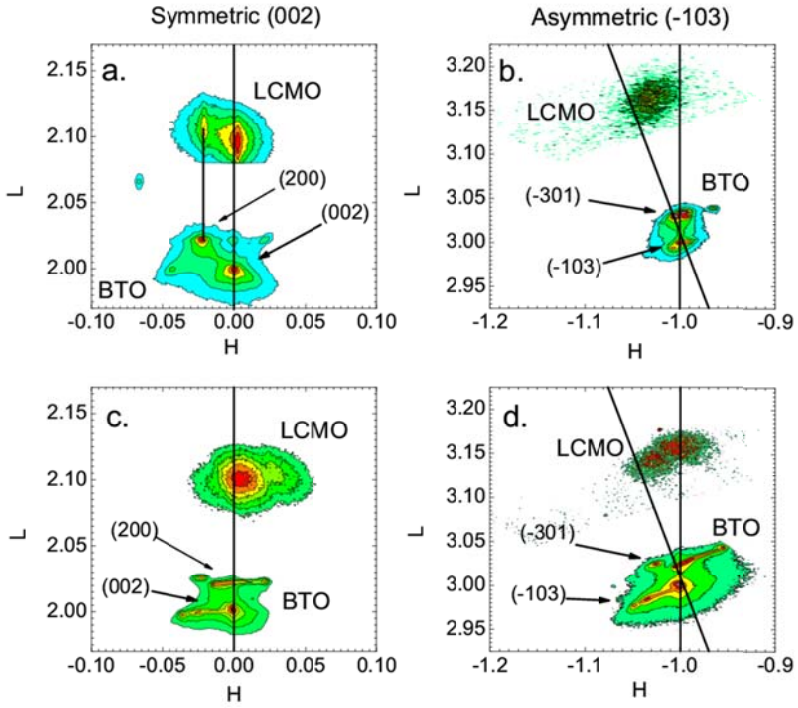

Fig.2. Room temperature coplanar XRD reciprocal space maps for two $La_{0.7}Ca_{0.3}MnO_3$//$BaTiO_3$ samples (upper and lower panels), for symmetric (a and c) and asymmetric (b and d) reflections, as indicated.

LOW TEMPERATURE CHARACTERIZATION

Given our interest in the physics of the low temperature (T<200K) phase of $La_{0.7}Ca_{0.3}MnO_3$ thin films, structural characterization at low temperatures is needed [Alberca2011, Alberca2012]. For this purpose, Grazing-incidence (GIXD) diffraction at low temperatures was done at the ESRF SpLine beamline (BM25B), with a six-circle diffractometer (see Chapter 3). In Chapter 2 the lower temperature phases of the substrate were considered, highlighting the complexity derived from the domain formation.

Let us start then with the reciprocal space maps of the substrate in coplanar geometry. Figure 3 shows the reciprocal space maps for $BaTiO_3$ in the three ferroelectric phases as recorded on the Bruker 4-circle diffractometer using a purpose-made low temperature sample chamber. The tetragonal phase [Fig. 3(a)] is, as described above, characterized by the presence of peaks corresponding to the "a"- and "c"-domains. In this case, the alignment was done with respect to the "a" domains, which were found to be majority in this sample. The calculated corrugation angle was, as expected, 0.6º. The domain pattern in the orthorhombic phase can be observed in Fig. 3(b). This phase shows similar reciprocal space maps as the tetragonal phase, but with slightly smaller misorientation angle of 0.5º. In the rhombohedral phase at 77 K [Fig. 3(c)], only two peaks, of almost equal intensity, are apparent with the expected relative misorientation of 0.27º. In our experiments, lattice parameters and misorientation angles in the three phases of $BaTiO_3$ were in agreement with those found in literature (see Chapter 2 and references therein).

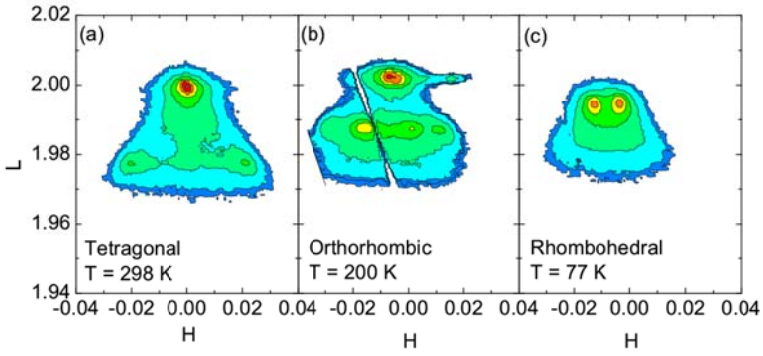

Fig.3. Coplanar XRD reciprocal space maps of $BaTiO_3$ in its three ferroelectric phases.

The evolution with temperature of the structure of $La_{0.7}Ca_{0.3}MnO_3$ layers was studied by synchrotron x-ray diffraction at the ESRF SpLine beamline using both coplanar and grazing incidence scattering geometries. Figure 4 shows reciprocal space maps in the three main phases of the $BaTiO_3$ substrate and $La_{0.7}Ca_{0.3}MnO_3$ thin film. Using the point detector in GIXRD geometry, reciprocal space maps in the region of the BTO (0-12) reflection were taken at low temperatures (Fig. 5). To avoid long exposure times required by the point detector at ESRF, a CCD camera was used to obtain reciprocal space maps in the three ferroelectric phases of the substrate. According to the observed diffraction patterns, $La_{0.7}Ca_{0.3}MnO_3$ films remain epitaxial at all temperatures (see also Fig. 5) with in-plane lattice parameters a and b larger than the pseudocubic bulk value (a_P = 3.86 Å), while c remains smaller, at all temperatures (see Fig.6), with the exception of 250 K (we do not have an explanation for the anomalous observation at T = 250 K).

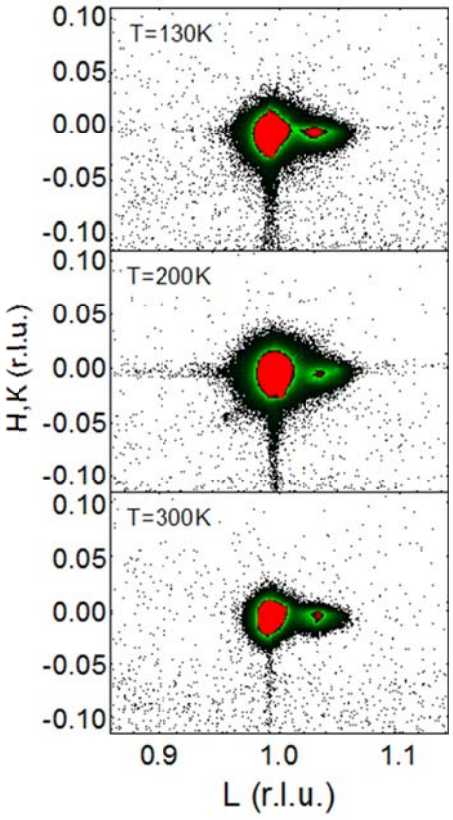

Fig.4. Coplanar XRD reciprocal space maps of the symmetric (100) reflection of a $La_{0.7}Ca_{0.3}MnO_3$//$BaTiO_3$ sample. Peak on the left is the $BaTiO_3$, saturated (but not masked) in this measurement. The peak on the right side corresponds to $La_{0.7}Ca_{0.3}MnO_3$.

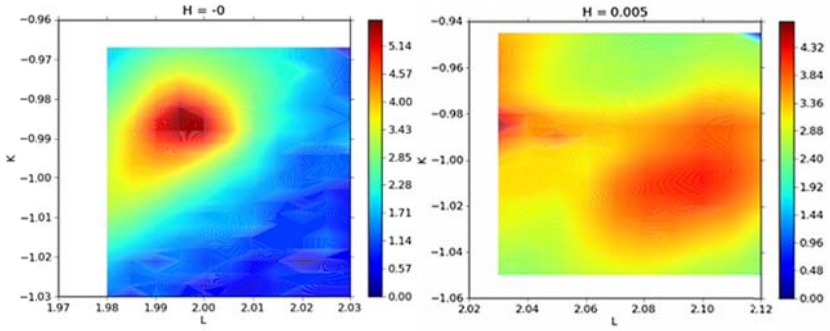

Fig.5. GIXRD reciprocal space map around the asymmetric (0-12) reflection for $BaTiO_3$ (left) and $La_{0.7}Ca_{0.3}MnO_3$ (right) at 120K.

Figure 6 shows the calculated parameters for the thin film. Note that high-resolution neutron powder diffraction of BTO reveals that there is hardly any change in its lattice parameters below T = 130 K (the maximum change in the fitted lattice parameter throughout the rhombohedral phase corresponds to 5×10^{-4} Å at 150 K, relative to the experimental value at 15 K) [Billinge1993] and no structural transition occurs at those temperatures in bulk $La_{0.7}Ca_{0.3}MnO_3$. On this basis, no additional strain sources are expected, other than thermal contraction of the lattices. Open symbols in Fig. 6 correspond to a second campaign of GIXD measurements near $(0\bar{1}1)$ on a separate, but magnetically equivalent, $La_{0.7}Ca_{0.3}MnO_3$//$BaTiO_3$ sample.

Strains calculated with reference to the room temperature $La_{0.7}Ca_{0.3}MnO_3$ pseudocubic parameter, $\varepsilon_{\alpha\alpha} = (\alpha - a_P)/a_P$ with $\alpha = 1, 2, 3 \equiv x, y, z$, were calculated for both $BaTiO_3$ substrate and $La_{0.7}Ca_{0.3}MnO_3$ thin film and are shown in Fig. 7. Structural coherence lengths (Fig. 8) estimated from the widths of the GIXD $(1\bar{1}2)$ diffraction peaks are approximately constant in temperature and range from 200–250 Å in plane and 70–90 Å out of plane (smaller than the film thickness of 120 Å) for $La_{0.7}Ca_{0.3}MnO_3$ layer. This agrees with the results obtained in coplanar room temperature XRD.

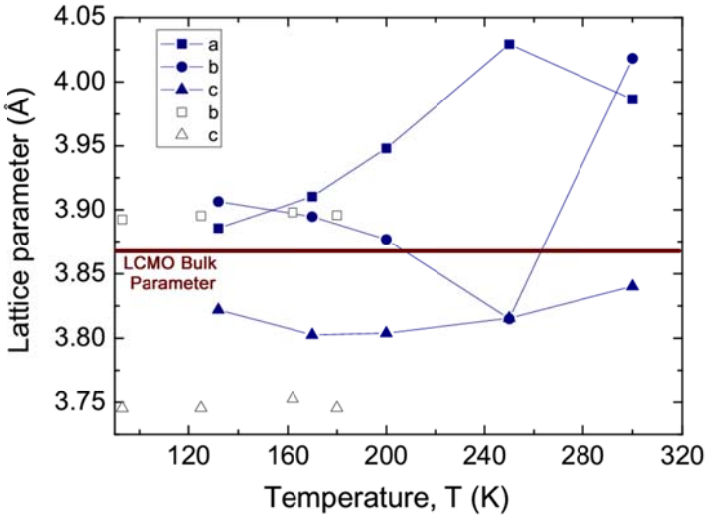

Fig.6. $La_{0.7}Ca_{0.3}MnO_3$//$BaTiO_3$ lattice parameters against temperature. Data extracted from CCD reciprocal space maps at two different campaigns at the ESRF SpLine beamline. Closed and open symbols refer to two

different samples. Closed symbols were obtained from measurements near $BaTiO_3$ (1-12) and open symbols near $BaTiO_3$ (0-11).

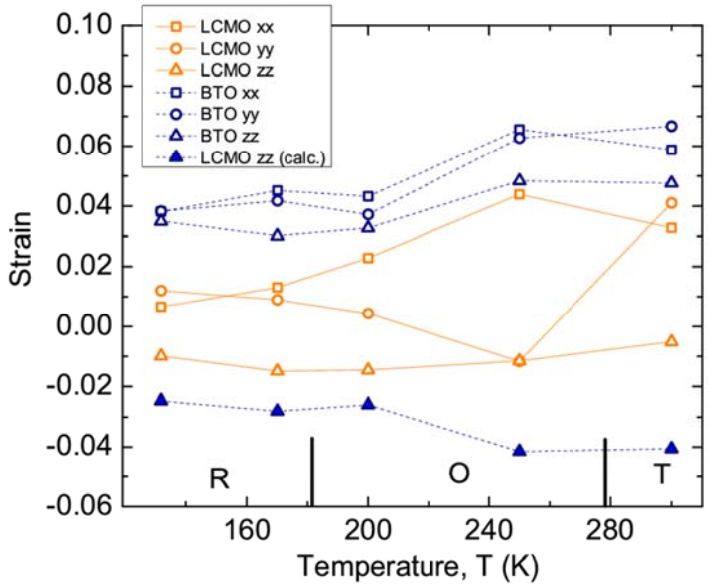

Fig.7. Temperature dependence of strains relative to pseudocubic bulk parameter of $La_{0.7}Ca_{0.3}MnO_3$, for both $BaTiO_3$ and $La_{0.7}Ca_{0.3}MnO_3$ peaks (open symbols) and $La_{0.7}Ca_{0.3}MnO_3$ ε_{zz} in biaxial approximation from $BaTiO_3$ strain values: $\varepsilon_{zz} = -(c_{12}/c_{11})(\varepsilon_{xx} + \varepsilon_{yy})$, suitable in first approximation to describe the strain field in the $La_{0.7}Ca_{0.3}MnO_3$ layers closer to $BaTiO_3$ (full symbols). Vertical bars indicate the temperatures of the $BaTiO_3$ structural phase transitions.

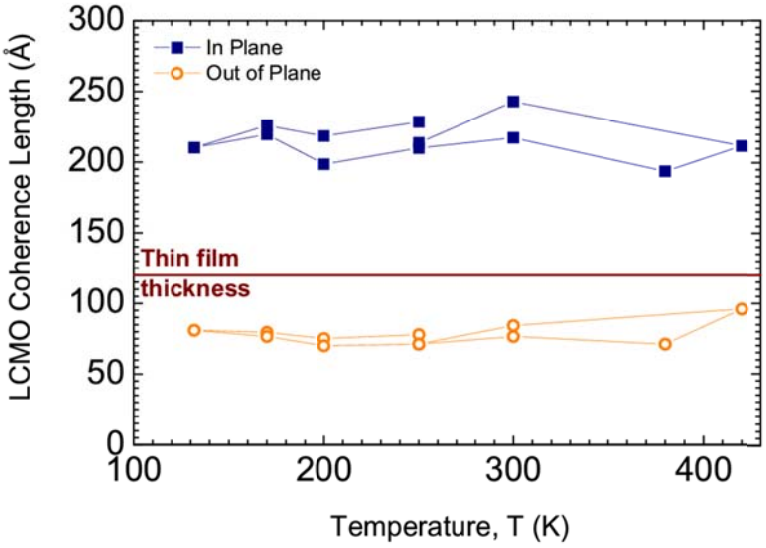

Fig.8. Structural coherence lengths versus temperature of the thin film in plane (blue squares) and out of plane (orange circles). Note that the structural coherence length is smaller than the thickness of the layer at all temperatures.

TOPOGRAPHY

We discussed in Chapter 2 the relevance of domain formation in the structure of the $BaTiO_3$ substrate surfaces. XRD techniques have also shown the complexity of the structure of thin films of $La_{0.7}Ca_{0.3}MnO_3$ when grown on $BaTiO_3$ and compared with $La_{0.7}Ca_{0.3}MnO_3$//$SrTiO_3$ samples. Here we discuss the topography of $La_{0.7}Ca_{0.3}MnO_3$//$BaTiO_3$ samples measured by atomic force microscopy (AFM).

There is a noticeable difference in surface morphology between $La_{0.7}Ca_{0.3}MnO_3$ grown on $SrTiO_3$ and $BaTiO_3$. Over large length scales, the $La_{0.7}Ca_{0.3}MnO_3$//$BaTiO_3$ surface shows a corrugation in the micron range that yields a mean roughness of 12 nm [Fig. 9(a)], whereas the $La_{0.7}Ca_{0.3}MnO_3$//$SrTiO_3$ shows a flat surface with a mean roughness of 1 nm [Fig. 9(b)]. This difference is better observed in the profiles of Fig. 9(c), and has its origin in the crystal symmetry of the substrates. Figures 9(d) and 9(e), corresponding to the microscale morphology, still show considerable differences, yielding rms values of 4 nm vs. 0.6 nm for the $La_{0.7}Ca_{0.3}MnO_3$//$BaTiO_3$ and $La_{0.7}Ca_{0.3}MnO_3$//$SrTiO_3$, respectively. Nevertheless, on the nanometer scale [Figs. 8(g) and 8(h)], both substrates provide flat support for the epitaxial growth of $La_{0.7}Ca_{0.3}MnO_3$, with similar surface roughness of 0.5 nm.

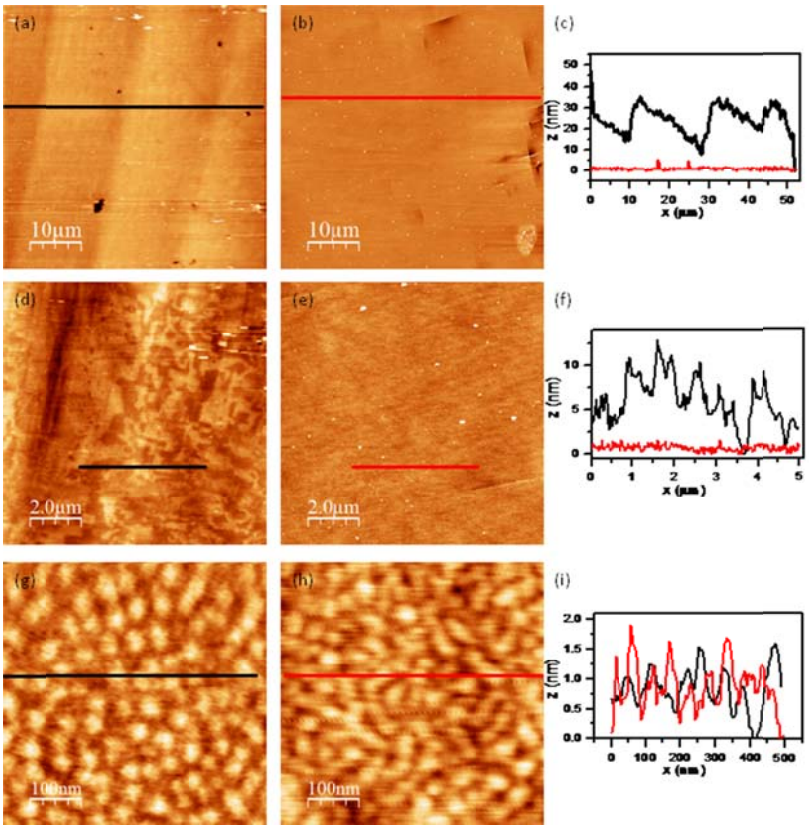

Fig.9. Room temperature AFM topographic images of a), d), and g) $La_{0.7}Ca_{0.3}MnO_3$//$BaTiO_3$ and b), e) and h) $La_{0.7}Ca_{0.3}MnO_3$//$SrTiO_3$ samples on different length scales. c), f) and i) profiles taken along the lines indicated in the topographic images.

A subsequent topography study of the domain thermal evolution allowed us to establish some general features of unpoled $BaTiO_3$ substrates in the three phases of interest. Topographic images of the same representative area are shown in Fig. 10 for selected temperatures at 300 K [Fig. 10(a)], 270 K [Fig. 10(b)], 180 K [Fig. 10(c)], and 100 K [Fig. 10(d)]. To better highlight possible changes in morphology with temperature, line profiles are compared in pairs in Figs. 10(e)–2(g). In order to avoid image processing artifacts, only global plane subtraction was applied prior to profile measurement. The corresponding morphology for the T, O, and

rhombohedral phases is shown in Figs. 10(a)–10(c). The surface morphology at 100 K is also presented in Fig. 10(d).

In the scanned area, the $BaTiO_3$ surface exhibits, in all ferroelectric phases, a primary corrugation with a characteristic length around 15 μm that yields a mean roughness of 7.5 nm on 50 × 50 μm^2 areas. This corrugation, explained by the ferroelectric equilibrium conditions prevailing in the tetragonal phase, dominates the landscape, but some rippling of the slopes is also apparent. From 300 to 180 K, only minor changes are observed in the surface morphology corresponding to this dominant corrugation, which translate into very similar profiles for 300 and 270 K [Fig. 10(e)]. This behaviour has also been reported in $BaTiO_3$ (111) samples studied by transmission electron microscopy [Wang2011].

At 180 K, differences are hardly noticeable in the AFM image, but line profiles show subtle deviations from those measured at higher temperatures [Fig. 10(f)]. These differences are marked with black arrows and show the disruption of the primary slope and the formation of a mound-like structure or secondary corrugation, with a characteristic length close to 7.5 μm, about half the value of the primary corrugation. In view of the variability exhibited by the $BaTiO_3$ substrates, the precise values of the corrugation characteristic lengths should not be understood as general properties of these ferroelectric substrates. The T-O structural phase transition at 295K seems to trigger the observed changes in surface morphology, but it is below the O-R transition where the secondary corrugation consolidates. No further structural transition is expected on cooling below 183 K. Surprisingly, we observed significant changes in the topographic profiles at 100 K. These are marked in Fig. 10(g) and include height differences of up to 4 nm (over 2 μm) and the final formation of the secondary corrugation.

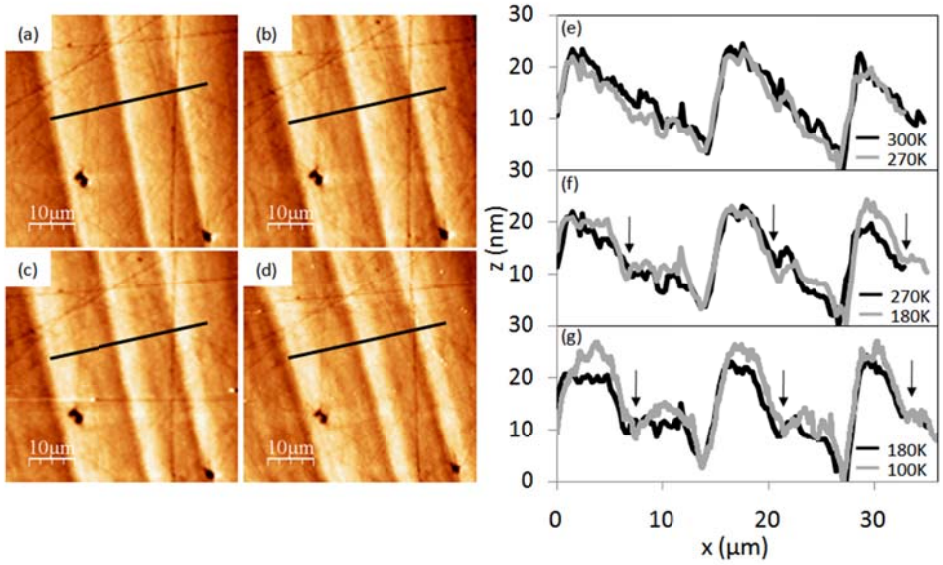

Fig.10. Topography of a $BaTiO_3$ substrate above and below the tetragonal-orthorhombic phase transition at (a) 300 K and (b) 270 K, in the rhombohedral phase at (c) 180 K and at (d) 100 K. Panels (e)–(g) show a comparison of the line profiles of (a)–(d) in pairs.

CONCLUSIONS

In summary, $La_{0.7}Ca_{0.3}MnO_3$ thin films grown on $BaTiO_3$ are epitaxial in all three ferroelectric phases of the substrate, with tensile strain in plane and compressive strain out of plane; typical strains are of 1-2%.

Coherence lengths are rather small when compared with control samples grown on $SrTiO_3$, with typical grain size of around 200 x 200 x (70-90) $Å^3$. $La_{0.7}Ca_{0.3}MnO_3$ thin films are partially relaxed, with relaxation coefficients between R = 0.2-0.7. $La_{0.7}Ca_{0.}3MnO_3$//$BaTiO_3$ topography has also been explored by means of atomic force microscopy, allowing us to characterize the corrugated surface of $BaTiO_3$ and compare it with $SrTiO_3$.

These two techniques allow us to establish the following picture: first, there is a highly corrugated interface between $BaTiO_3$ and $La_{0.7}Ca_{0.3}MnO_3$ that contributes to the small coherence lengths observed, second, the lattice mismatch between substrate and thin film bulk parameter, that results in high strains and, third, $La_{0.7}Ca_{0.3}MnO_3$ is magnetoelastically coupled to $BaTiO_3$ since the thin film adapts to the substrate lattice parameter. As we shall see in the next chapters, the implications of these three characteristics in the magnetic and transport properties will be crucial.

REFERENCES

[Alberca2011] Alberca, A., et al. "Exotic magnetic anisotropy map in epitaxial La0.7Ca0.3MnO3 films on BaTiO3." Physical Review B 84.13 (2011): 134402.

[Alberca2012] Alberca, A., et al. "Ferroelectric substrate effects on the magnetism, magnetotransport, and electroresistance of La0.7Ca0.3MnO3 thin films on BaTiO3." Physical Review B 86.14 (2012): 144416.

[Billinge1993] Kwei, G. H., et al. "Structures of the ferroelectric phases of barium titanate." The Journal of Physical Chemistry 97.10 (1993): 2368-2377.

[Loetzsch2010] Loetzsch, R., et al. "The cubic to tetragonal phase transition in SrTiO3 single crystals near its surface under internal and external strains." Applied Physics Letters 96.7 (2010): 071901-071901.

[Pietsch2004] Pietsch, Ullrich, Vaclav Holy, and Tilo Baumbach. "High-resolution X-ray scattering: from thin films to lateral nanostructures". Springer, 2004.

[Wang2011] Wang, Y. L., et al. "Unusual dielectric behavior and domain structure in rhombohedral phase of BaTiO3 single crystals." Journal of Applied Physics 110.1 (2011): 014101-014101.

CHAPTER 5
MAGNETISM IN $La_{0.7}Ca_{0.3}MnO3$//BaTiO3 ULTRA-THIN FILMS

In this chapter, the magnetic characterization of $La_{0.7}Ca_{0.3}MnO_3$//$BaTiO_3$ ultra-thin films is addressed. As we did in the previous chapter, we compare $La_{0.7}Ca_{0.3}MnO_3$ samples grown under the same conditions on $BaTiO_3$ and $SrTiO_3$ substrates.

$La_{0.7}Ca_{0.3}MnO_3$//$BaTiO_3$ show anomalous magnetic hysteresis between 40 K and 150 K. This hysteretic behaviour, named Matteucci magnetic loops, display extremely unusual features: after switching at coercivity, the magnetization overshoots the eventual high-field value. Also, the temperature dependence of the magnetization exhibits large irreversibilities between the zero field cooled (ZFC) and field cooled runs and blocking temperature pointing towards a magnetic granular behavior. These observations are compatible with the picture of a non-uniform strain field in $La_{0.7}Ca_{0.3}MnO_3$ on $BaTiO_3$, caused by the corrugation of the ferroelectric domains in the rhombohedral phase of $BaTiO_3$.

Magnetic characterization can be summarized in two main results: 1) Matteucci-like magnetic loops in the range 40K-150K, and, 2) magnetic granularity. We propose a basic model of two magnetic moment populations with different magnetoelastic anisotropy. The relative weight of both populations is estimated from the comparison with twin reference samples of $La_{0.7}Ca_{0.3}MnO_3$ films on non-ferroelectric $SrTiO_3$. Then, the observed magnetization overshoot may result from differences in the magnetostriction balance as the applied magnetic field increases. Finally, we consider the effect thin film thickness.

We explain our main findings in terms of the intrinsic phase separation tendency of $La_{0.7}Ca_{0.3}MnO_3$ enhanced by elastic effects resulting from an inhomogeneous strain map present in the ferroelectric substrate.

MAGNETISM IN La0.7Ca0.3MnO3//BaTiO3 THIN FILMS

MAGNETIC GRANULARITY

Obvious differences between $La_{0.7}Ca_{0.3}MnO_3$//$SrTiO_3$ and $La_{0.7}Ca_{0.3}MnO_3$//$BaTiO_3$ (120 Å, unpoled substrate) are apparent the ZFC and FC measured at 100 Oe and appearing in Figure 1 (a) and (b). The Curie temperature, T_c, is depressed from the 270 K bulk value to about 180 K in $La_{0.7}Ca_{0.3}MnO_3$//$BaTiO_3$ and, to 150 K for $SrTiO_3$ samples. For $La_{0.7}Ca_{0.3}MnO_3$//$BaTiO_3$, the temperature dependence of M exhibits strongly diverging zero field cooled (ZFC) and field cooled (FC) curves with a broad maximum (Blocking temperature, T_B) centred at 120 K [Fig. 1(b)] while in the case of $La_{0.7}Ca_{0.3}MnO_3$//$SrTiO_3$ system the closure temperature (T_{cl}, temperature in which ZF and ZFC overlap) is around 50K.

Notably, some $La_{0.7}Ca_{0.3}MnO_3$//$BaTiO_3$ samples exhibit important negative magnetization at low temperature after cooling without applied field, see Fig.1(c). Negative magnetization at low temperature is characteristic of frozen antiferromagnetic correlations in a frustrated system [Mihaly2004, Bartolomé2005, Mellergard2005]. It is important to remark here that all ZFC-FC in Figure 1 were measured in exactly the same conditions in a SQUID-based magnetometer equipped with a 5 Tesla coil, which is known to have a remanent field around 1 Oe, therefore, these results cannot be considered as an instrumental artefact.

As expected, Curie temperature (T_c, see Fig. 1) increases with sample thickness: T_c (120 Å) = 180 K, T_c (150 Å) = 220 K and T_c (240 Å) = 230 K, in the case of the sample shown in Fig. 8. As previously reported on $La_{0.7}Sr_{0.3}MnO_3$//$BaTiO_3$ (Refs. [Eerenstein2007] and [Lee2000]), hysteretic jumps of the magnetization are detected around the $BaTiO_3$ structural phase transitions that become smoother in thicker films (Fig. 1, insets).

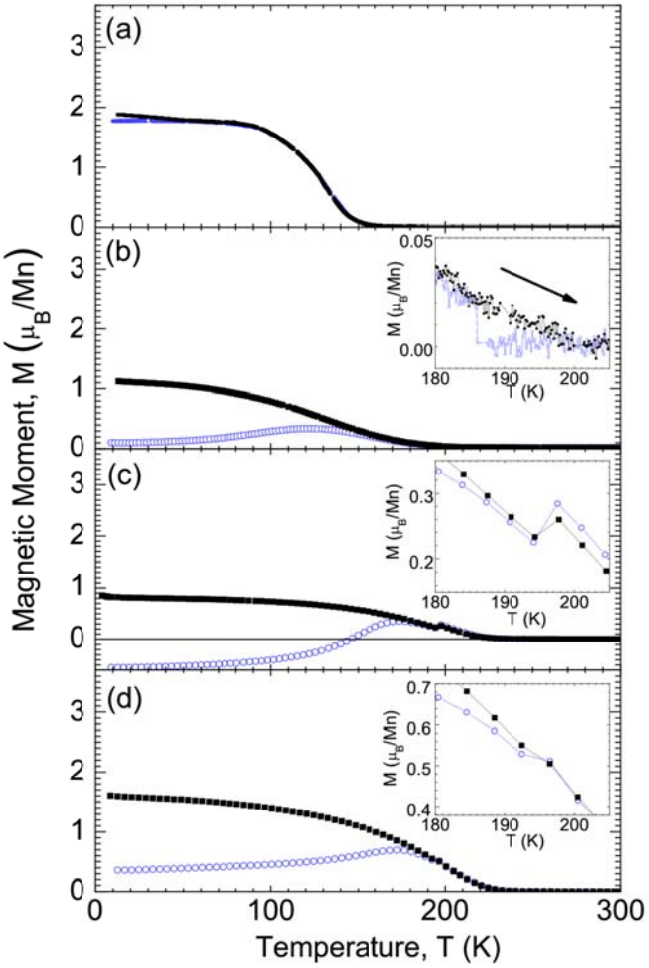

Fig.1. Field cooled (black squares) and zero field cooled (blue circles) temperature-dependent magnetic moments for 120 Å $La_{0.7}Ca_{0.3}MnO_3$ on (a) $SrTiO_3$, (b) poled $BaTiO_3$, (c) unpoled $BaTiO_3$, and (d) 150 Å $La_{0.7}Ca_{0.3}MnO_3$ on unpoled $BaTiO_3$ measured in 100 Oe. Insets highlight the magnetic moments jumps at the R-O $BaTiO_3$ transition.

MAGNETIC HYSTERESIS LOOPS

Figures 2 and 3 shows magnetic hysteresis loops measured at 10 K for $La_{0.7}Ca_{0.3}MnO_3$//$BaTiO_3$ (100 Å) and $La_{0.7}Ca_{0.3}MnO_3$//$SrTiO_3$. The saturation magnetic moment is quite reduced, from the limiting theoretical 3.7 μ_B/Mn, to 2.3 μ_B/Mn in $La_{0.7}Ca_{0.3}MnO_3$//$SrTiO_3$, and to 1.6 μ_B/Mn in $La_{0.7}Ca_{0.3}MnO_3$//$BaTiO_3$. The other

striking difference comes from the coercive fields which are one order of magnitude larger in $La_{0.7}Ca_{0.3}MnO_3$//$BaTiO_3$ than in $La_{0.7}Ca_{0.3}MnO_3$//$SrTiO_3$. Figure 4 shows the coercive fields, H_c, extracted from the magnetic hysteresis loops at different temperatures. H_c rises linearly with decreasing temperature in $La_{0.7}Ca_{0.3}MnO_3$//$BaTiO_3$. This linear dependence of coercive fields with temperature and the high blocking and closure temperatures are an indication of a magnetic granularity [Colino2005]. Note that we do not refer to a granular structure in the sense of a polycrystalline film (as we showed in Chapter 4, $La_{0.7}Ca_{0.3}MnO_3$//$BaTiO_3$ thin films are epitaxial) but to a system exhibiting an inhomogeneous magnetic behaviour.

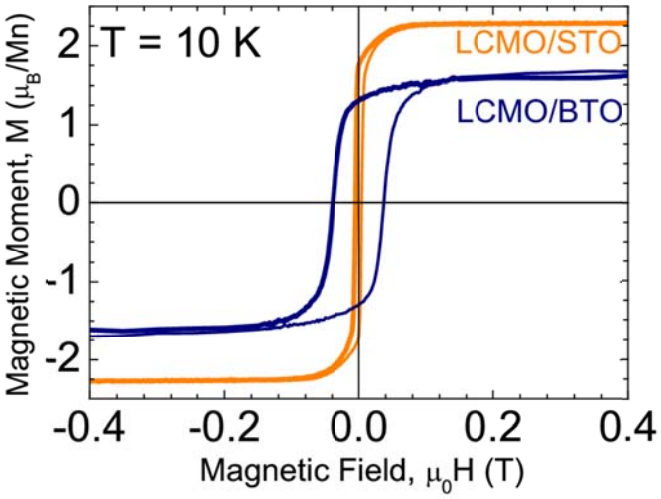

Fig.2. Hysteresis cycles for $La_{0.7}Ca_{0.3}MnO_3$//$BaTiO_3$ (blue) and $La_{0.7}Ca_{0.3}MnO_3$//$BaTiO_3$ (orange) at 10 K.

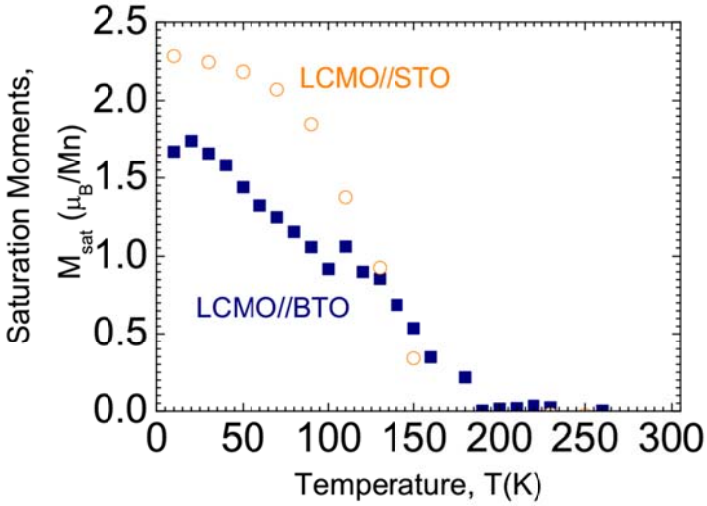

Fig.3. Saturation moments (around 1 T) versus temperature for $La_{0.7}Ca_{0.3}MnO_3$//$BaTiO_3$ (blue) and $La_{0.7}Ca_{0.3}MnO_3$//$BaTiO_3$ (orange) extracted from magnetic loops.

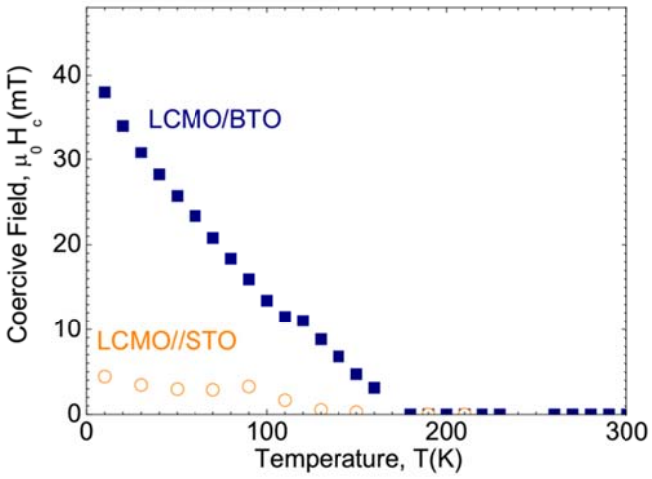

Fig.4. Coercive fields against temperature for $La_{0.7}Ca_{0.3}MnO_3$//$BaTiO_3$ (blue) and $La_{0.7}Ca_{0.3}MnO_3$//$BaTiO_3$ (orange) extracted from magnetic loops.

A remarkably anomalous behaviour of the hysteresis cycles of $La_{0.7}Ca_{0.3}MnO_3$//$BaTiO_3$ was found for 40 K < T < 150 K. An example is shown in Fig. 5 at 100 K, near the ZFC maximum, where the effect is most pronounced. After switching at H_c, the magnetization overshoots the high field value, M_s, and then steadily decreases as the magnetic field increases to the saturation magnetization. This is improperly termed as saturation and it is the high field valued measured approximately at 1 Tesla. When the magnetic field decreases, the magnetization remains at "saturation" until the magnetic field passes coercivity on the opposite side and, again, in negative fields, the same overshoot occurs. This can be interpreted as a fraction of spins that cannot align with the applied field. Since no phase transition occurs in $BaTiO_3$ in this temperature range, the observed behaviour could be related to the corrugation that steadily develops deep within the rhombohedral phase.

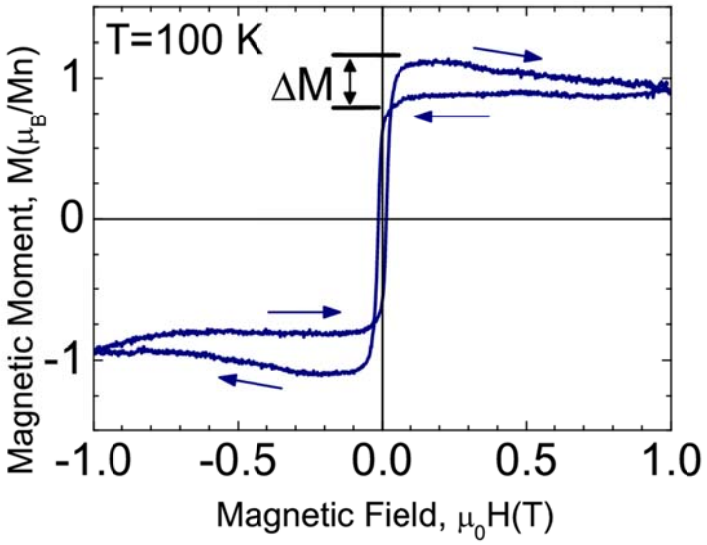

Fig.5. Exotic, Matteucci-like, hysteresis loop at 100 K of $La_{0.7}Ca_{0.3}MnO_3$//$BaTiO_3$ showing excess magnetization, ΔM.

This excess magnetization, ΔM (the maximum difference between hysteresis loop branches, see Fig. 5) is same for negative and positive values of the magnetic field and at 100 K corresponds to almost 21% of the maximum moment reached. ΔM and the normalized difference in saturation moments between $La_{0.7}Ca_{0.3}MnO_3$//$BaTiO_3$ and $La_{0.7}Ca_{0.3}MnO_3$//$SrTiO_3$ remarkably show the same temperature dependence in the 50–120 K range, see Fig. 6. The excess magnetization ΔM relaxes, decaying linearly with a time constant of 10^{-3} μB/Mn/min as determined by SQUID magnetometry at 100 K and −0.5 T, following sample saturation at 5 T. Similar hysteresis loops (named Matteucci or inverse Wiedemann cycles) have been observed in metal bars under torsion stress fields that induce helical arrangements of magnetization [Hernando1975].

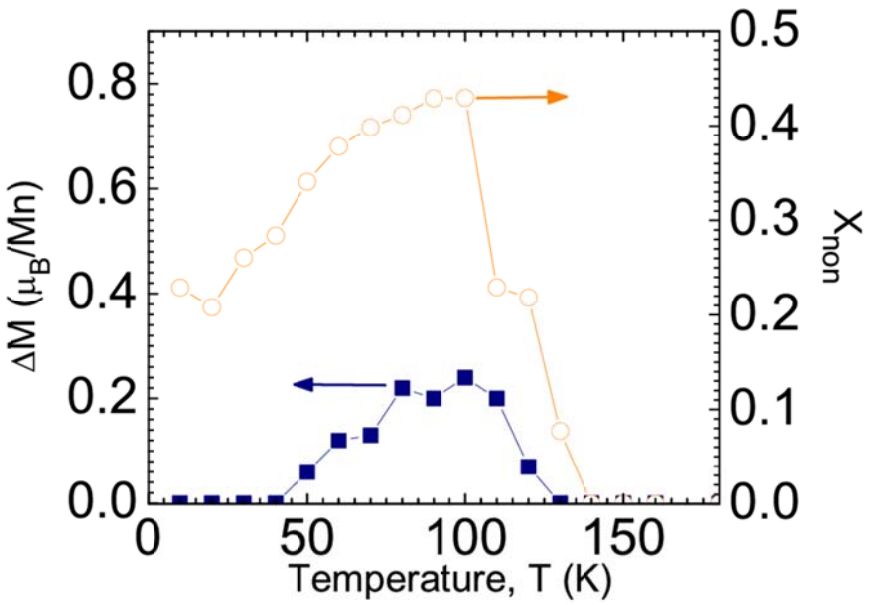

Fig.6. Temperature dependence of ΔM, the excess magnetization observed in Matteucci-like hysteresis cycles (open circles) and x_{non}, the fraction of nonaligned magnetic moments, estimated as [1 − M_s ($La_{0.7}Ca_{0.3}MnO_3$//$BaTiO_3$) / M_s($La_{0.7}Ca_{0.3}MnO_3$//$BaTiO_3$)] (full squares).

Figure 7 shows magnetization hysteresis loops up to 2.5 T field, applied both in plane, along [100], and out of plane, along [001] on a 120Å $La_{0.7}Ca_{0.3}MnO_3$//$BaTiO_3$ sample. The Matteucci effect persists in both orientations in low field, even though magnetic fields as large as 5 T were applied. Also, the out-of-plane loop slightly crosses the in-plane loop above 1 T, hinting at some missing moment in the parallel orientation. Note that the noisy trace of the cycles in the inset of Fig. 5 cannot be attributed to instrumental noise but rather to a non-equilibrium condition of the magnetic moments in the sample, as also indicated by the relaxation of ΔM. In fact, this noise at higher fields was always observed in all $La_{0.7}Ca_{0.3}MnO_3$//$BaTiO_3$ samples, but considerably reduced in $La_{0.7}Ca_{0.3}MnO_3$//$SrTiO_3$ samples.

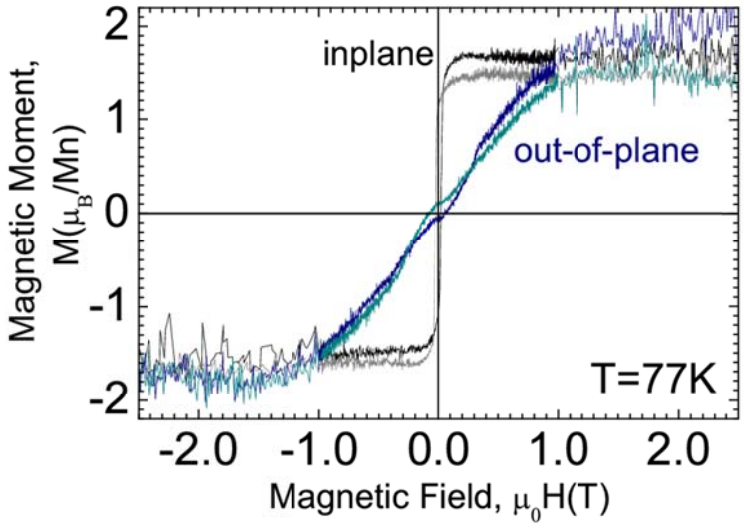

Fig.7. Hysteresis cycles with magnetic field in plane (black) and out of plane (blue) of $La_{0.7}Ca_{0.3}MnO_3$//$BaTiO_3$ at 77K. Increasing field in black and dark blue; decreasing field in gray and light blue: note the Matteucci effect at low field in both orientations.

The complex magnetic properties in $La_{0.7}Ca_{0.3}MnO_3$//BaTiO3 are the result of interfacial effects, which are more pronounced in thinner films. In fact, for layers as thick as 240 Å, no Matteucci hysteresis loops were observed, Fig. 8. Magnetism of thicker $La_{0.7}Ca_{0.3}MnO_3$//$BaTiO_3$ resembles that of $La_{0.7}Ca_{0.3}MnO_3$//$SrTiO_3$: no depressed saturation moments, no Matteucci hysteresis loops and no magnetic granularity.

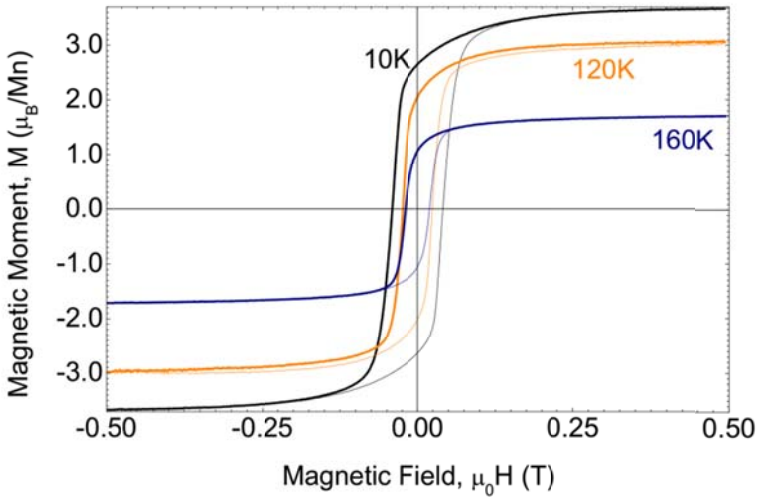

Fig.8. Magnetization hysteresis cycles at 160 K (blue), 120 K (orange), and at 10 K (black) of a 240 Å thick $La_{0.7}Ca_{0.3}MnO_3$//$BaTiO_3$ (T_c = 230K).

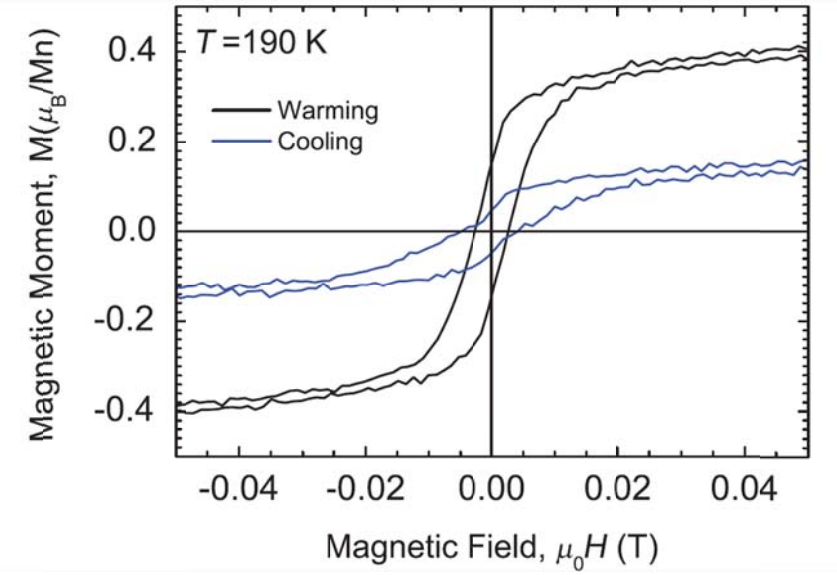

Fig.9. Magnetization hysteresis loops at the same 190 K after warming from 10 K, in the rhombohedral phase (black lines) and cooling from 300 K, in the orthorhombic phase (blue lines), at the hysteretic R-O transition of $BaTiO_3$ for 120 Å $La_{0.7}Ca_{0.3}MnO_3$//$BaTiO_3$.

Figure 9 compares for a 120 Å $La_{0.7}Ca_{0.3}MnO_3$//$BaTiO_3$ the hysteresis loops recorded at 190 K after either cooling from 300 K in the $BaTiO_3$ orthorhombic phase or warming from 10 K in the rhombohedral. Even though the magnetic moment is higher in the rhombohedral phase, the coercive fields are larger in the orthorhombic phase, indicating the strong influence of the surface morphology on the magnetic properties of the $La_{0.7}Ca_{0.3}MnO_3$ film. The observed magnetic moment difference between the two phases at 190 K is compatible with differences stemming either from substrate-induced strain (via magnetoelastic and magnetostrictive coupling) or from electric polarization [via giant converse magnetoelectric coupling with coefficients of the order of magnitude determined for $La_{0.7}Sr_{0.3}MnO_3$ on $BaTiO_3$, [Eerenstein2007, Thiele2007] or a combination of both.

MAGNETOELASTIC FREE ENERGY DENSITY

$La_{0.7}Ca_{0.3}MnO_3$//$BaTiO_3$ systems are epitaxial thin films with a finite in-plane and out-of-plane structural coherence [Alberca2011]. However the observed magnetic response is akin to a granular system (i.e. the coercive field of the $La_{0.7}Ca_{0.3}MnO_3$//$BaTiO_3$ rises linearly with decreasing temperature up to a large value of approximately 500 Oe, typical of strongly hindered, interlinked granular systems), therefore, we refer to it as a magnetically granular system. The most outstanding feature: the anomalous hysteresis cycles in the 40–120 K temperature range can only be understood in terms of a fraction of spins that rotate out of plane when the applied field increases. The large coercive field points to a very distinctive anisotropy map when compared to $La_{0.7}Ca_{0.3}MnO_3$//$SrTiO_3$. From the AFM topography a noticeable roughness is apparent, due to the inhomogeneous ferroelectric domain map of $BaTiO_3$.

An analysis involving magnetoelastic energy can be considered here along the lines of other studies for the case of magnetite on $BaTiO_3$ [Vaz2009, Sterbinsky2010]. The model assumes that there exists some magnetic moment misalignment induced by the presence of significant stress fields that arise due to the inhomogeneous ferroelectric domain map of the substrate. To account for magnetoelastic anisotropy effects, the model introduces two effective magnetization populations within the $La_{0.7}Ca_{0.3}MnO_3$ thin film: aligned and nonaligned with the in-plane applied magnetic field, with relative abundance fractions x_{align} and x_{non},

respectively. Relying on the comparison with the more uniformly stressed $La_{0.7}Ca_{0.3}MnO_3//SrTiO_3$ sample we estimate $x_{non} = [1 - M_s (La_{0.7}Ca_{0.3}MnO_3//BaTiO_3) / M_s(La_{0.7}Ca_{0.3}MnO_3//SrTiO_3)]$ from the corresponding high field magnetizations at each temperature (see Fig. 6). The relevance and implications of this estimation will be discussed in more detail in Chapter 7, nevertheless, some remarks are in order here. First, we have seen that in thicker layers (t > 200 Å, Fig. 8) the saturation magnetization at low temperatures is almost the theoretically expected value 3.7 μ_B/Mn. It is obvious then that the depressed magnetization observed in very thin layers is an interface effect only noticeable when the total magnetic volume is reduced. Second, the presence of a dead layer, which is known to exist in $La_{0.7}Ca_{0.3}MnO_3//SrTiO_3$ samples, may be present in our $BaTiO_3$ layers too, especially considering the topography. Therefore, as indicated above, we consider the non-aligned population as the difference with $La_{0.7}Ca_{0.3}MnO_3//SrTiO_3$ saturation moments.

The magnetoelastic anisotropy free energy, F, is given by the sum of the contributions from both magnetic moment populations:

$$F = F_{M,align}\, x_{align} + F_{M,non}\, x_{non} \qquad [1]$$

Where F, expressed in function of the spherical coordinates, is given by:

$$F_M = \left(K_t \cos 2\varphi + K_o \sin 2\varphi\right)\sin^2\theta + K_p \cos^2\theta \qquad [2]$$

In this notation, the coefficients K_t, K_o and K_p refer to contributions arising from tangential and orthogonal (in plane) and perpendicular (out of plane) **M** components, respectively, with respect to **H** and are defined as $K_t = B_1 (\varepsilon_{11} - \varepsilon_{22})/2$, $K_o = B_2\varepsilon_{12}/2$ and $K_p = B_1[1 + c_{11}/(2c_{12})]\varepsilon_{33}$ with $B_1 = 3\lambda_{100} (c_{12} - c_{11})/2$ and $B_2 = -3\lambda_{111}c_{44}$ [O'Donnell1998, Seikh2004]

For a thin film, shape anisotropy would favour $\theta = 90^o$ and an optimal value for φ determined by the ratio K_t/K_o. However, it should be kept in mind that our $La_{0.7}Ca_{0.3}MnO_3//BaTiO_3$ sample exhibits characteristics proper of a kind of inhomogeneous magnetic granular system, and therefore the restriction imposed by the shape anisotropy may be relaxed. ($\varepsilon_{12} \approx 3.5 \times 10^{-3}$), K_o is small and so F is almost insensitive to the in-plane angle, φ. Thus, we set $\varphi = 0$ and are left with the K_t and K_p terms to analyse the contributions of aligned and nonaligned populations to system stabilization. We will see in Chapter 7 how this approximation is, in fact, a good approximation.

Furthermore, we assume that nonaligned spins lay close to the interface with $BaTiO_3$, although some contribution from in-plane segregation might also be conceivable. This is a plausible assumption given the limited out-of-plane structural coherence of our film (70 Å). We then characterize the $La_{0.7}Ca_{0.3}MnO_3//BaTiO_3$ interface with a biaxial in-plane strain state with values for ε_{11} and ε_{22} taken directly from $BaTiO_3$ GIXD measurements and ε_{33} derived from the biaxial strain field as $\varepsilon_{33} = -(c_{12}/c_{11})(\varepsilon_{11} + \varepsilon_{22})$, a reasonable assumption for epitaxial growth. The aligned population is characterized by $\theta = 90^\circ$ and its strain field determined from $La_{0.7}Ca_{0.3}MnO_3$ GIXD measurements. The resulting in a non-uniform strain field in our thin $La_{0.7}Ca_{0.3}MnO_3$ film indicates higher relaxation away from the $La_{0.7}Ca_{0.3}MnO_3//BaTiO_3$ interface (compare full triangles and open triangles in Fig. 7 in Chapter 4). Evaluating [1] with the above-mentioned assumptions and the literature value for the magnetostriction of $\lambda_{100} = +7 \times 10^{-5}$ [O'Donnell1998] for both aligned and nonaligned populations, we obtain only a marginal stabilizing effect from the aligned population contribution to F, irrespective of the fraction of nonaligned moments: with our strain fields and positive magnetostriction, an out-of-plane nonaligned population does not contribute to system stabilization (since $B_1 > 0$)
Within the limitations of our model, such stabilization can only be introduced by a change of sign in B_1 for the nonaligned population. This sign reversal may result from a negative value of the saturation magnetostriction λ or, away from cubic symmetry, from a change in the orientation of the $La_{0.7}Ca_{0.3}MnO_3$ cells (a, b, c) closer to

the $BaTiO_3$ interface with respect to the (x, y, z) laboratory axes or by a combination of both effects. Since our experimental input comes from macroscopic magnetic and averaged structural magnitudes, we cannot identify on microscopic grounds the mechanism operating in $La_{0.7}Ca_{0.3}MnO_3$//$BaTiO_3$. However, if our model is evaluated with $B_1 < 0$ for the nonaligned population, for example by taking λ_{100} (nonaligned) = $-\lambda_{100}$ (aligned), the perpendicular (K_p) stabilizing effect of a very small fraction of nonaligned moments (1%) results in $F < 0$ with wide minima around $\theta = 0°$, which becomes deeper with increasing x_{non}. Thus, fractions of nonaligned moments close to $x_{non} = 0.43$, the value registered at 100 K at the peak of the anomalous effects, would contribute to the system stabilization. Negative values of the magnetostriction through Villari reversal are not uncommon in systems showing Matteucci and inverse Wiedemann effects like metallic glasses under torsion stress along the applied field axis [Hernando1975]. In manganites, a sign reversal in the magnetic anisotropy with (110) easy axis was reported by Ziese *et al.* [Ziese2002]

By analogy with the Matteucci systems and bearing in mind the stabilizing effect of the K_p term for such a population of nonaligned moments at saturation (high fields), we suggest that noncollinear arrangements of magnetic moments occur in our thin $La_{0.7}Ca_{0.3}MnO_3$//$BaTiO_3$ films that are responsible for the anomalous magnetization hysteresis cycles. Furthermore, since corrugation imposed by ferroelectric domains is expected in the rhombohedral phase of $BaTiO_3$, noncollinear (for instance helical, in view of the Matteucci-like magnetic hysteresis phenomenology) arrangements can be expected to be located at the peaks and valleys generated at the $BaTiO_3$ interface by the corrugation where two different ferroelectric domains meet. These highly frustrated regions would be responsible for the time-dependent behavior observed in the magnetic response. Note that the particular distribution of ferroelectric domains is unique for each sample and varies with its thermal history. We have observed the same effect reported here in a variety of samples (as prepared, poled, and annealed), with small sample-dependent details but with the same basic phenomenology.

The existence of regions dominated by K_t and K_p would explain the limited structural coherence of the epitaxy and the observed magnetic granular behavior of $La_{0.7}Ca_{0.3}MnO_3$//$BaTiO_3$. Excess magnetization, ΔM, as shown by $La_{0.7}Ca_{0.3}MnO_3$//$BaTiO_3$ in the temperature range $40\ K < T < 120\ K$ would result from the in-plane alignment of a majority of magnetic moments immediately after the application of the coercive field. As the applied field increases, the growth of the aligned domains is hindered by the strong pinning to $BaTiO_3$ ferroelectric domains, triggering the switch to out-of-plane orientations of a substantial fraction of the moments and thus increasing the number of moments involved in magnetic domain walls exhibiting helical arrangements.

The high-field balance of this competition of magnetostriction effects would be established, as described by our model, with a substantial fraction of the moments lying out of plane, stabilizing the system, and giving rise to a depressed in-plane magnetization. We address the question of whether the observed phenomenology matches what is expected for the phase segregation scenario, given the strong tendency of $La_{0.7}Ca_{0.3}MnO_3$ to it. Phase segregation in the interface of $La_{0.7}Ca_{0.3}MnO_3$ grown on different substrates is apparent around T_C (T_{MI}) and evolves steadily to a predominantly single phase system as the temperature is lowered. However, the anomalous behaviour in the $La_{0.7}Ca_{0.3}MnO_3$//$BaTiO_3$ magnetization cycles is maximum around 100 K, well below T_C and far apart from the region where conventional phase segregation is maximal. Therefore, conventional phase segregation as that observed in many $La_{0.7}Ca_{0.3}MnO_3$ systems (see for instance Ref. [Paranjape2003] on phase segregation of $La_{0.7}Ca_{0.3}MnO_3$ on $SrTiO_3$ and $NdGaO_3$) cannot be considered at the root of the observed behaviour in $La_{0.7}Ca_{0.3}MnO_3$//$BaTiO_3$, but only in a very broad sense of the term. The magnetic properties of $La_{0.7}Ca_{0.3}MnO_3$//$BaTiO_3$ arise from an inhomogeneous structural scenario within the epitaxial film resulting in different magnetic interactions and magnetic orderings. In this sense, our magnetically granular system can be considered as a kind of phase-segregated system driven by strain

[Millis2000]. This is in contrast to what is observed in $La_{0.7}Ca_{0.3}MnO_3$//$SrTiO_3$, a system for which a canonical phase segregation scenario is ascribed.

CONCLUSIONS

In summary, thin epitaxial films of $La_{0.7}Ca_{0.3}MnO_3$//$BaTiO_3$ systematically exhibit anomalous Matteucci-like hysteresis loops around 120 K, the crossover temperature in ZFC magnetization. As in granular systems, this temperature signals the set in of a dominant anisotropy: nonuniform strains in $La_{0.7}Ca_{0.3}MnO_3$ generate a significant out-of-plane magnetic anisotropy. The observed phenomenology cannot be explained in terms of conventional phase separation. Helical arrangements of the spins, similar to those exhibited by Matteucci systems may be responsible for the anomalous magnetic loops. Their precise location and origin are hard to determine solely from macroscopic magnetic measurements, and so, at this point were unanswered.

REFERENCES

[Alberca2011] Alberca, A., et al. "Exotic magnetic anisotropy map in epitaxial La0.7Ca0.3MnO3 films on BaTiO3." Physical Review B 84.13 (2011): 134402.

[Alberca2012] Alberca, A., et al. "Ferroelectric substrate effects on the magnetism, magnetotransport, and electroresistance of La0.7Ca0.3MnO3 thin films on BaTiO3." Physical Review B 86.14 (2012): 144416.

[Bartolomé2005] Bartolome, F., et al. "Element-specific magnetometry on negatively magnetized NdMnO 3+ δ." Journal of applied physics 97.10 (2005): 10A503-10A503.

[Colino2005] Colino, J. M., and A. De Andres. "Huge magnetoresistance in ultrathin LaCaMnO films: The role of superparamagnetic clusters and domain walls." Applied Physics Letters 87 (2005): 142509.

[Eerenstein2007] Eerenstein, W., et al. "Giant sharp and persistent converse magnetoelectric effects in multiferroic epitaxial heterostructures." Nature materials 6.5 (2007): 348-351.

[Hernando1975] A. Hernando and J. Barandiarán, J. Phys. D: Appl. Phys. 8, 833 (1975) & J. Phys. D: Appl. Phys. 11 1539, (1978); A. Hernando, J. Mag. Magn. Mat, 12, 96-101 (1979) & A. Hernando and J.M. Barandiarán, Phys Rev. B, 22, 2445, (1980)

[Lee2000] Lee, Mark K., et al. "Strain modification of epitaxial perovskite oxide thin films using structural transitions of ferroelectric BaTiO3 substrate." Applied Physics Letters 77.22 (2000): 3547-3549.

[Mellergard2005] Azad, A. K., et al. "Structural and magnetic properties of LaFe0.5Cr0.5O3 studied by neutron diffraction, electron diffraction and magnetometry." Materials research bulletin 40.10 (2005).

[Mihaly2004] Mihály, László, et al. "Field-frequency mapping of the electron spin resonance in the paramagnetic and antiferromagnetic states of LaMnO3." Physical Review B 69.2 (2004): 024414.

[Millis2000] Biswas, Amlan, et al. "Two-phase behavior in strained thin films of hole-doped manganites." Physical Review B 61.14 (2000): 9665. & Biswas, Amlan, et al. "Strain-driven charge-ordered state in La0.67Ca0.33MnO3." Physical Review B 63.18 (2001): 184424.

[O'Donnell1998] λ100 = λ111 = 7 × 10−5: O'Donnell, J., et al. "Magnetoelastic coupling and magnetic anisotropy in La0.67Ca0.33MnO3 films." Applied physics letters 72.14 (1998): 1775-1777.

[Paranjape2003] Paranjape, Mandar, et al. "Effect of strain on the electrical conduction in epitaxial films of La0.7Ca0.3MnO3." Physical Review B: Condensed Matter and Materials Physics 67.21 (2003): 214415_1-214415_6.

[Seikh2004] Seikh, Md Motin, et al. "A Brillouin scattering study of La0. 77Ca0. 23MnO3 across the metal–insulator transition." Journal of Physics: Condensed Matter 16.24 (2004): 4381.

[Sterbinsky2010] Sterbinsky, G. E., et al. "Strain-driven spin reorientation in magnetite/barium titanate heterostructures." Applied Physics Letters 96.9 (2010): 092510-092510.

[Thiele2007] Thiele, C., et al. "Influence of strain on the magnetization and magnetoelectric effect in La_ {0.7} A_ {0.3} MnO_ {3}/ PMN-PT (001)(A= Sr, Ca)." Physical Review B 75.5 (2007): 054408.

[Vaz2009] Vaz, Carlos AF, et al. "Magnetic anisotropy modulation of magnetite in FeO/BaTiO (100) epitaxial structures." Applied Physics Letters 94 (2009): 022504.

[Ziese2002] Ziese, M., H. C. Semmelhack, and P. Busch. "Sign reversal of the magnetic anisotropy in La0.7A0.3MnO3(A= Ca, Sr, Ba, □) films." Journal of magnetism and magnetic materials 246.1 (2002): 327-334.

CHAPTER 6

ELECTRONIC TRANSPORT IN $La_{0.7}Ca_{0.3}MnO_3$//$BaTiO_3$ ULTRA-THIN FILMS

In this chapter, we describe transport and magnetostransport results regarding $La_{0.7}Ca_{0.3}MnO_3$//$BaTiO_3$. As before, we compare these results with $La_{0.7}Ca_{0.3}MnO_3$//$SrTiO_3$ control samples. Transport properties are deeply linked to the magnetic ordering in manganites and very sensitive to octahedral distortions due to extrinsic factors such as strain induced by the substrate. For these reason, electronic transport and magnetotransport become a power technique for the characterization of $La_{0.7}Ca_{0.3}MnO_3$//$BaTiO_3$.

In this chapter, we show new hints of out of plane population and/or antiferromagnetic clusters. The coupling between the two magnetic moment populations is expected to severely alter the transport properties of $La_{0.7}Ca_{0.3}MnO_3$ since the metal-insulator (MI) transition, accompanying the paramagnetic to ferromagnetic transition, is percolative in nature. In addition, substrate corrugation is expected to introduce new phenomenology related to enhanced phase separation at the micron length scale. The antiferromagnetic phase may be likely interspersed within the ferromagnetic thin film.

RESISTIVITY

The exotic magnetic behaviour of $La_{0.7}Ca_{0.3}MnO_3$//$BaTiO_3$ shows up in its electronic transport properties. Figure 1 compares the temperature-dependent resistivity of $La_{0.7}Ca_{0.3}MnO_3$//$SrTiO_3$ and two $La_{0.7}Ca_{0.3}MnO_3$//$BaTiO_3$ samples. There are large differences between $La_{0.7}Ca_{0.3}MnO_3$//$SrTiO_3$ and La0.7Ca0.3MnO3//BaTiO3. The $La_{0.7}Ca_{0.3}MnO_3$//$SrTiO_3$ follows the behaviour expected for an optimally doped thin epitaxial manganite layer: there is a metal insulator transition (T_{MI}) near the Curie temperature, which shifts towards higher temperature when increasing the applied field [Dagotto2003]. The resistivity and magnetoresistance are very low at low temperatures with negligible thermal hysteresis.

Thin (120 Å) $La_{0.7}Ca_{0.3}MnO_3$//$BaTiO_3$ films exhibit two hysteretic jumps, coinciding with the two first-order structural transitions of $BaTiO_3$ at T_{R-O} = 188 K (196 K) and T_{O-T} = 283 K (293 K) upon cooling (warming). Remarkably, the resistivity variation at the R-O transition, $\Delta\rho_{R-O}$, exceeds two orders of magnitude and overlaps with the usual M-I transition near T_c. This resistivity jump is sample dependent, although in most cases, it runs from higher resistance on the high-temperature side to lower resistance on the low-temperature side. This is consistent with the typically observed upwards jump of the magnetization as the temperature is lowered. Nevertheless, the sign of $\Delta\rho_{R-O}$ may differ even between simultaneous measurements along the two perpendicular sample edges in the van der Pauw geometry; this is suggestive of the importance of the distribution of ferroelectric domains in $BaTiO_3$ for the conductance pathways which may differ from one sample to another and be further affected by thermal history. When measuring with field perpendicular to the film plane, the observed phenomenology is qualitatively the same as with the field parallel to it.

Indeed, most thin $La_{0.7}Ca_{0.3}MnO_3$//$BaTiO_3$ (120 Å) samples show two metal insulator transitions at around T_{MI} = 160 K and T'_{MI} = 100 K, coinciding with the onset of ferromagnetism at T_C and slightly below the blocking of the magnetic system around 120 K. Here, T_{MI} increases from 160 K in zero magnetic fields to above 260 K for an applied field of 8 T, see Fig. 1(b), behaviour similar to that observed for $La_{0.7}Ca_{0.3}MnO_3$//$SrTiO_3$ and as expected for the conventional MI transition of optimally doped manganites. This is not the case for T'_{MI}. It hardly shifts with field, demonstrating the appearance of a fraction of magnetic moments quite insensitive to the application of an external magnetic field and forming insulating regions.

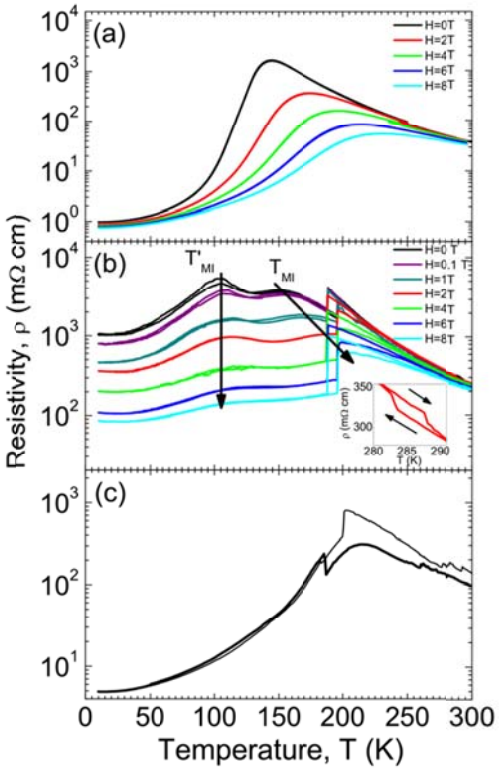

Fig.1. Temperature-dependent resistivity of (a) $La_{0.7}Ca_{0.3}MnO_3$//$SrTiO_3$, (b) $La_{0.7}Ca_{0.3}MnO_3$// $BaTiO_3$ in several in-plane magnetic fields, arrows are guides to the eye, (c) $La_{0.7}Ca_{0.3}MnO_3$// $BaTiO_3$, 240 Å showing one MI transition and strong hysteretic behavior. Inset shows the hysteretic jumps in resistivity at the T-O $BaTiO_3$ transition.

There is a striking hysteretic thermal behavior of $La_{0.7}Ca_{0.3}MnO_3$//$BaTiO_3$. Figure 2 shows the temperature dependence of the difference of resistivity ($\Delta\rho$) between warming and cooling runs (note the logarithmic scale). Irreversibilities ($\Delta\rho > 0$) are apparent around both metal-insulator transitions, although they are far more pronounced for the T'_{MI} freezing transition in zero fields and, curiously enough, are also strongly enhanced in the paramagnetic region. The latter persists up to the highest fields studied. Also, around T_{MI} they are very sensitive to the application of an external magnetic field. This observation rules out secondary and nonstoichiometric fractions as responsible for the appearance of a second transition at T_{MI}. In addition, the R-O $BaTiO_3$ structural transition trivially yields very large $\Delta\rho$ between 188 K and 196 K, due to its hysteretic nature.

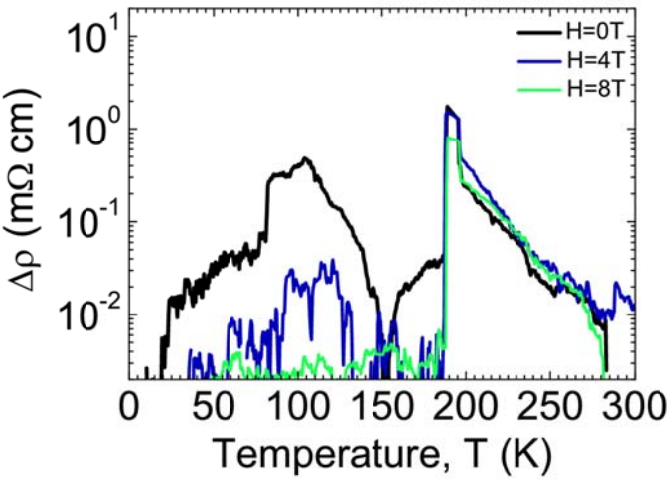

Fig.2. Temperature dependence of thermal resistivity hysteresis (Δρ) in selected magnetic fields: 0 T (black), 4 T (blue), and 8 T (green).

To explore the role of ferroelectric $BaTiO_3$ domains in the magnetic and electronic properties of $La_{0.7}Ca_{0.3}MnO_3$//$BaTiO_3$, we studied the effect on the film resistivity of electrically poling the substrate at room temperature. Figure 3 shows the resistivity of a thin (120 Å) film before and after $BaTiO_3$ poling. Upon cooling after poling, the peak at T'_{MI} remains, while the transition at T_{MI} is practically obscured by the change induced by the O-R structural transition. The low-temperature resistivity increases an order of magnitude after poling and thermal hysteresis is strongly enhanced. Interestingly, the sign of Δρ changes upon approaching the O-R transition from below. In spite of this hysteretic behaviour, the high-temperature resistance remains unchanged, assuring the reproducibility of the current paths (i.e. lack of fractures). In thicker $La_{0.7}Ca_{0.3}MnO_3$//$BaTiO_3$, the effect of the $BaTiO_3$ morphology on transport properties can also be appreciated: the resistivity around the O-R transition is dramatically altered upon poling (inset to Fig. 3), even though T_{MI} was not seen either before or after poling.

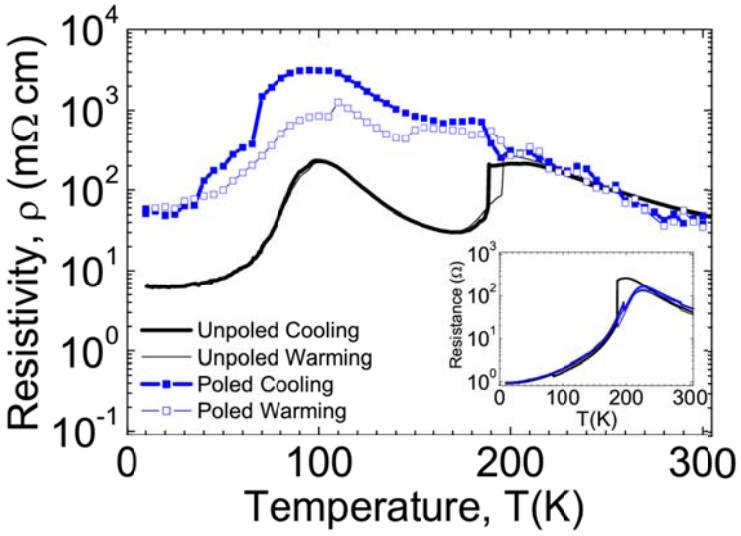

Fig.3. Temperature-dependent resistivity of 120 Å thick $La_{0.7}Ca_{0.3}MnO_3$//$BaTiO_3$ before (black lines) and after (blue lines) poling the $BaTiO_3$ substrate. The inset shows data for a thicker sample (150 Å).

MAGNETORESISTANCE

The isothermal magnetoresistance (MR) also reveals important differences between $La_{0.7}Ca_{0.3}MnO_3$//$SrTiO_3$ and $La_{0.7}Ca_{0.3}MnO_3$//$BaTiO_3$. Figure 4 shows the field dependent MR at several temperatures for 120 Å thick $La_{0.7}Ca_{0.3}MnO_3$//$SrTiO_3$ and $La_{0.7}Ca_{0.3}MnO_3$//$BaTiO_3$. Colossal MR ratios are observed at temperatures near T_C as expected in optimally doped manganites. For thin (120 Å) $La_{0.7}Ca_{0.3}MnO_3$//$BaTiO_3$, large and hysteretic MR is observed at low temperatures that is absent in either $La_{0.7}Ca_{0.3}MnO_3$//$SrTiO_3$ or thicker $La_{0.7}Ca_{0.3}MnO_3$//$BaTiO_3$. Again, hysteretic behaviour, this time with applied field, is observed for the thin $La_{0.7}Ca_{0.3}MnO_3$//$BaTiO_3$ over a broad temperature range. For temperatures above T'_{MI} hysteresis is also present in $La_{0.7}Ca_{0.3}MnO_3$//$SrTiO_3$, as expected from the percolative nature of the transition. The MR of $La_{0.7}Ca_{0.3}MnO_3$//$BaTiO_3$ remains large at low temperature, indicating lack of complete magnetic ordering. This is in agreement with the granular magnetic behaviour exhibited below the freezing temperature.

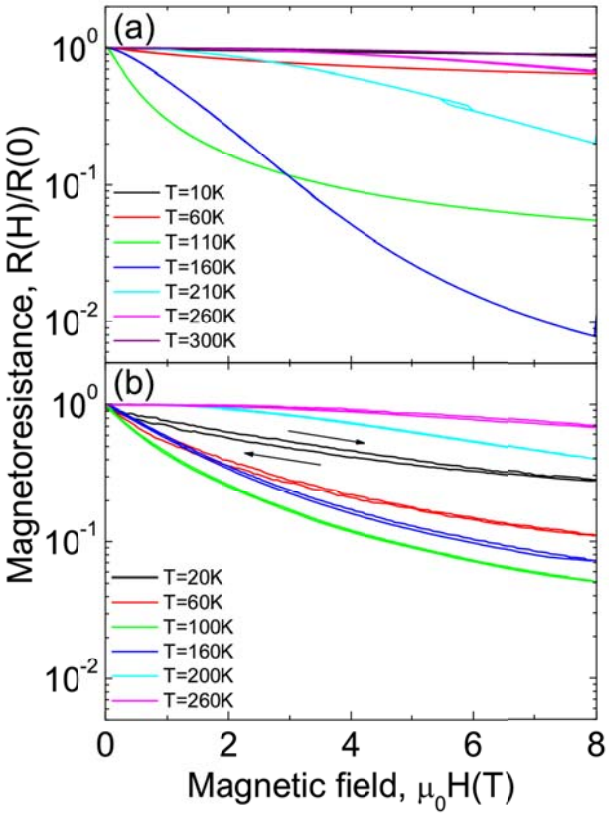

Fig.4. Magnetoresistance of (a) $La_{0.7}Ca_{0.3}MnO_3$//$SrTiO_3$ and (b) $La_{0.7}Ca_{0.3}MnO_3$//$BaTiO_3$ at selected temperatures (thickness: 120 Å in both cases).

ELECTRORESISTANCE

A complementary phenomenon to magnetoresistance, electroresistance, refers in its broadest to any nonlinear current-voltage characteristics [Wu2001]. Electroresistance is sensitive to conduction pathways and the associated distribution of potential barriers; therefore it is a good measure of electric inhomogeneity. Figure 5 shows the voltage dependent normalized resistivity R/R_0 curves (where R_0 is low bias resistance) at selected temperatures for 120 Å thin films of $La_{0.7}Ca_{0.3}MnO_3$//$SrTiO_3$ and $La_{0.7}Ca_{0.3}MnO_3$//$BaTiO_3$. Contrary to the

$La_{0.7}Ca_{0.3}MnO_3$//$SrTiO_3$ case, where it is negligible, ER in $La_{0.7}Ca_{0.3}MnO_3$//$BaTiO_3$ is significant and nontrivial. For the former, the resistance is either ohmic (linear, e.g. at 200 K) or decreases slightly ($\Delta R/R_0 <$ 1%, e.g. at 100 K and the low-voltage part at 10 K). The increase of resistance with voltage in $La_{0.7}Ca_{0.3}MnO_3$//$SrTiO_3$ (e.g. at 10 or 140 K) is a mere consequence of Joule heating in the metallic regime. This extreme was also checked with pulsed measurements at certain temperatures. Electroresistance in $La_{0.7}Ca_{0.3}MnO_3$//$BaTiO_3$ reaches 20% at T = 150 K and V = 1V. Once again, the upturn of R/R_0 for V > 1V is a consequence of Joule heating and is not considered in our analysis.

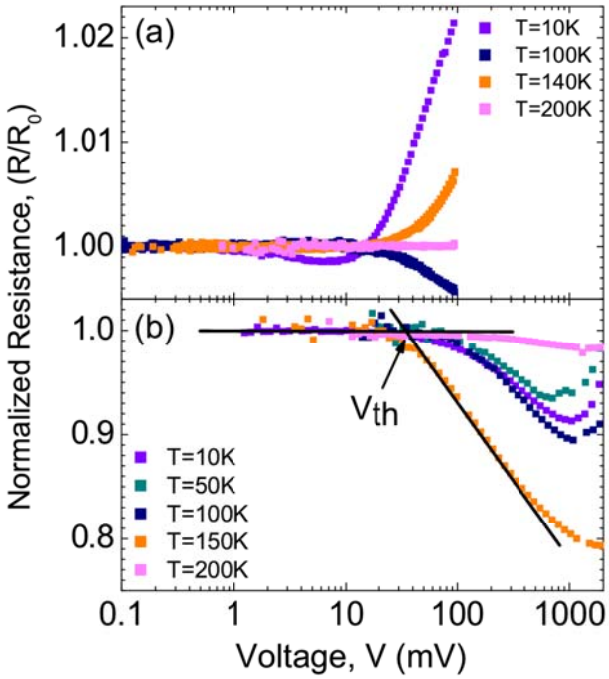

Fig.5. Resistance vs. applied voltage for (a) $La_{0.7}Ca_{0.3}MnO_3$//$SrTiO_3$ and (b) $La_{0.7}Ca_{0.3}MnO_3$//$BaTiO_3$ normalized to the low bias value R_0 at selected temperatures.

In order to quantify these data, we define the ER threshold voltage V_{th} as the voltage where R departs from ohmic behavior, as illustrated in Fig. 5(b), and ER as $\Delta R/R_0 = (R(V) - R_0)/R_0$ for $V = 2V_{th}$. We summarize these data in Figs. 6(a) and 6(b) showing the temperature dependence of threshold voltage V_{th} and ER, respectively. The threshold voltage has a broad dip centered around T ≈ 130–160 K, coinciding with the strongest ER. These salient changes of ER and threshold voltage occur in the temperature range where anomalies in the magnetic hysteresis cycles are observed and also near T'_{MI}. Note that the rather small magnitude of ER (up to 4%) is only due to our operational definition of ER, taken at $V = 2V_{th}$. To summarize our electroresistance experiments, $La_{0.7}Ca_{0.3}MnO_3$//$BaTiO_3$ shows very steep and large resistance drop above threshold up to T_{MI}, as opposed to $La_{0.7}Ca_{0.3}MnO_3$//$SrTiO_3$, which barely displays a temperature-dependent ER.

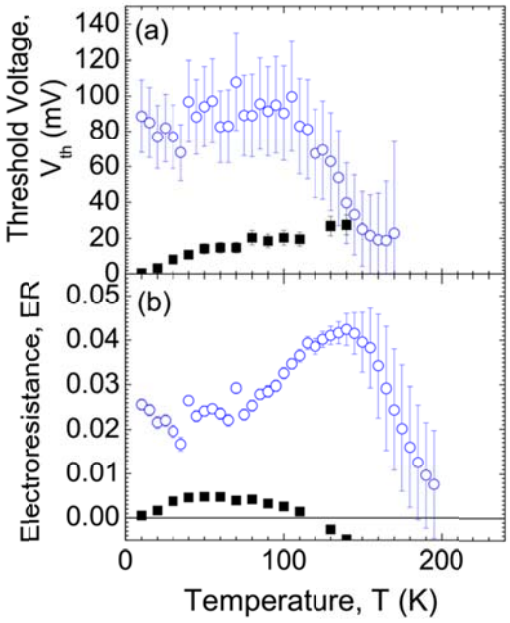

Fig.6. (a) Threshold voltage and (b) electroresistance for $La_{0.7}Ca_{0.3}MnO_3$//$SrTiO_3$ (black solid squares) and $La_{0.7}Ca_{0.3}MnO_3$//$BaTiO_3$ (blue open circles) as a function of temperature.

DISCUSSION

Magnetotransport properties are extremely sensitive to changes in double-exchange interactions, which are in turn strongly affected by the variations in the angles between MnO_6 octahedra induced by strain or by changes in the crystal field. Unlike $La_{0.7}Ca_{0.3}MnO_3$//$SrTiO_3$ films and bulk $La_{0.7}Ca_{0.3}MnO_3$, $La_{0.7}Ca_{0.3}MnO_3$//$BaTiO_3$ thin films (120 Å) show two well defined MI transitions. T_{MI} is described as the usual metal-insulator transition in ferromagnetic perovskite manganites [Dagotto2003, Tomioka2000, García-Hernandez2003]. Insulating clusters intermixed into the long-range conducting ferromagnetic order grow with increasing temperature, and electronic transport becomes dominated by electric percolation through ferromagnetic regions. As summarized in Chapter 2, the usual paramagnetic insulating phase appears above T_c. A magnetic field strengthens the ferromagnetic clusters and shifts the transition to higher temperature. However, the second transition, T'_{MI}, does not fit this picture as the magnetic field does not shift the transition temperature, suggesting that the clusters responsible for the T'_{MI} are not affected by the magnetic field, unlike the paramagnetic regions in the usual MI transition. The considerable magnetoresistance is then due to the interface between small ferromagnetic and non-ferromagnetic regions. Irreversibility between cooling and warming is usually considered a signature of the percolative nature of the transition. Around T'_{MI} the phase-separation balance changes, favouring the insulating non-ferromagnetic clusters. Structural changes of the substrate lead to evolution of the surface morphology. This drives the competition between phases. It then causes the highly hysteretic MI transition.

Although in the previous chapter we interpreted the magnetism solely on the basis of the purely ferromagnetic order with spatially inhomogeneous anisotropy (coexisting regions of in-plane and out of- plane FM interaction), hints coming from negative magnetization measured in the ZFC of some samples cannot be ignored either. In this sense, the insulating behaviour of the spins responsible for the T'_{MI} transition support the idea of antiferromagnetic correlations that could be enhanced in $La_{0.7}Ca_{0.3}MnO_3$//$BaTiO_3$ close to the $BaTiO_3$ interface and that should be also present to a much lesser extent in $La_{0.7}Ca_{0.3}MnO_3$//$SrTiO_3$ and thicker $La_{0.7}Ca_{0.3}MnO_3$//$BaTiO_3$ samples). In this picture, $La_{0.7}Ca_{0.3}MnO_3$//$BaTiO_3$ thin films would consist of

ferromagnetic regions interspersed with antiferromagnetic ones, with strong magnetic frustration at their boundaries.

This enhancement of antiferromagnetic interactions in an optimally (x = 0.3) doped manganite thin film grown on $BaTiO_3$ is also supported by other works in the literature. In 50 Å $La_{0.7}Ca_{0.3}MnO_3$ on $SrTiO_3$ [Ziese2003], under uniform strain conditions, magnetic and transport measurements have been interpreted on the basis of the existence of an antiferromagnetic-insulating phase which occupies nearly 70% of the film. Also, theoretical works predict that the tetragonal distortion induced by strain, which affects orbital ordering, can alter the phase diagram of the thin film. Indeed, for $La_{1-x}Sr_xMnO_3$ [Fang2000] the phase diagram calculated from first principles shows the stability region of the ferromagnetic order to be reduced: for x = 0.3 doping in $La_{0.7}Sr_{0.3}MnO_3$, c/a < 0.96 corresponds to antiferromagnetic order.

For our $La_{0.7}Ca_{0.3}MnO_3$//$BaTiO_3$ samples, the c/a ratio for $La_{0.7}Ca_{0.3}MnO_3$ can be estimated in the rhombohedral phase of $BaTiO_3$ from synchrotron x-ray diffraction, giving c/a = 0.98 at 132 K [Alberca2011], implying ferromagnetic order. However, in line with the magnetoelastic model described in Chapter 5, we may assume that the clusters of the $La_{0.7}Ca_{0.3}MnO_3$ layer lying close to $BaTiO_3$ are severely strained. Under this hypothesis, the tetragonality ratio would be c/a = 0.94, making the presence of an antiferromagnetic order plausible close to the interface. Finally, recent *ab initio* and two-orbital model calculations explore the effect of the electric polarization of the ferroelectric on the magnetic state of manganite in connection with manganite/ferroelectric/manganite heterostructures [Burton2011]. They conclude that interfacial spins, under various ferroelectric polarization scenarios, switch to non-ferromagnetic arrangements, most of them concerning antiferromagnetic coupling. In films thicker than a few atomic layers, antiferromagnetic arrangements would therefore coexist with ferromagnetic arrangements, giving rise to phase separation, similar to that observed in bulk $La_{0.7}Ca_{0.3}MnO_3$. These effects predominate near the ferromagnetic/ferroelectric interface over only a few unit cells, so the associated phenomenology blurs out in thicker films, akin to our observations.

With either the strain or electric-field-induced antiferromagnetic mechanism, transport properties of the $La_{0.7}Ca_{0.3}MnO_3$ layer will be very sensitive to the electric poling of the $BaTiO_3$ substrate. In these conditions, magnetoelectric effects are expected, changing the equilibrium between the manganite microphases from that corresponding to a random polarization distribution. We observed precisely this (Fig. 3): upon poling, the resistance near T'_{MI} increases, whereas the usual MI transition is depleted, showing that a larger fraction of the $La_{0.7}Ca_{0.3}MnO_3$ could be in an antiferromagnetic state. In the rhombohedral phase, the polarization lies along the unit cell diagonals. A poling process perpendicular to the sample surface at room temperature enhances the formation of larger domains oriented parallel to the applied electric field. When cooling to the rhombohedral phase, these ferroelectric domains remain with a large net component of polarization in the poling direction. These domains can act as nucleation centers for the antiferromagnetic patches. As the new ferromagnetic and antiferromagnetic magnetic domains develop simultaneously with decreasing temperature due to the new pattern of ferroelectric domains, no exchange bias in the hysteresis cycles is expected, indeed none is observed.

CONCLUSIONS

In summary, our model of a granular metallic system is confirmed by the high resistivity and large magnetoresistance at low temperatures of $La_{0.7}Ca_{0.3}MnO_3$ thin films [Alberca2012]. Between 180 and 100 K and triggered by the O-R $BaTiO_3$ phase transition, $La_{0.7}Ca_{0.3}MnO_3$//$BaTiO_3$ experiences a renormalization of the existing delicate equilibrium between intrinsic phases that was developing below T_{MI}. The magnetic/metallic granularity can be explained by the intimate mixing of antiferromagnetic and ferromagnetic phases that are overcome when ferromagnetism starts to be the dominant phase at lower temperatures. Also,

the anomalies become smoother with increasing $La_{0.7}Ca_{0.3}MnO_3$ thickness, suggesting a vertically segregated structure.

REFERENCES

[Alberca2011] Alberca, A., et al. "Exotic magnetic anisotropy map in epitaxial La0.7Ca0.3MnO3 films on BaTiO3." Physical Review B 84.13 (2011): 134402.

[Alberca2012] Alberca, A., et al. "Ferroelectric substrate effects on the magnetism, magnetotransport, and electroresistance of La0.7Ca0.3MnO3 thin films on BaTiO3." Physical Review B 86.14 (2012): 144416.

[Burton2011] J. D. Burton and E. Y. Tsymbal, Phys. Rev. B 80, 174406 (2009) & J. D. Burton and E. Y. Tsymbal, Phys. Rev. Lett. 106, 157203, (2011).

[Dagotto2003] E. Dagotto, "Nanoscale phase separation and colossal magnetoresistance: the physics of manganites and related compounds." Vol. 136. Springer, (2003)

[Fang2000] Fang, Z., I. V. Solovyev, and K. Terakura. "Phase diagram of tetragonal manganites." Physical Review Letters 84.14 (2000): 3169-3172.

[Garcia-Hernandez2003] Garcia-Hernandez, M., et al. "Disorder-induced phase segregation in La_{2/3}Ca_{1/3}MnO_{3} manganites." Physical Review B 68.9 (2003): 094411.

[Tomioka2000] Tomioka, Y., A. Asamitsu, and Y. Tokura. "Magnetotransport properties and magnetostructural phenomenon in single crystals of La_ {0.7}(Ca_ {1-y} Sr_ {y}) _ {0.3} MnO_ {3}." Physical Review B 63.2 (2000): 024421.

[Wu2001] Wu, T., et al. "Electroresistance and electronic phase separation in mixed-valent manganites." Physical Review Letters 86.26 (2001): 5998-6001.

[Ziese2003] Ziese, M., H. C. Semmelhack, and K. H. Han. "Strain-induced orbital ordering in thin La_{0.7}Ca_{0.3}MnO_{3} films on SrTiO_ 3}." Physical Review B 68.13 (2003): 134444.

CHAPTER 7

MAGNETOELASTIC COUPLING IN $La_{0.7}Ca_{0.3}MnO_3$//$BaTiO_3$ ULTRA-THIN FILMS

The complex magnetic anisotropy of $La_{0.7}Ca_{0.3}MnO_3$//$BaTiO_3$ thin films is studied in this chapter by means of Polarized Neutron Reflectometry (PNR) and Ferromagnetic Resonance (FMR). The resulting depth profiles of magnetization reveal a vertical segregated structure, confirming our predictions in Chapter 5, with a strongly suppressed magnetization throughout the thin film (300 kA/m, equivalent to a magnetic moment of 2 μB/Mn) and with largest suppression near the interface with $BaTiO_3$ (50 kA/m, equivalent to 0.3 μB/Mn).

We observe remarkable differences in FMR spectra measured in $La_{0.7}Ca_{0.3}MnO_3$//$BaTiO_3$ thin films when compared to control samples grown on $SrTiO_3$ in which low strains and no corrugation are expected. FMR is observable at 8.9 GHz only around the [110] crystallographic direction in thin $La_{0.7}Ca_{0.3}MnO_3$//$BaTiO_3$. The resonance field is hardly affected when the applied field is rotated away from [110].

Results from both techniques are addressed in terms of the magnetoelastic energy density and combined in a model of 2 magnetic layers coupled ferromagnetically: one thin layer near the interface with out-of-plane anisotropy and the other with in-plane biaxial anisotropy, typical in $La_{0.7}Ca_{0.3}MnO_3$ thin films. This model qualitatively explains the characteristics of the FMR spectra, confirming the presence of an out-of-plane spin population highly coupled magneto-elastically to the substrate.

POLARIZED NEUTRON REFLECTOMETRY

During the experiments performed at the Asterix reflectometer, we measured reflectivities of two samples, one $La_{0.7}Ca_{0.3}MnO_3$//$BaTiO_3$ and another $La_{0.7}Ca_{0.3}MnO_3$//$SrTiO_3$, both with thickness t = 120 Å. For the grown on $BaTiO_3$, we measured reflectivities at two representative temperatures: 120K, near T'_{MI} (see Chapter 6, [Alberca2012]) when ΔM is maximum in the Matteucci magnetic loops (see Chapter 5, [Alberca2011]) and 30K, far for the Curie temperature and where ferromagnetism is stronger. In the case of $La_{0.7}Ca_{0.3}MnO_3$//$SrTiO_3$, we measured the reflectivity at 90K, which is similar to 120K, as these two temperatures are similar fractions of the respective Curie temperatures. Figure 1 shows the reflectivities for these samples [Alberca2013].

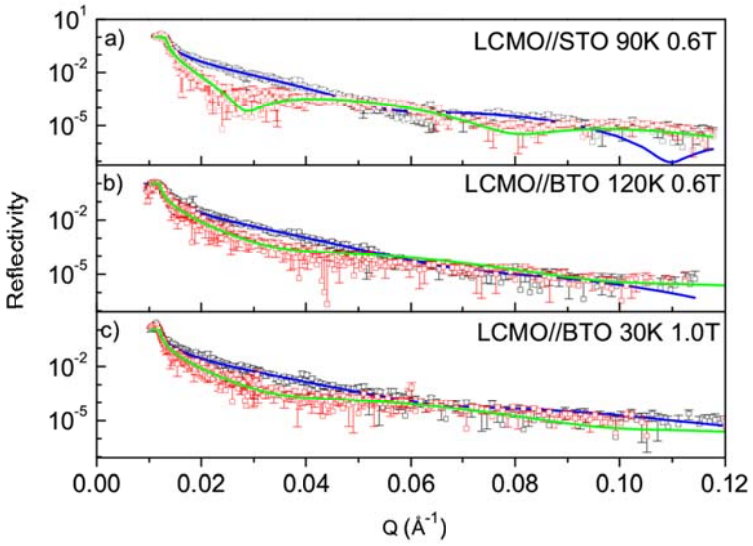

Fig.1. Non Spin-Flip Reflectivities measured on Astérix (LANSCE) for the samples and experimental conditions given. Magnetic field was applied along the easy axis, [110] direction.

Best fits to experimental data were obtained by partitioning the manganite layer profile in two zones: an upper one close to the air interface and a lower one, close to the interface with the substrate. The Nevot-Croce roughness (σ) of the interfaces, thickness (Δ) of the layers and magnetic scattering lengths (ρ_M) were left as free parameters for the fits. Best values and confidence limits are listed in Table I. The interpretation of profiles for layers with $\sigma \approx \Delta$ is best done in terms of their derivatives with respect to the depth coordinate as discussed in Ref. [Park2008]. Figure 2 shows the nuclear scattering length density (NSLD) and in-plane magnetization profiles.

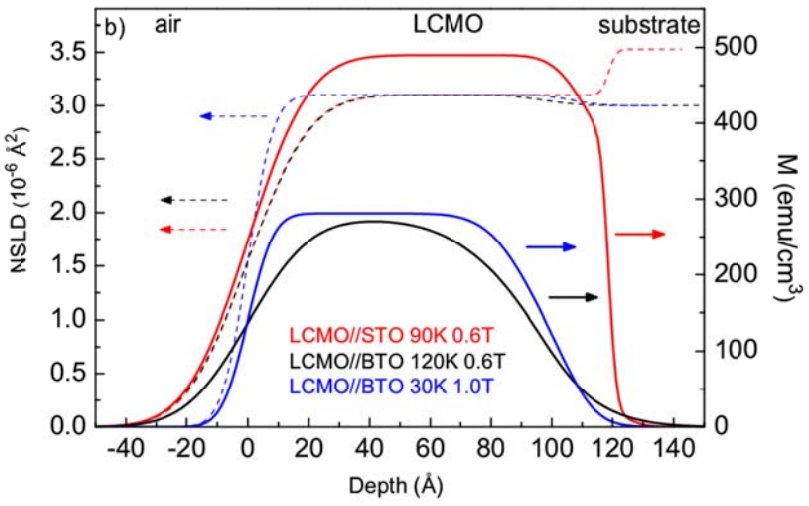

Fig.2. Magnetization and nuclear scattering length density profiles obtained with *co_nevot_croce* from the experimental data. Note the absence of a plateau in the magnetization profile of $La_{0.7}Ca_{0.3}MnO_3$//$BaTiO_3$ at 120 K, which is present both for $La_{0.7}Ca_{0.3}MnO_3$//$SrTiO_3$ and $La_{0.7}Ca_{0.3}MnO_3$//$BaTiO_3$ at 30 K.

It is apparent that near the $La_{0.7}Ca_{0.3}MnO_3$//$BaTiO_3$ interface no significant differences in NSLD exist between the results on $BaTiO_3$ at 120 and 30 K. However, the difference in M|| magnetization profiles is significant: the measurements on $BaTiO_3$ at 30 K (and on $SrTiO_3$) show a significant plateau in the central part of the magnetization profile and a steep decrease when approaching the substrate interface. On $BaTiO_3$ at 120 K this plateau is absent and M|| decreases steadily from its maximum value near the center of the $La_{0.7}Ca_{0.3}MnO_3$ layer to the interface with $BaTiO_3$ (note that best fit parameters for this zone of the $La_{0.7}Ca_{0.3}MnO_3$ layer imply $\sigma > \Delta$). We interpret this as evidence of a depletion of magnetic moments aligned with the saturating magnetic field on $La_{0.7}Ca_{0.3}MnO_3$//$BaTiO_3$ at 120 K when compared with the same system at 30 K. From our experiments, however, it is impossible to decide whether this depletion arises from a significant population of out-of-plane magnetic moments or by a vector cancellation of in-plane magnetizations corresponding to magnetic domains whose magnetic coherence length is smaller than the neutron beam coherence length (estimated in the range 1-10 μm).

Table I. Fitted values obtained with *co_nevot_croce* for the two-zone model for the $La_{0.7}Ca_{0.3}MnO_3$ layer. Numbers in brackets correspond to 68% confidence limits for the best value shown. An asterisk (*) indicates unrealistic values for the upper and lower confidence limits due to the strong correlation between Δ and σ parameters.

	Air/LCMO interface	**LCMO Upper zone (A)**			**LCMO Bottom zone (B)**		
Sample	σ (Å)	Δ (Å)	σ (Å)	ρ_M (10^{-6} Å^{-2})	Δ (Å)	σ (Å)	ρ_M (10^{-6} Å^{-2})
LCMO/STO 90K 0.6 T	16 (15.8-16.3)	112 (111-113)	9 (8-10.4)	1.4 (1.38-1.44)	7 (5.4-8.7)	2 (0.4-3)	1.0 (0.8-1.4)
LCMO/BTO 120K 0.6 T	16 (15.5-16.9)	92 (88-94)	21 (12-25)	0.8 (0.74-0.82)	6 (*)	9 (*)	0.1 (0-0.3)
LCMO/BTO 30K 1.0T	7 (4.6-7.8)	94 (91-98)	12 (6-23)	0.8 (0.76-0.84)	13 (*)	7 (*)	0.2 (0-0.3)

FMR SPECTRA

FMR spectra were recorded at 77K for four different samples: three $La_{0.7}Ca_{0.3}MnO_3$//$BaTiO_3$ thin films, one of t=150 Å and two of t=120 Å (one of the latter exhibiting Matteucci magnetic loops, see Chapter 5) and a $La_{0.7}Ca_{0.3}MnO_3$//$SrTiO_3$ with t=120 Å. The diagram in Fig. 3 shows the different orientations of the applied magnetic field, $\mathbf{B}_{applied}$, with respect to the sample surface and the corresponding values of the orientation angles.

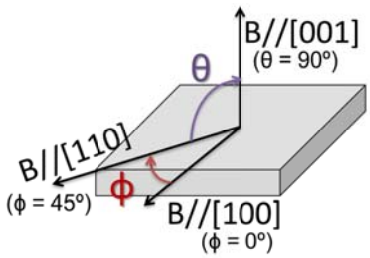

Fig.3. Schematics of the geometry of magnetic field with respect to the sample.

Figures 4-6 show the FMR spectra for the $La_{0.7}Ca_{0.3}MnO_3$//$SrTiO_3$, $La_{0.7}Ca_{0.3}MnO_3$//$BaTiO_3$ (150 Å) and $La_{0.7}Ca_{0.3}MnO_3$//$BaTiO_3$ (120 Å), respectively. The spectra are offset vertically by the corresponding orientation angle of the applied field. Left panels show the in-plane rotations where 0° denotes field applied along the [100] direction, B//[100], and 45º along the B//[110] direction. Right panels show rotations from B//[100] to the B//[001] (out-of-plane) direction for $La_{0.7}Ca_{0.3}MnO_3$//$SrTiO_3$ and rotations from B//[110] to the B//[001] direction for $La_{0.7}Ca_{0.3}MnO_3$//$BaTiO_3$. For the four films, out-of-plane rotations reveal the hard axis, along [001], and in-plane rotations show an easy axis along the [110], where the resonance field, denoted as B_0, is observed. However, several striking differences between them can be observed:

- The FMR signal is much weaker in $La_{0.7}Ca_{0.3}MnO_3$//$BaTiO_3$ than in $La_{0.7}Ca_{0.3}MnO_3$//$SrTiO_3$.
- $La_{0.7}Ca_{0.3}MnO_3$//$BaTiO_3$ shows considerably broader resonances and, unlike for $La_{0.7}Ca_{0.3}MnO_3$//$SrTiO_3$, these get sharper near the B//[110] and B//[001] directions.
- For $La_{0.7}Ca_{0.3}MnO_3$//$BaTiO_3$ when the applied field is rotated away from the film plane, no FMR can be conclusively identified in an experiment where the in-plane direction is along [100] [Figs. 5(a) and 6(a)].
- When the field rotation starts from [110] and progresses towards [001], the FMR is well resolved up to approx. θ ~ 75-80° and the FMR shifts to higher field rather slowly, staying near the easy axis value.
- Close to B//[001], or perpendicular to the film plane, the FMR appears as a sharp resonance at high field, just below the limit of the maximum field of the spectrometer [Fig. 5(b)].

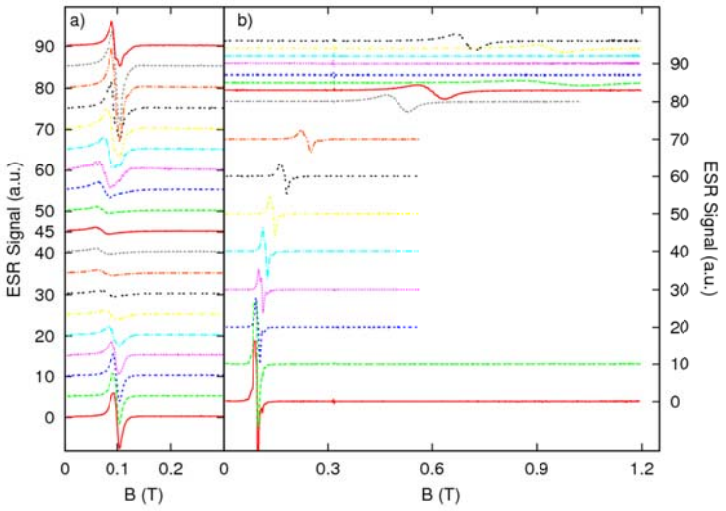

Fig.4. FMR spectra with various magnetic field orientations (a) in-plane, (b) out-of-plane, of a 120 Å thick $La_{0.7}Ca_{0.3}MnO_3$ film on $SrTiO_3$ at 77K. The spectra are offset for clarity and their baseline value corresponds to the orientation angle.

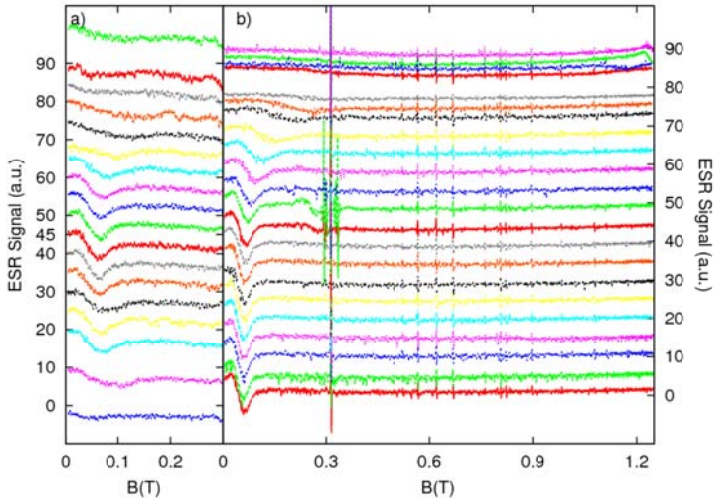

Fig.5. FMR spectra with various magnetic field orientations a. in-plane, b. out-of-plane, of a 150 Å thick $La_{0.7}Ca_{0.3}MnO_3$ film on $BaTiO_3$ at 77K. The spectra are shifted vertically and their baseline value corresponds to the orientation angle. The resonance observed at 0.3 T is DPPH used as reference.

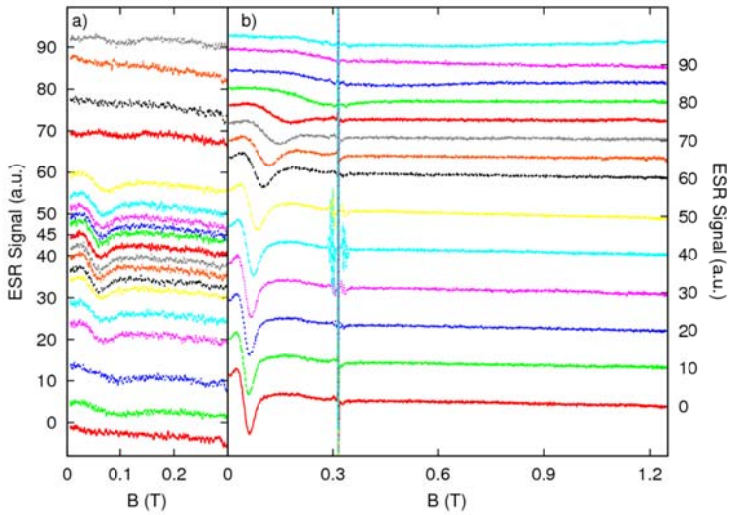

Fig.6. FMR spectra with various magnetic field orientations a. in-plane, b. out-of-plane, of a 120 Å thick $La_{0.7}Ca_{0.3}MnO_3$ film on $BaTiO_3$ at 77K. The spectra are shifted vertically and their baseline value corresponds to the orientation angle. The resonance observed at 0.3 T is DPPH used as reference.

The obtained resonance fields (B_0) are plotted vs. the rotation angle in Fig. 7(a)-7(c) (in-plane rotations) and Fig. 7(d)-7(f) (out-of-plane) for $La_{0.7}Ca_{0.3}MnO_3$//$SrTiO_3$ (120 Å), $La_{0.7}Ca_{0.3}MnO_3$//$BaTiO_3$ (150 Å), and $La_{0.7}Ca_{0.3}MnO_3$//$BaTiO_3$ (120 Å), respectively. Out-of-plane resonance fields are plotted in Fig. 7(d)-7(f). FMR for both $La_{0.7}Ca_{0.3}MnO_3$//$BaTiO_3$ [Figs. 7(e) and 7(f)] was measured with B-field between [110] in-plane ($\theta = 0°$, see Fig. 3) and [001] out-of-plane ($\theta = 90°$). For $La_{0.7}Ca_{0.3}MnO_3$//$SrTiO_3$ [Fig. 7(d)] the in-plane direction was less critical and was chosen as [100] ($\phi = 0°$). The in-plane data [Fig. 7(a)-7(c)] show typical sinusoidal variation, characteristic of biaxial symmetry with easy axes along the four [110] directions. However, as Figs. 5 and 6 demonstrate, around [100] no resonance could be resolved in $La_{0.7}Ca_{0.3}MnO_3$//$BaTiO_3$ samples. In out-of-plane rotations of $La_{0.7}Ca_{0.3}MnO_3$//$BaTiO_3$ [Figs. 7(e) and 7(f)], the

FMR barely shifts until 50° and then starts to slowly creep upwards up to 75° where it rapidly broadens and disappears. Sharper resonances appear around 1T near the [001] orientation in the thicker $La_{0.7}Ca_{0.3}MnO_3$//$BaTiO_3$ (150Å) film. Narrow lines in the spectra around 0.33 T (g=2) correspond to the electron paramagnetic resonance (EPR) of the reference 2,2-diphenyl-1-picrylhydrazyl (DPPH). Other, angular dependent, lines around 0.6 T correspond to EPR of defects in the substrates.

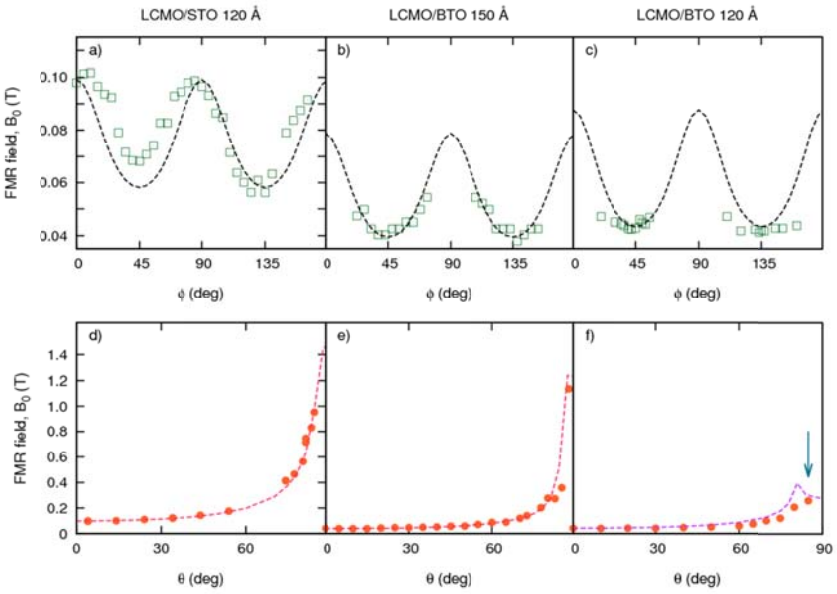

Fig.7. FMR resonance fields for the $La_{0.7}Ca_{0.3}MnO_3$//$SrTiO_3$ 120Å in-plane (a) and out-of-plane (d), $La_{0.7}Ca_{0.3}MnO_3$//$BaTiO_3$ 150 Å in-plane (b) and out-of-plane (e), and $La_{0.7}Ca_{0.3}MnO_3$//$BaTiO_3$ 120 Å in-plane (c) and out-of-plane (f), as extracted from FMR spectra shown in Figures 4-6. Lines correspond to simulations using Eq. [1] and parameters listed in Table II.

ANISOTROPY ENERGIES

For the interpretation of the FMR results we use a classical free energy anisotropy model to determine first the equilibrium magnetization orientation for a given applied field (magnitude and direction): $\mathbf{M}(\mathbf{B}_{applied})$ and the eigenoscillation around this equilibirium. We then vary the magnitude of $\mathbf{B}_{applied}$ until the eigenfrequency equals the frequency of the simulated experiment, we denote $\mathbf{B}_{applied}$ by B_0. The free energy includes the Zeeman energy and shape anisotropy terms and the power series of the directional cosines as the anisotropy energy [Chikazumi2009]:

$$E/V = -\mu_0 \mathbf{M}\cdot\mathbf{B}_{applied} + \tfrac{1}{2}\mu_0 \mathbf{M}\cdot\mathbf{N}\cdot\mathbf{M} + K_{2c}\alpha_3^{\,2} + K_{4ab}(\alpha_1^{\,4} + \alpha_2^{\,4}) + K_{4c}\alpha_3^{\,4} \qquad [1]$$

Where V is the volume of the ferromagnetic layer, α_1, α_2 and α_3 are the direction cosines of the $La_{0.7}Ca_{0.3}MnO_3$ magnetization ($\alpha_i = \mathbf{M}_i/M_{sat}$, i= 1,2,3 and $\alpha_1^{\,2} + \alpha_2^{\,2} + \alpha_3^{\,2} = 1$), $\mathbf{N}$ is the demagnetization tensor ((N_{11},N_{22},N_{33})=(0,0,1) in the case of a film perpendicular to the z-axis), K_{2c} is the lowest order out-of-plane anisotropy term, K_{4c} the next order, K_{4ab} is the lowest order in-plane anisotropy term and M_{sat} is the saturation magnetization (determined from VSM).

Here, for the $La_{0.7}Ca_{0.3}MnO_3$//$SrTiO_3$ layer we obtained K_{2c}= + 140 ± 30 kJ/m^3 and K_{4ab}= + 1.7 ± 0.5 kJ/m^3 (see Table II). No higher order terms appearing in Eq. [1] were needed to describe the fundamental features of

$La_{0.7}Ca_{0.3}MnO_3$//$SrTiO_3$. In Ref. [Nemes2008], lower values, K_{2c}= + 48 kJ/m^3 and K_{4ab}= + 1.6 kJ/m^3, were obtained for t = 150 Å thick $La_{0.7}Ca_{0.3}MnO_3$//$SrTiO_3$. Simulations of the angular dependence of the FMR B_0 with these parameters are shown in Fig. 7 (a) and 7 (d).

FMR spectra of a t = 120 Å $La_{0.7}Ca_{0.3}MnO_3$//$BaTiO_3$, not exhibiting Matteucci-loops, are shown in Fig. 6. As in the case of the 150 Å thick $La_{0.7}Ca_{0.3}MnO_3$//$BaTiO_3$, no resonance was observed near the B//[100] and, although, B//[110] remains the easy axis, its shift to higher fields is small [Fig. 6(a)] away from [110]. The out-of-plane rotations are in Fig. 6(b), again, resonance fields shift slowly up when rotating to B//[001] remaining at B_0 ~ 0.3 T even at 80°. In the thinner layer no resonance was observed around B//[001] within the limit of our spectrometer. Compared with $La_{0.7}Ca_{0.3}MnO_3$//$SrTiO_3$, broad and weak signals are characteristic of these spectra. Figure 7(c) and 7(f) show the in-plane and out-of-plane angular dependence of the resonance fields, respectively. The corresponding parameters for Eq. [1] of the FMR simulation are summarized in Table II. Remarkably, in another thin 120 Å $La_{0.7}Ca_{0.3}MnO_3$//$BaTiO_3$ film, which did exhibit Matteucci magnetic loops, no FMR could be observed for any magnetic field orientation.

A strong tendency for out-of-plane orientation of the magnetic moments is apparent in $La_{0.7}Ca_{0.3}MnO_3$//$BaTiO_3$: the FMR can be described by incorporating the fourth order out-of-plane K4c term, with values given in Table II. The salient feature of these results is the large and negative K4c = - 70 ± 20 kJ/m^3 for the thicker layer and K4c = - 140 ± 20 kJ/m^3 for the thinner layer. Indeed, the out-of-plane FMR of $La_{0.7}Ca_{0.3}MnO_3$//$BaTiO_3$ cannot be described without recurring to the K_{4c} term not needed for $La_{0.7}Ca_{0.3}MnO_3$//$SrTiO_3$. This large, negative K_{4c} term yields the low values of the resonance field near [001]. Indeed, the curious backwards turn of the simulation near [001] is a direct consequence of K_{4c} being comparable to K_{2c} but negative.

Table II. Anisotropy energies of 120 Å $La_{0.7}Ca_{0.3}MnO_3$//$SrTiO_3$ and $La_{0.7}Ca_{0.3}MnO_3$//$BaTiO_3$ and 150 Å $La_{0.7}Ca_{0.3}MnO_3$//$BaTiO_3$ at 77K. t_B is the estimated 30 Å thickness of the highly strained sub-layer near the $BaTiO_3$.

	K_{2c}[kJ/m^3]	K_{4c} [kJ/m^3]	K_{4ab} [kJ/m^3]	M_{sat}[kA/m]/m_{sat}[μ_B/Mn]	t^B/t^A
LCMO/STO (120 Å)	140±30	-	1.7±0.5	400/2.52	0
LCMO/BTO (150 Å)	220±30	-70±20	2.1±0.7	379/2.38	0.25
LCMO/BTO (120 Å)	190±50	-140±20	2.1±0.7	375/2.36	0.33

The large negative K_{4c} indicates the existence of a fraction of magnetic moments that prefer to be out-of-plane in $La_{0.7}Ca_{0.3}MnO_3$//$BaTiO_3$. The overall energy balance, K_{2c} and the shape anisotropy keep the sample plane as the easy plane of the system. Yet, a negative K_{4c} comparable to K_{2c} is needed to simulate the low resonance field, implying a tendency of spins to be out-of-plane. The non-uniform distribution of magnetization extracted from PNR depth profiles indicates that the non-aligned population of spins must reside near the interface with the substrate. The influence of these out-of-plane spins in the macroscopic properties is thickness dependent. In thicker layers (t > 150 Å) the effect of these spins in magnetic and transport properties weakens [Alberca2012]. In this sense, the relative amount of the two populations plays an important role. We consider the ratio t_B/t_A, where t_B is the thickness of the sub-layer at the interface with $BaTiO_3$ estimated from PNR (see Fig. 2) to be 30 Å and t_A is the thickness of the more relaxed sub-layer further from the $BaTiO_3$. As t_A increases with $La_{0.7}Ca_{0.3}MnO_3$ film thickness, K_{4c} diminishes (Table II). Also, the small reduction of K2c in the thinner layer can be a result of an increase of K_{4c}. In this respect, $La_{0.7}Ca_{0.3}MnO_3$//$SrTiO_3$ can be considered as the limit $t_B \rightarrow 0$.

MAGNETOELASTIC ENERGY DENSITY

The highly negative anisotropy shown in the previous section can be addressed just by looking at the magnetoelastic energy density. Internal strains in thin films due to the substrate (as high as 2% in $La_{0.7}Ca_{0.3}MnO_3$//$BaTiO_3$ [Alberca2011]) affect significantly the magnetic anisotropy through magnetoelastic coupling. Here, we turn to the more general expression of the free energy density in powers of strains, ε_{ij}:

$$E/V = K_{ij}\alpha_i\alpha_j + B_{ij}\alpha_i\alpha_j\varepsilon_{ij} + D_{ijkl}\alpha_i\alpha_j\alpha_k\alpha_l\varepsilon_{ij}\varepsilon_{kl} + \ldots + C_{ijkl}\varepsilon_{ij}\varepsilon_{kl} + \ldots \quad [2]$$

This expansion includes the magnetocrystalline anisotropy (MCA) energy density, with coefficients $K_{ij,}$ as the zero order term, the magnetoelastic energy density with coefficients of first (B_{ij}) and second (D_{ijkl}) order, as well as the elastic energy density terms (C_{ijkl}) [Chikazumi2009, Lacheisserie2006, Lacheisserie1993, delMoral2008]. When strains are less than 1%, as in the case of $La_{0.7}Ca_{0.3}MnO_3$//$SrTiO_3$, only linear terms are needed. Then, by minimizing the elastic and magnetoelastic contributions and incorporating them to the MCA, it is possible to calculate analytical expressions for the anisotropic constants of Eq. [1]. For a cubic system, assuming a coherently strained film with in-plane strain $\varepsilon_{xx} = \varepsilon_{yy} = \varepsilon$, ignoring shear in-plane, $\varepsilon_{xy}=0$, and denoting the out-of-plane strain as $\varepsilon_{zz} = \varepsilon_z$, the anisotropy constants in Eq. [1] can be expressed as follows:

$$\begin{aligned} K_{2c} &= K_{2z,MCA} + B_1(\varepsilon_z - \varepsilon) + B_2^2/(2c_{44}) \\ K_{4ab} &= K_{4xy,MCA} \\ K_{4c} &= K_{4z,MCA} + B_2^2/(2c_{44}) \end{aligned} \quad [3]$$

where B_1 and B_2 are the magnetoelastic coefficients, c_{44} the elastic modulus and $K_{2z,MCA}$, $K_{4xy,MCA}$ and $K_{4z,MCA}$ are the MCA coefficients [Vaz2009, O'Donnell1998, Chang1993].

For higher strains (1-3%) and also in presence of corrugation at the interface, terms quadratic in strains are needed [O'Handley1992, Lacheisserie1982, Kittel1996]. High corrugation can cause larger shears which in turn strongly affect the anisotropy, yielding very complex analytical expressions, beyond the scope of the present work. Nonetheless, assuming cubic symmetry, with zero in-plane shear, $\varepsilon_{xy}=0$, but small out-of-plane shears, ε_{xz} and ε_{yz}, (ie. terms of the form $\varepsilon_{ij}\varepsilon_{kl}$ and $\varepsilon_{ii}\varepsilon_{kl}$ are neglected) similar calculations can lead to expressions for the anisotropy constants. Thus, the proposed approximations eliminate a considerable number of magnetoelastic coefficients and the anisotropy constants read as:

$$\begin{aligned} K_{2c} &= K_{2z,MCA} + B_1(\varepsilon_z - \varepsilon) + B_2^2/(2c_{44}) \\ K_{4ab} &= K_{4xy,MCA} + D_{12}\varepsilon\varepsilon_z + D_{11}\varepsilon^2 \\ K_{4c} &= K_{4z,MCA} + B_2^2/2c_{44} + D_{12}\varepsilon^2 + D_{11}\varepsilon_z^2 \end{aligned} \quad [4]$$

where the dependence of K_{4c} and K_{4ab} on strains is now explicit. When strains are small, K_{4c} is dominated by $K_{4z,MCA}$. Since B_2 is proportional to magnetostriction, λ_{111}, B_2^2 is considerably smaller than B_1 and the term $B_2^2/(2c_{44})$ can be neglected [Kittel1996]. This results in the expected $K_{2c} \neq 0$ and $K_{4c} \approx 0$ for systems like $La_{0.7}Ca_{0.3}MnO_3$//$SrTiO_3$. Now, the case of high strains includes new magnetoelastic coefficients (D_{12} and D_{11} in this approximation), that add to the anisotropy constants. Thus, negative magnetoelastic coefficients can lead to the high negative value of K_{4c} coefficient in $La_{0.7}Ca_{0.3}MnO_3$//$BaTiO_3$ thin films.

THE TWO-LAYER MODEL

In this section we reach back to the idea discussed in Chapter 5 of two different populations of spins in $La_{0.7}Ca_{0.3}MnO_3$//$BaTiO_3$ [Alberca2011]. In sight of PNR results of a vertically segregated structure and supported by magnetoelastic theory discussed in section IV, we propose a two layers model that might be able to explain the differences in FMR spectra between $La_{0.7}Ca_{0.3}MnO_3$//$BaTiO_3$ and $La_{0.7}Ca_{0.3}MnO_3$//$SrTiO_3$ thin films. It is the large out-of-plane anisotropy (indicated by the negative K_{4c}) and the strongly suppressed depth-dependent in-plane magnetization seen by PNR that lead us to postulate a two-layer model. One sub-layer corresponds to relaxed $La_{0.7}Ca_{0.3}MnO_3$, akin to $La_{0.7}Ca_{0.3}MnO_3$//$SrTiO_3$, with in-plane magnetic anisotropy (positive K_{2c}). The other one is highly affected by inhomogeneous strain from the $BaTiO_3$ substrate, with out-of-plane anisotropy (negative K_{2c}). By considering these two regions, the magnetic granularity and many of the unusual properties observed in magnetism and transport can be explained.

In the following, we discuss the model, and simulations of the corresponding FMR. We express the free energy areal density of the system as the sum of two different populations of spins distributed as layers of different thicknesses, coupled together at the interface:

Sub-layer A: We assume a top-layer with anisotropy constants found for $La_{0.7}Ca_{0.3}MnO_3$//$SrTiO_3$ with in-plane easy axis: K^A_{2c} = + 140 kJ/m^3 and K^A_{4ab} = + 1.7 kJ/m^3 (see Table II) and saturation magnetization, based on VSM measurements: M_A= 379 kA/m (2.5 μ_B/Mn).

Sub-layer B: For the bottom layer, highly affected by the $BaTiO_3$ substrate, we assume out-of-plane easy axis, ie., negative anisotropy constant K^B_{2c}. Here we proceed as suggested in Ref. [O'Handley1992] where the negative K_{4c} is included as an effective K_{2c} that accounts for the large strains and corrugation. In addition, according to Eq. [4] a large, negative K^B_{4ab} can be expected. The thickness and magnetization of this sub-layer are estimated from PNR as t^B = 30 Å and M^B = 50 kA/m (0.3 μ_B/Mn).

We consider in the free energy the corresponding volumetric Zeeman and shape anisotropy terms and finally the simplest coupling between sub-layers, an interfacial exchange type ferromagnetic coupling of the adjacent Mn ions. The resulting free energy density is:

$$
\begin{aligned}
&E / A = \\
&[-\mu_0 \mathbf{M^A}\cdot\mathbf{B}_{applied} + \tfrac{1}{2}\mu_0 \mathbf{M^A}\cdot N\cdot\mathbf{M^A} + K^A{}_{2c}\alpha^A{}_3{}^2 + K^A{}_{4ab}(\alpha^A{}_1{}^4 + \alpha^A{}_2{}^4)]\cdot t^A \\
&+[-\mu_0 \mathbf{M^B}\cdot\mathbf{B}_{applied} + \tfrac{1}{2}\mu_0 \mathbf{M^B}\cdot N\cdot\mathbf{M^B} + K^B{}_{2c}\alpha^B{}_3{}^2 + K^B{}_{4ab}(\alpha^B{}_1{}^4 + \alpha^B{}_2{}^4)]\cdot t^B \\
&- J_{eff}\rho_S \mathbf{S}^A\mathbf{S}^B
\end{aligned}
\qquad [5]
$$

where $\alpha^j_i = \mathbf{M}^j_i/M^j_{sat}$, i= 1,2,3 and $\alpha^j_1{}^2 + \alpha^j_2{}^2 + \alpha^j_3{}^2 = 1$, j=A or B, N is the demagnetization tensor ($(N_{11},N_{22},N_{33})=(0,0,1)$, A is the (arbitrary) surface of the layer, ρ_S the surface density of Mn ions (spins/area), $S^j = M^j/(-g^j\times\mu_B\times\rho^j)$ is the polarization (expectation value) of the spin in the j-th layer, ρ^j is the density of the spins in the j-th layer, and $t = t^A+t^B$ = 150 Å is the total $La_{0.7}Ca_{0.3}MnO_3$ film thickness. We focus on simulations (maps of FMR intensity over the magnetic field / excitation frequency plane) for the t = 150 Å thick $La_{0.7}Ca_{0.3}MnO_3$//$BaTiO_3$ film. With the experimental values of M^A, M^B, t^A and t^B, and the anisotropy constants of the $La_{0.7}Ca_{0.3}MnO_3$//$SrTiO_3$ used for the upper layer, only K^B_{2c}, K^B_{4ab} and J_{eff} remain as free parameters for the simulations. We selected these so as to capture most of the qualitative features of the experimental FMR listed in Section II. Table III gives the values best approximating the experimental results, as described below.

Table III. Simulation parameters at 77K used in the two layers modes described by Eq. [5]. The coupling value used is $J_{eff} \approx 4 \cdot 10^{-23}$ kJ ~ 250 meV per spin pair.

	K_{2c} [kJ/m^3]	K_{4ab} [kJ/m^3]	M_{sat}[kA/m]	t [Å]
Sub-Layer A	140	1.7	379	120
Sub-Layer B	-220±30	-50±10	50	30

The resonance modes and frequencies of this system of coupled ferromagnetic layers can be calculated once all the parameters, including the size and direction of $\mathbf{B}_{applied}$ are fixed: We determine first the equilibrium orientation of $\mathbf{M}^A$ and $\mathbf{M}^B$ by minimizing E. Then the coupled equations of motion for $\dot{\mathbf{M}}^j=\gamma_j$ ($\mathbf{M}^j \times \mathbf{B}_{eff}^j$) are solved after linearization for small variations of $\mathbf{M}^j$ from their equilibrium. The coupling emerges from the (dynamic) exchange torque produced by the layers on each other. To simulate the orientation dependence of the FMR (recorded by sweeping $\mathbf{B}_{applied}$ at a fixed frequency), for each orientation we varied the magnitude of $\mathbf{B}_{applied}$ systematically until one of the resonance frequencies matched the measurement frequency.

The FMR mode can exhibit fairly complex behavior, especially for the two-layer model. For comparison, simulations for $La_{0.7}Ca_{0.3}MnO_3$//$SrTiO_3$ are shown in Fig. 8(a)-8(c). These 2D FMR maps show expected microwave absorption (in a false color scale) as a function of the excitation frequency and applied magnetic field, at three representative orientations: with the magnetic field applied along the two principal in-plane directions, [100] and [110], and in the out-of-plane orientation [001]. The shift of the whole mode between the in-plane easy and hard axes is determined by K_{4ab}. Around the hard axis the resonance mode is dominated by K_{2c}, where Zeeman and anisotropy energies compete in the magnetization process, resulting in the initial downturn of the resonance mode and its final upturn [Fig. 8(c)] for strong enough fields to reach magnetic saturation [Fig. 8(i), black line, around 1.2 T). The FMR mode crosses the excitation microwave frequency (indicated as green lines at 8.9 GHz) at smaller magnetic field in the expected [110] direction, in agreement with this being the easy axis given by the positive K_{4ab} of the simulation. In the out-of-plane orientation [Fig. 8(c)], the resonance is predicted above the experimentally available magnetic field (at B = 1.2 T), in accordance with no resonance observed for this direction in Fig. 4. The relative intensity of the resonances at different orientations observed in $La_{0.7}Ca_{0.3}MnO_3$//$SrTiO_3$ spectra is also reproduced: the intensity of the resonance near the easy axis is lower than around the B//[100].

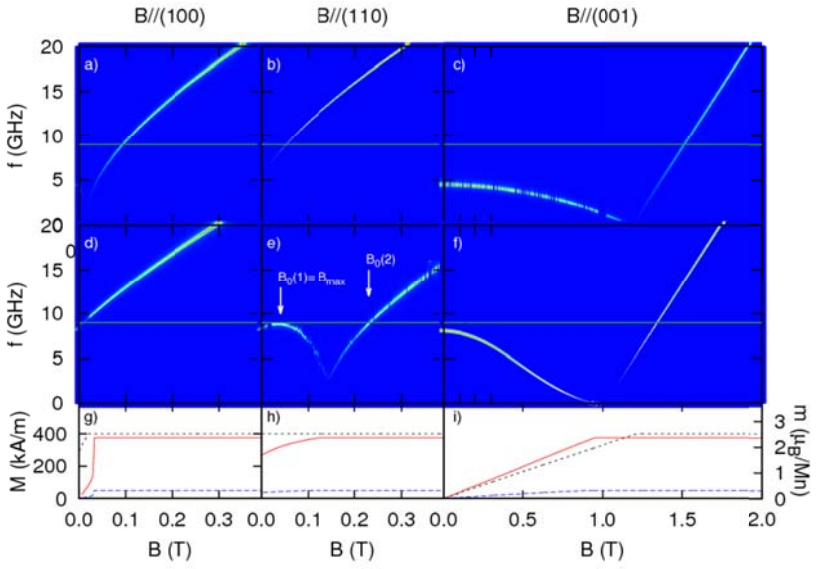

Fig.8. FMR maps calculated for the $La_{0.7}Ca_{0.3}MnO_3$//$SrTiO_3$120 Å layer (upper panels) and the $La_{0.7}Ca_{0.3}MnO_3$//$BaTiO_3$ 150 Å layer (central panels) in three selected applied field orientations B//[100], B//[110] and B//[001]. For the $La_{0.7}Ca_{0.3}MnO_3$//$SrTiO_3$ layer a 1-layer model described by equation 1 was used. In the case of $La_{0.7}Ca_{0.3}MnO_3$//$BaTiO_3$ sample the 2-layer model described by Eq. [5] was used. Green line indicates the experimental microwave excitation frequency. Lower panels show the simulated magnetic loops in the direction of the applied magnetic field for $La_{0.7}Ca_{0.3}MnO_3$//$SrTiO_3$ (black), and $La_{0.7}Ca_{0.3}MnO_3$//$BaTiO_3$ sub-layer A (red) and sub-layer B (blue).

We employ the two-layer model of Eq. [5] to describe the magnetism of $La_{0.7}Ca_{0.3}MnO_3$//$BaTiO_3$. A complex FMR mode results from the coupling of the individual resonances of the two sub-layers. The model has 9 parameters of which we fix 6 based on experiment, as discussed above: the two magnetizations, the sub-layer thicknesses, and the in-plane K^A_{4ab} and out-of-plane K^A_{2c} anisotropy constants of the top-layer. There is no obvious guidance from experiment for the other 3 parameters: K^B_{4ab}, K^B_{2c} and the A-B layer coupling, J_{eff}. We studied a large set of simulated FMR maps varying all three parameters systematically, until a parameter-set was found that reproduces the important features, described in Section II, of the FMR data qualitatively. These parameters are given in Table III, and the corresponding FMR maps in the three main orientations of the magnetic B-field are shown in Figs. 8(d)-8(f).

In the following we discuss each of the free parameters of the two-layer model separately by comparing their effects on the simulated FMR maps to the experiment.

The most striking difference of the FMR maps of the two-layer model with respect to the one-layer model is that in the [110] orientation the low frequency, experimentally achievable, mode shows a maximum frequency in low applied B-field, indicated as B_{max} in Fig. 8(e). We tuned this "bump" with the chosen model parameters to be just above the measurement frequency, 8.9 GHz, indicated with a green line. In-plane characteristics of the observed spectra in $La_{0.7}Ca_{0.3}MnO_3$//$BaTiO_3$ are determined mainly by K^B_{4ab}. The model forces us to use a large negative K^B_{4ab} anisotropy constant in order to push the B_{max} "bump" up to observable frequencies. For certain orientations near [110] of the applied B-field, the two-layer model predicts more than one FMR peaks. We identify the experimental FMR with the low-field peak, $B_0(1)$~B_{max}, and will comment below on why the higher-field peak, $B_0(2)$ reminiscent of the resonance of the one-layer model, is not observed except for near perpendicular directions. Figures 8(d)-8(f), show the FMR maps with K^B_{2c} = -220 kJ/m^3, K^B_{4ab} = -50 kJ/m^3 and $J_{eff} = 4 \cdot 10^{-23}$ kJ (~ 250 meV) per interfacial spin pair to simulate the observed FMR of 150 Å thick $La_{0.7}Ca_{0.3}MnO_3$//$BaTiO_3$.

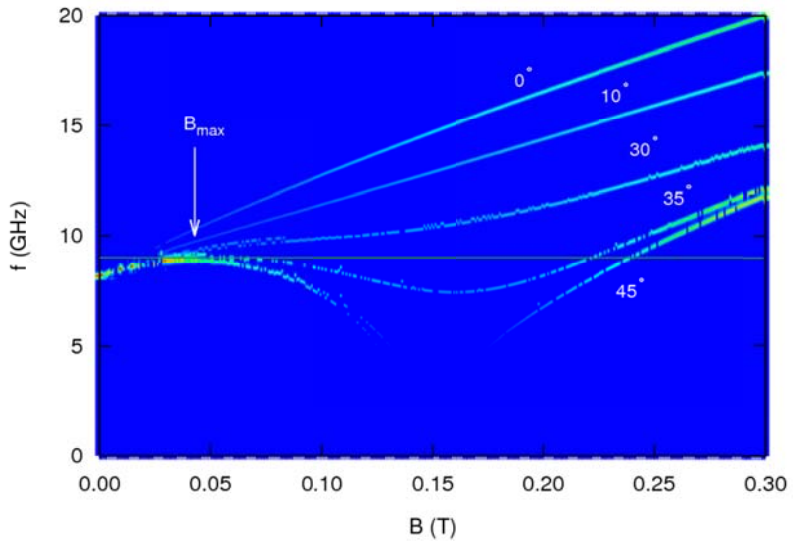

Fig.9. Overlayed FMR maps where B is rotated in-plane from B//[100] (ϕ = 0°) to B//[110] (ϕ = 45°). Resonance $B_0(1)$ is only observed after a certain angle is reached (ϕ = 35° in our model), then it moves to lower fields.

When the magnetic field is applied near [110], the direction where experimentally FMR were observed, the two-layer model has a minimum frequency, corresponding to the reorientation/saturation of the magnetization. In low fields the bottom layer forces the top layer to bend towards [100] and [001]. This minimum slowly rises and then disappears as the field is oriented towards [100], as shown in Fig. 9. Crucially, at the experimental 8.9 GHz frequency the observed FMR is more intense near [110] than along B//[100] and it is also broadened around B//[110]. Both effects are direct consequences of the "bump" feature of the resonance around 0.04 T, since the observation at fixed frequency cuts the mode tangentially, precisely near [110]. This $B_0(1)$ resonance in Fig. 9 barely moves when rotating in-plane and finally disappears towards B//[100], concurrent with the lack of resonance observed there in $La_{0.7}Ca_{0.3}MnO_3$//$BaTiO_3$. Quantitatively, the simulated FMR disappears already 10° away from [110] contrary to experiment where it is observed up to 20°, indicating the limits of our model. Nevertheless, the model predicts $B_0(1)$ to be smallest at B//[110], in agreement with experiment.

Figure 10 shows FMR maps using the same model parameters but different top layer thickness. Interestingly, for a total layer of 120 Å, the resonance mode is raised over the experimental frequency, coinciding with the lack of observable resonance in the $La_{0.7}Ca_{0.3}MnO_3$//$BaTiO_3$ Matteucci sample. At the other extreme, the thickness needed to get the FMR maps to approximate $La_{0.7}Ca_{0.3}MnO_3$//$SrTiO_3$, is 1000 Å with the parameters of Table III. This thickness is much larger than the 250 Å expected experimentally according to magnetic characterization in Ref. [Alberca2012]. Quantitative agreement between model and experiment is not expected as the complexity derived from the interface with the inhomogeneous $BaTiO_3$ substrate, with varying topography and ferroelectric domain distribution is addressed in our model only through K^B_{4ab}. As a result, we are forced to use a rather large in-plane K^B_{4ab} to reproduce the qualitative features of the FMR experiment. Yet, the magnetoelastic calculations (Eq.[4]) also predict a gain with increased strain.

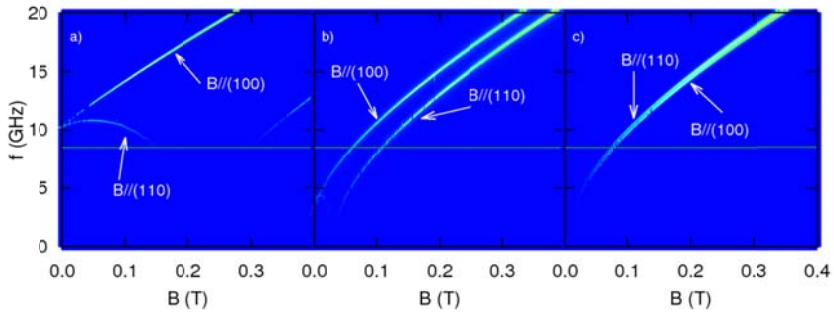

Fig.10. Overlayed FMR maps at two different orientations B//[100], and B//[110], of the 2-layer model for three different model thickness: a) 120 Å, b) 500 Å and c) 1000 Å. Green horizontal line indicates the frequency during the experiments.

For out of-plane rotations, it is the corresponding K^{B}_{2c} parameter that drives the aspect of FMR. The relative intensity of the resonances in different orientations plays an important role. Near the perpendicular directions a second resonance, denoted as $B_0(2)$, also appears. Figure 11 shows the simulated spectra when rotating the field from B//[110] to B//[001]. Initially, the resonance at $B_0(1)$ is more intense, and shifts to higher fields rather slowly as it broadens, exactly as observed [Figs. 5(b) and 6(b)]. This is the result of the "bump" of Fig. 8(e), moving slowly and broadening, when rotating towards the hard axis. In the same process, the sharp and less intense $B_0(2)$ resonance slowly gains intensity as it broadens and can be finally observed near the hard axis. The observation of this resonance (at low enough fields for the spectrometer) is the natural result of the large and negative K^{B}_{2c}. The explanation for the process in which the observed lower field resonance (equivalent to $B_0(1)$) loses, and the higher field resonance (ie. $B_0(2)$) gains, intensity towards the hard axis is as follows. The two branches are separated by the field of reorientation/saturation of the magnetization from in-plane to out-of -plane as indicated in Fig. 8(f)-8(i). In strong in-plane fields the Zeeman-energy, the shape anisotropy and the positive K^{A}_{2c} of the top layer all force the bottom layer (B) oriented in-plane, along its hard axis where it is very sensitive to heterogeneity, given by the highly inhomogeneous $BaTiO_3$ substrate. Thus, the coupled $B_0(1)$ resonance frequency drops below the 8.9 GHz of the experiment, furthermore it also suffers strong inhomogeneous broadening (not captured by our model) and its integrated intensity diminishes rapidly while $B_0(2)$ becomes predominant.

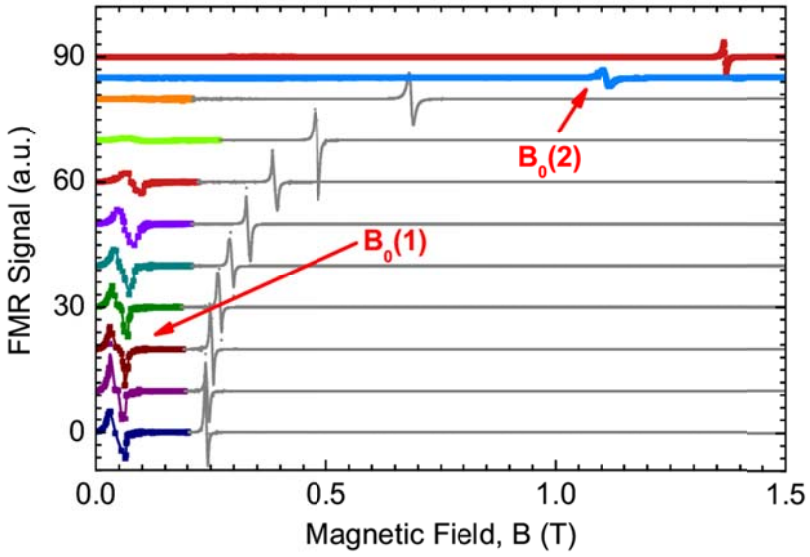

Fig.11. Simulated FMR spectra for the $La_{0.7}Ca_{0.3}MnO_3$//$BaTiO_3$ 150 Å sample in out-of-plane field rotation between B//[110] (0°) and B//[001] (90°).

The strength of the ferromagnetic coupling (J_{eff}) determines the shape of the new FMR modes, through the field where the [001] and [110] mode frequencies tend to zero. Decreasing J_{eff} pushes B_{max} to higher frequencies and also increases modestly the resonance field in the [001] orientation ($B_0(2)$). The actual value of magnetic exchange coupling between Mn spins is hard to determine both experimentally and theoretically [Dagotto2003, Ziese2002, Martin1996, Millis1997]. Nevertheless, it is widely accepted that the effective hopping amplitude between Mn ions must be fractions of an eV (from 1 to 0.2 eV) and the on-site Hubbard repulsion to be ~6 eV [Dagotto2003]. With this, approximating $J_{eff} \sim t^2/U$, the coupling is expected to be between 5 meV and 200 meV. In our model, a relatively broad range of values of the coupling could reproduce the observations, anywhere between -30 and -300 meV per spin-pair, with appropriate choice of the anisotropy constants and the M^B magnetization. Smaller J_{eff} is needed with stronger M^B, as only their product appears in Eq.[5]. Operationally, our choice of the low value of M^B based on PNR leads to the large coupling. In this sense, our J_{eff} must be considered as an effective coupling that accounts for the presence of the much larger out-of-plane moments, not actually included in our model. Physically, even near the interface there are magnetic moments (M^B, seen by PNR) that can be reoriented in-plane with a reasonable applied field. These have a preferred orientation out-of-plane, due to their coupling to moments, with much larger overall magnetization that cannot be reoriented easily.

DISCUSSION

The two-layer model proposed here is in robust agreement with FMR experimental data. The need of high negative anisotropic constants, supported by magnetoelastic theory reveals the strong magnetolastic coupling in $La_{0.7}Ca_{0.3}MnO_3$//$BaTiO_3$. Thus, in line with what was discussed in Chapters 5 and 6, the following picture is proposed: first, $La_{0.7}Ca_{0.3}MnO_3$ may be segregated into an antiferromagnetic phase (AF); second, this AF phase results from high strains and corrugation and is vertically segregated, as PNR results suggest; third, AF clusters may not be uniformly distributed near the interface with $BaTiO_3$ [see Fig. 12(a)] and, fourth, these AF clusters may be at the origin of the high negative anisotropy in $La_{0.7}Ca_{0.3}MnO_3$//$BaTiO_3$. That is, both FM and AF phases must be interspersed within layer B, near the interface (besides, some of these clusters may protrude far into the $La_{0.7}Ca_{0.3}MnO_3$, as seen in PNR profiles) with overall strongly reduced magnetization. When a sufficiently strong magnetic field is applied in plane, the FM phase aligns with it exhibiting a strong magnetic anisotropy as revealed by FMR. This situation is illustrated in Fig. 12(a) and (b). In low applied fields, $\mathbf{M^A}$ lies in-plane. On the other hand, $\mathbf{M^B}$ keeps out-of-plane due to the negative anisotropy induced by AF population.

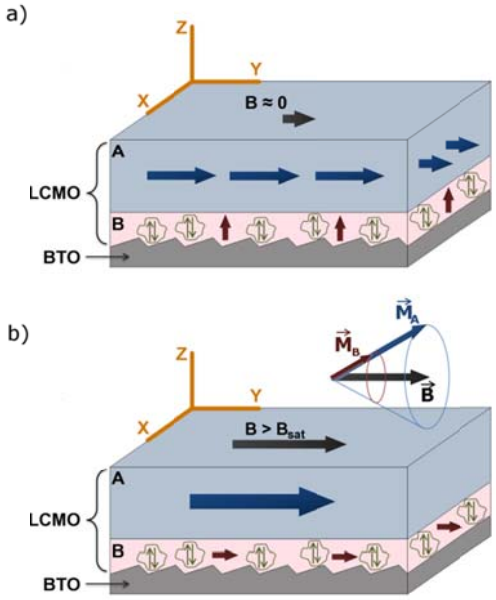

Fig.12. Illustration of the two-layer model. (a) With no applied field, magnetization near the substrate is out-of-plane due to negative anisotropy possibly induced by coupling to AF clusters. b) Under saturating fields M^B turns in-plane.

Although our model does not capture the Matteucci physics, it does provide some insight: the hysteretic behavior between 0.1 and 1 T in Matteucci magnetic loops may have its origin in the magnetic interface between strained and relaxed $La_{0.7}Ca_{0.3}MnO_3$. During the magnetization process with increasing applied field in-plane, $La_{0.7}Ca_{0.3}MnO_3$ magnetization at the grain boundaries rotates out-of-plane. Even in layers as thin as 120 Å, the relative amount of FM and AF populations may vary, since the actual ferroelectric domain configuration is dramatically different amongst unpoled $BaTiO_3$ substrates. We postulate this as the main reason for the big differences observed between thin $La_{0.7}Ca_{0.3}MnO_3$//$BaTiO_3$ films.

CONCLUSIONS

In this chapter, we studied the strong magnetoelastic coupling present in $La_{0.7}Ca_{0.3}MnO_3$//$BaTiO_3$ by means of the joint analysis of PNR and FMR data. We developed a two-layer magnetic model that addresses the relevant differences of $La_{0.7}Ca_{0.3}MnO_3$//$BaTiO_3$ FMR spectra compared to $La_{0.7}Ca_{0.3}MnO_3$//$SrTiO_3$: i) weak and broadened signals; ii) absence of resonance around B//[100]; iii) lower field resonances, $B_0(2)$, near the hard axis; iv) slow shift of FMR to higher field in out-of-plane rotations and, v) lack of resonance for the Matteucci-like samples. Relying on high strains and corrugation near the interface with the $BaTiO_3$ and together with the experimental results from PNR depth profiles, the FMR data are qualitatively explained just by considering a two-layer model. Our findings are compatible with the existence of antiferromagnetic (AF) clusters resulting from the inhomogeneous strain map and corrugation at the $BaTiO_3$/$La_{0.7}Ca_{0.3}MnO_3$ interface. The FM and AF phases must be interspersed near the interface. Besides, some of these clusters may protrude far into the $La_{0.7}Ca_{0.3}MnO_3$, as seen in PNR profiles with overall strongly reduced magnetization. Even in layers as thin as 120 Å, the relative amount of FM and AF populations may vary, as does the $BaTiO_3$ domain distribution.

REFERENCES

[Alberca2011] Alberca, A., et al. "Exotic magnetic anisotropy map in epitaxial La0.7Ca0.3MnO3 films on BaTiO3." Physical Review B 84.13 (2011): 134402.

[Alberca2012] Alberca, A., et al. "Ferroelectric substrate effects on the magnetism, magnetotransport, and electroresistance of La0.7Ca0.3MnO3 thin films on BaTiO3." Physical Review B 86.14 (2012): 144416.

[Alberca2013] A. Alberca et al., "Magnetoelastic coupling in La0.7Ca0.3MnO3/BaTiO3 ultrathin films" submitted to Phys. Rev. B (2013)

[Chang1993] Chang, Ching-Ray. "Magnetostrictive surface anisotropy of epitaxial multilayers." Physical Review B 48.21 (1993): 15817.

[Chikazumi2009] S. Chikazumi, "Physics of Ferromagnetism" 2e., 94. Oxford University Press, USA, (2009)

[Dagotto2003] E. Dagotto, "Nanoscale phase separation and colossal magnetoresistance: the physics of manganites and related compounds". Vol. 136 . Springer, (2003)

[delMoral2008] A. del Moral, "Handbook of Magnetostriction and Magnetostrictive Materials", vol 1, Del Moral Publisher (2008)

[Hoffmann2005] A. Hoffmann, et al.,"Suppressed magnetization in LCMO/YBCO superlattices" Phys. Rev. B 72, R140407, (2005)

[Kittel1996] C. Kittel and P. McEuen, "Introduction to solid state physics" New York: Wiley, 1996.

[Lacheisserie1982] Du Tremolet de Lacheisserie, E., and J. Rouchy. "The magnetoelastic coupling in nickel." Journal of Magnetism and Magnetic Materials 28.1 (1982): 77-87.

[Lacheisserie1993] E. du Tremolet de Lacheisserie. "Magnetostricition: Theory and Applications of Magnetoelasticity" CRC Press 9 Juin 1993 – 408 pages.

[Lacheisserie2006] Du Trémolet de Lacheisserie, Etienne, Damien Gignoux, and Michel Schlenker. "Magnetism." Magnetism, Edited by E. du Trémolet de Lacheisserie, D. Gignoux, and M. Schlenker. ISBN 0-387-23062-9. Berlin: Springer, 2006. 1 (2006).

[Liu2012] Liu, Yaohua, et al. "Effect of Interface-Induced Exchange Fields on Cuprate-Manganite Spin Switches." Physical Review Letters 108.20 (2012): 207205.

[Majkrzak2005] M.R. Fitzsimmons and C.F. Majkrzak, Application of polarized neutron reflectometry to studies of artificially structured magnetic materials, in Modern Techniques for Characterizing Magnetic Materials, ed. by Y. Zhu (Kluwer, Boston 2005), pp. 107-152.

[Martin1996] Martin, Michael C., et al. "Magnetism and structural distortion in the La0.7Sr0.3MnO3 metallic ferromagnet." Physical Review B 53.21 (1996): 14285. [49] [Millis1997] Millis, A. J. "Orbital ordering and superexchange in manganite oxides." Physical Review B 55.10 (1997): 6405.

[Nemes2008] Nemes, Norbert Marcel, et al. "Thickness dependent magnetic anisotropy of ultrathin LCMO epitaxial thin films." Magnetics, IEEE Transactions on 44.11 (2008): 2926-2929.

[O'Donnell1998] O'Donnell, J., et al. "Magnetoelastic coupling and magnetic anisotropy in La0.67Ca0.33MnO3 films." Applied physics letters 72.14 (1998): 1775-1777.

[O'Handley1992] R.C O'Handley & S-W. Sun., J. of Magn.& Magn. Materials, 104, 1717-1720, (1992);

[Park2008] Park, S., et al. "The influence of growth temperature and annealing on the magnetization depth profiles across ferromagnetic/semiconductor interfaces." Journal of Applied Physics 104.8 (2008): 083905-083905.

[Vaz2009] Vaz, Carlos AF, et al. "Magnetic anisotropy modulation of magnetite in FeO/BaTiO (100) epitaxial structures." Applied Physics Letters 94 (2009): 022504.

[Ziese2002] Ziese, Michael. "Extrinsic magnetotransport phenomena in ferromagnetic oxides." Reports on Progress in Physics 65.2 (2002): 143.

CHAPTER 8

MAGNETOELECTRIC COUPLING IN $La_{0.7}Ca_{0.3}MnO_3$//$BaTiO_3$ ULTRA-THIN FILMS

In this chapter, we investigate the magnetoelectric coupling in $La_{0.7}Ca_{0.3}MnO_3$//$BaTiO_3$ thin films. We discuss experiments based on the converse magnetoelectric effect. We report changes in magnetization around 30-40% upon applying electric fields, and estimate magnetoelectric coupling constants, α, of the order of $(2\text{-}5)\cdot10^{-7}$ s/m. This effect is giant compared with those found in literature. Magnetic anisotropy is also highly affected upon applying electric fields, resulting in a considerable reduction of coercive fields.

We compare the magnetoelectric effect in pre-poled and unpoled $BaTiO_3$. The observed behaviour is distinct in the two kinds of substrates and our findings can be explained in terms of differences of domain configuration as described in Chapter 2. The strong magnetoelastic coupling present in $La_{0.7}Ca_{0.3}MnO_3$//$BaTiO_3$ (studied in Chapter 7) is at the origin of this strong magnetoelectric coupling, as the magnetoelectric effect in $La_{0.7}Ca_{0.3}MnO_3$//$BaTiO_3$ is strain mediated.

CHARACTERIZATION

In order to explore the converse magnetoelectric coupling we worked with 100 Å thick $La_{0.7}Ca_{0.3}MnO_3$ films grown on pre-poled $BaTiO_3$ substrates. Essentially, these substrates differ from the unpoled ones, used in the previous chapters of this thesis, by a poling process during fabrication, prior to slicing the large single crystal into individual pieces. We do not refer to poling the actual substrate post-production. See Chapter 3 for more details on these substrates and Chapter 4 for the characterization at room temperature of unpoled $BaTiO_3$.

We chose for these experiments substrates exhibiting mainly "c"-type ferroelectric domains (determined by X-Ray diffraction). That is, in the tetragonal phase, the polar axis (lattice parameter c = 4.036 Å) is directed along the out-of-plane direction, with the shorter parameter, a = 3.992 Å, in-plane.

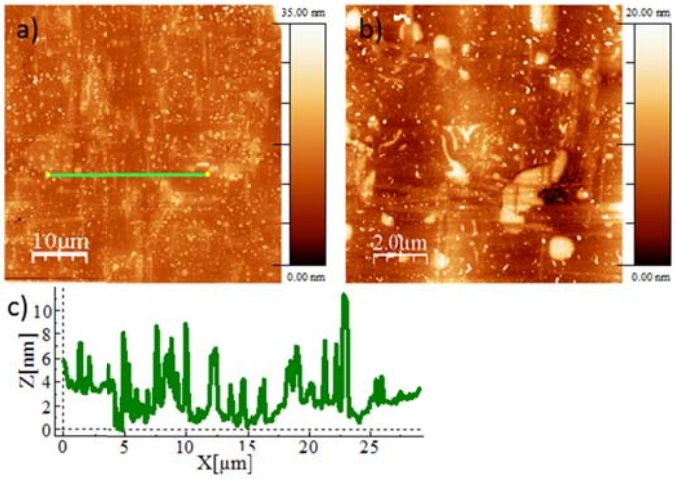

Fig.1. a) and b) AFM images showing the topography of a $BaTiO_3$ substrate used in the inverse magnetoelectric effect experiments. c) Line profile showing the characteristic roughness of these substrates.

The morphology of the $BaTiO_3$ was characterized with AFM prior to film growth. Two representative images are shown in Figure 1, for two different scan areas. Figure 1(a) corresponds to a 50μm x 50μm area, showing a relatively flat surface with features in the 10-15nm range as can be observed in the corresponding profile of Fig. 1(c). The calculated rms for this scan area is 4.8nm. This value is approximately three times lower than the value obtained for unpoled $BaTiO_3$ substrates (Chapter 4), which was dominated by the characteristic corrugation of a-c domain walls. Figure 1(b) shows a 10μm x 10μm scan area. The features observed, with a height of ~10nm, have been ascribed to a selective polishing effect on the different ferroelectric domains.

$La_{0.7}Ca_{0.3}MnO_3$ films grown on pre-poled substrates had a thickness of 100 Å and were characterized by X-Ray diffraction at room temperature. Figure 2 shows two reciprocal space maps of a symmetric (200) and an asymmetric (-103) reflection. $La_{0.7}Ca_{0.3}MnO_3$ thin films are epitaxial with a near cubic structure with parameters in-plane a = 3.88 ± 0.02 Å and, out-of-plane c = 3.86 ± 0.01 Å. The average c/a ratio is ~ 0.99. The relaxation coefficient for this particular sample is R ≈ 0.8, that is, $La_{0.7}Ca_{0.3}MnO_3$//$BaTiO_3$ films are partially relaxed. Coherence lengths are 130±10 Å in-plane and 90±10 Å in the out of plane direction. $La_{0.7}Ca_{0.3}MnO_3$ is under a tensile strain in-plane of ε_{11}=0.5% and out-of-plane ε_{33}=0.1%, approximately.

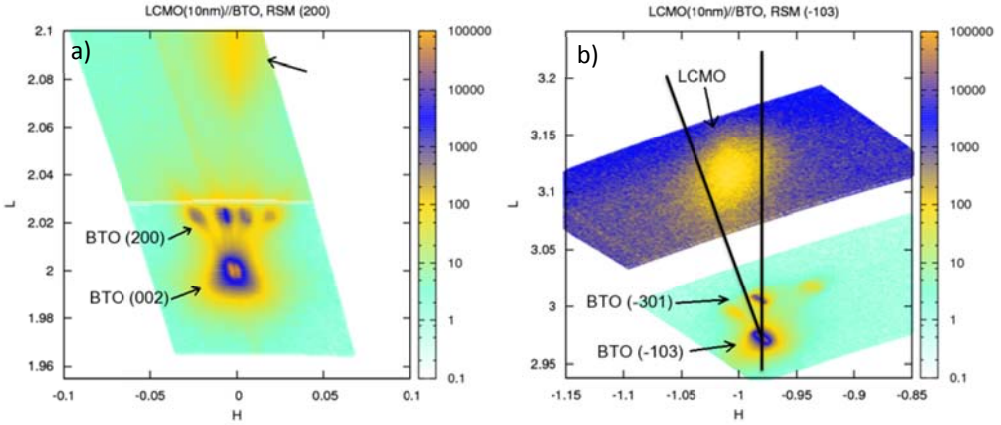

Fig.2. Reciprocal space maps around a) the (200) symmetric direction and b) the (-103) asymmetric reflection. Black lines in b) are guides to the eye.

Magnetic characterization was done using the VSM system. Zero field cooled (ZFC) and field cooled (FC) temperature dependent magnetization is shown in Fig. 3. As for films grown on unpoled $BaTiO_3$ substrates, a broad paramagnetic-ferromagnetic (PM-FM) transition is observed with the characteristic depressed magnetization (saturation magnetization, M_{sat} ≈ 1.8 μ_B/Mn at 20 K, see Fig. 4) and depressed Curie temperature, T_c ≈ 190 K. Large hysteretic behaviour between FC and ZFC measured in an applied field of 100 Oe with elevated blocking (T_B ≈ 140K) and closure (T_{cl} ≈ 155K) temperatures are also observed.

The similarities in magnetism with samples grown on unpoled substrates are evident. Remanent and saturation moments extracted from magnetic hysteresis loops are shown in Fig. 5. Coercive fields are large, up to 500 Oe at low temperatures, denoting the strong magnetic anisotropy and inhomogeneous domains structure (see Fig. 6). Furthermore, the linear temperature dependence of the coercive fields along with the broad PM-FM transition and high blocking temperature indicate that $La_{0.7}Ca_{0.3}MnO_3$ thin films grown on pre-poled $BaTiO_3$ are also magnetic granular systems.

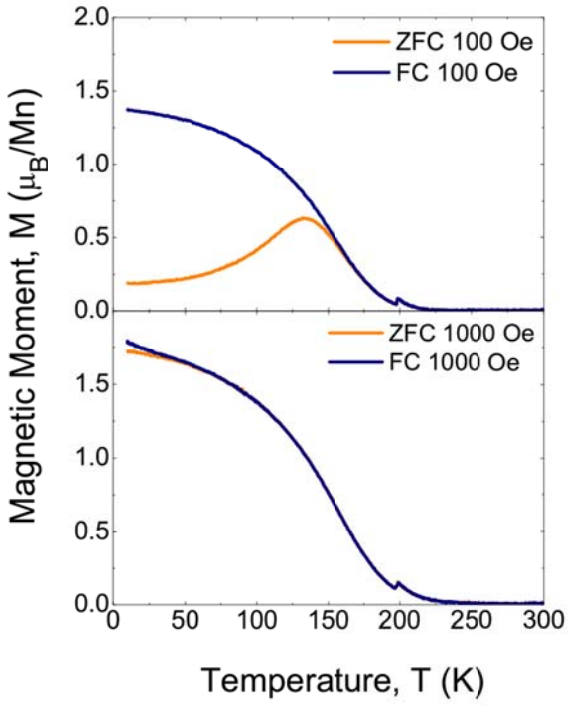

Fig.3. ZFC-FC measured at a) 100 Oe and b) 1000 Oe. The small jump around 190 **K** is due to substrate phase transition from Rhombohedral to Orthorhombic phase.

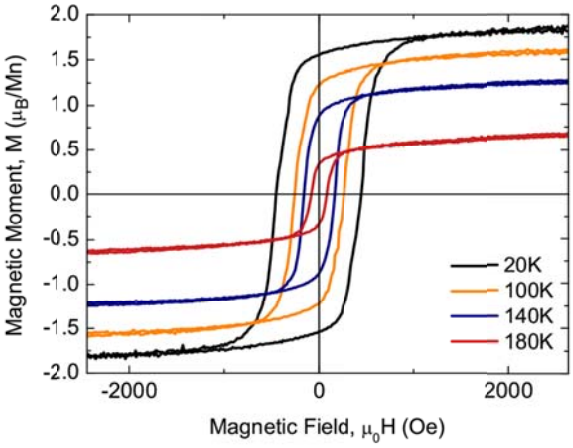

Fig.4. Magnetic hysteresis loops at selected temperatures.

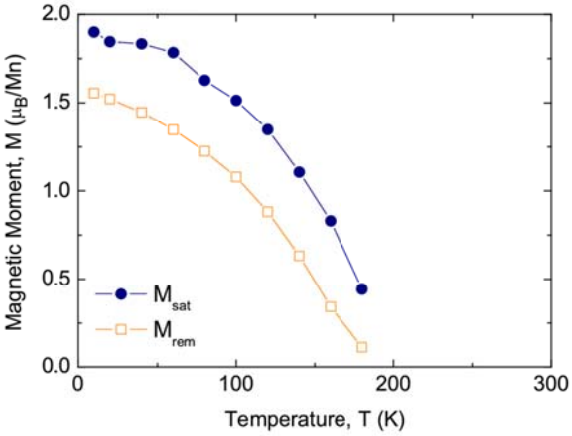

Fig.5. Remanent and saturation moments vs. temperature.

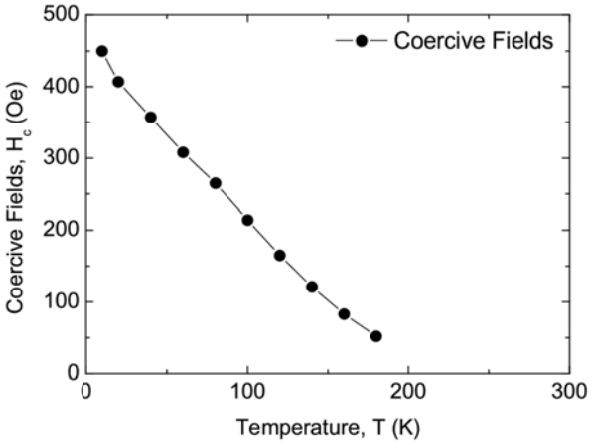

Fig.6. Coercive fields as a function of temperature.

MAGNETOELECTRIC COUPLING TO PRE-POLED $BaTiO_3$ SUBSTRATES

We measured the magnetization changes upon application of electric fields to the ferroelectric substrate. For this purpose we used a modified sample rod for the VSM-PPMS system described in Chapter 3, section VI.

Optimal results were obtained when adopting the following protocol: In the ferroelectric, tetragonal phase (T = 300K) an electric field higher than the ferroelectric coercivity was applied to the sample in a direction normal to the sample surface (E > 1 kV/cm). Direct observation of the current peak at the switching field ensured the sample was properly contacted and that the switching process was taking place. The electric field was then maintained during all subsequent measurements at lower temperatures, essentially keeping the $BaTiO_3$ poled.

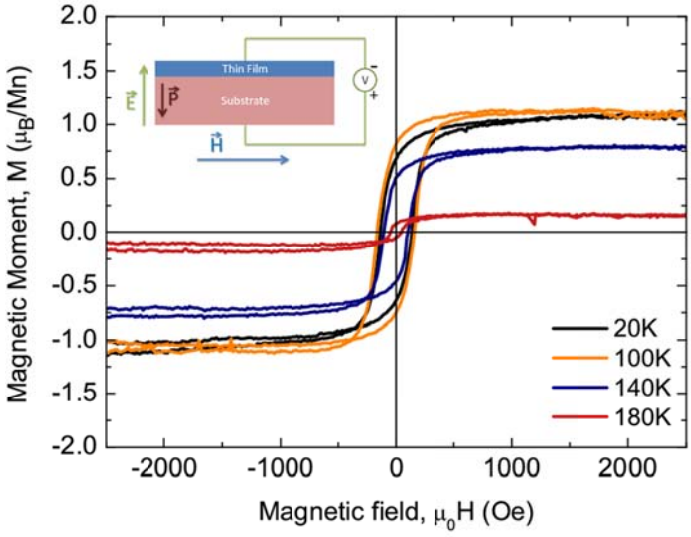

Fig.7. Magnetic hysteresis loops at four selected temperatures measured under an applied voltage of 300 V/mm (ferroelectric polarization points away from sample plane). This figure can be directly compared with Fig. 4, where the magnetic loops of the same sample measured in the initial ferroelectric depolarized state are depicted.

Figure 7 shows the magnetic hysteresis loops of the sample of Fig. 4 with an applied electric field of 3 kV/cm directed towards sample plane, thus inducing a polarization away from it, see inset in Fig. 7. Two remarkable differences can be seen: i) Strong reduction of the saturation moments, $M_{sat} \approx 1.1\ \mu_B$/Mn at 20 K, that is, a variation of a 38%; ii) considerable reduction of the coercive fields, from 450 Oe at 0 kV/cm to 150 Oe at 3 kV/cm, at 20 K.

In Figures 8-10, we compare saturation moments, remanent magnetization and coercive fields in the ferroelectric depolarized (Fig.4) and polarized (Fig. 7) states of the $BaTiO_3$. The effect of electric polarization of the substrate is striking: the magnetization is strongly reduced and this is enhanced at lower temperatures. Furthermore, the magnetization reaches a broad maximum in the polarized state between 50 and 100 K, as opposed to the monotonic behavior in the depolarized one. The coercive field also ceases to grow linearly with decreasing temperature in the polarised state, and instead becomes practically constant below 100 K. This is deeply linked to the change of magnetic anisotropy (change in the shape of magnetic hysteresis loops) due to changes in the ferroelectric substrate and denotes a change in the magnetic granularity of the system below 100K.

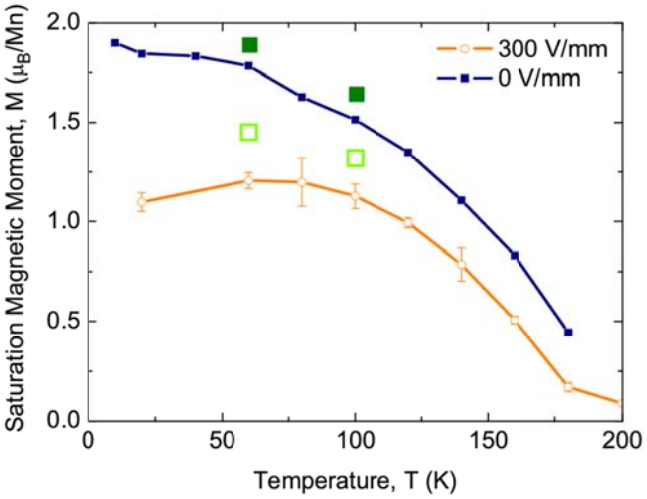

Fig.8. Saturation moments vs. temperature for the same sample at 0 and 3 kV/cm with polarization pointing away from sample plane. Dark green squares correspond to applied electric field and light green open squares to polarization pointing towards sample plane with an applied electric field of 3 kV/cm, from another set of measurements in a different sample.

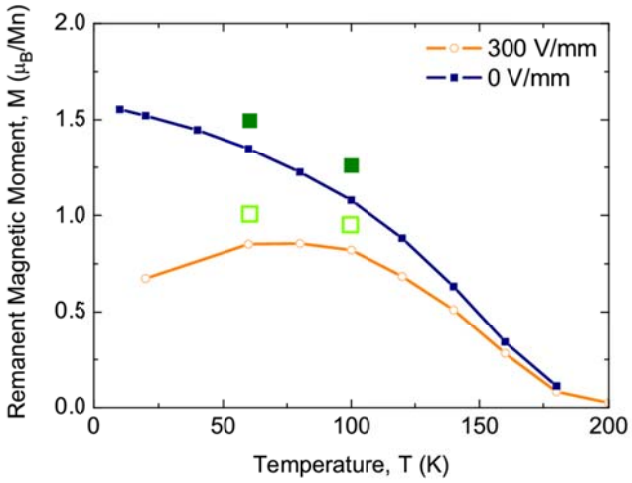

Fig.9. Remanent magnetization versus temperature extracted from magnetic hysteresis loops in Fig. 7.

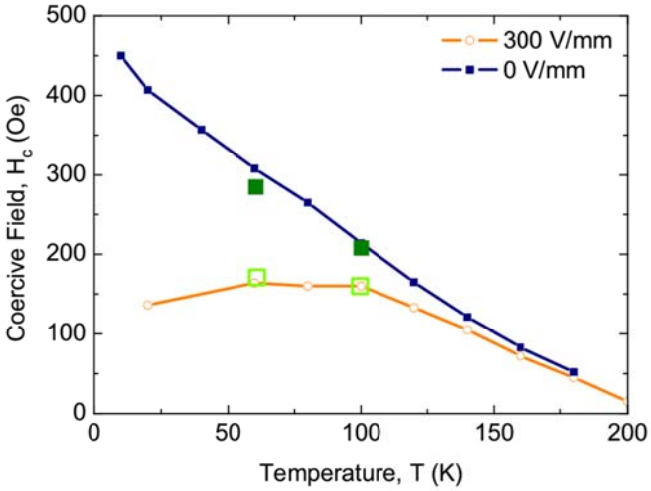

Fig.10. Coercive fields vs. temperature extracted from magnetic hysteresis loops in Fig. 7. Dark and light green points correspond to data obtained from another sample in which the electric field was applied pointing away from sample plane.

The effect of applying the electric field in opposite directions was also studied. Since the magnetoelectric effect is strongly dependent of the substrate history we performed two different experiments. First, in a different sample, the experiment was repeated, this time applying the electric field away from sample plane. This way the effect is comparable in magnitude to that in as prepared samples. Second, in another same sample we measured the effect by applying the electric fields in different directions alternatively. We show the first case in green squares in Figs. 8-10, as extracted from magnetic hysteresis loops and the second case can be appreciated in the moment vs. temperature curves in Fig. 11.
When changing the direction of the applied electric field, the effect was practically the same: a strong reduction of saturation and remanent moments, and coercive fields upon applying saturating electric fields. This is a relevant result since it links the magnetoelectric coupling observed in $La_{0.7}Ca_{0.3}MnO_3$//$BaTiO_3$ to a strain mediated mechanism, instead of interface reconstruction, when differences between different polarization senses are expected [Burton2009, Dagotto2011, Sohrab2012] We will discuss this later in this chapter.

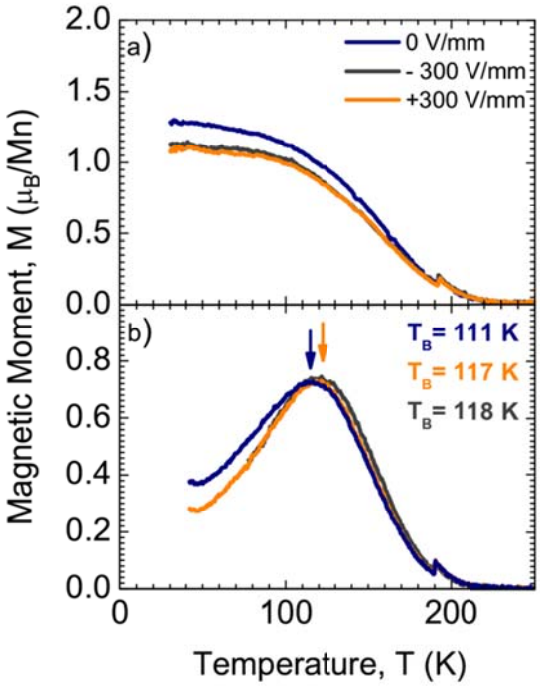

Fig.11. ZFC measured at a) 1000 Oe and b) 100 Oe. Blue lines correspond to the depolarized state of the ferroelectric. Orange and gray correspond to applied electric fields pointing towards (+300 V/mm) and away from (-300 V/mm) sample plane. Note the different y-scales in both graphs.

In Fig. 11, we compare ZFC measurements with different polarization states of the substrate (same sample). Some works reported in literature state that the Curie temperature in FM/FE heterostructures may shift when applying electric fields the substrate (up to 20K in Refs. [Thiele2007, Hajo2009]). However, we did not observed any change in the T_c due to the broad nature of the PM-FM transition and the coincidence of the T_c with the $BaTiO_3$ phase transition (Fig. 12.a). Indeed, even after taking the derivative of the ZFC, no conclusive change in the Curie temperature was observed. Nevertheless, we were able to measure a shift of 5K in the Blocking temperature in $La_{0.7}Ca_{0.3}MnO_3$//$BaTiO_3$ heterostructures (Fig. 12.b).

From changes in saturation moments, ΔM = M(0kV/cm)-M(3kV/cm) we can calculate the linear magnetoeleastic coupling constant as a function of temperature:

$$\alpha = \mu_0 \frac{\Delta M}{\Delta E} \qquad [1]$$

resulting in a maximum magnetoelectric constant at low temperatures of $\alpha = 5 \cdot 10^{-7}$ s/m, as depicted in Figure 12. We also include the calculated coupling constants (green squares of Figs. 8-10) of the second sample.

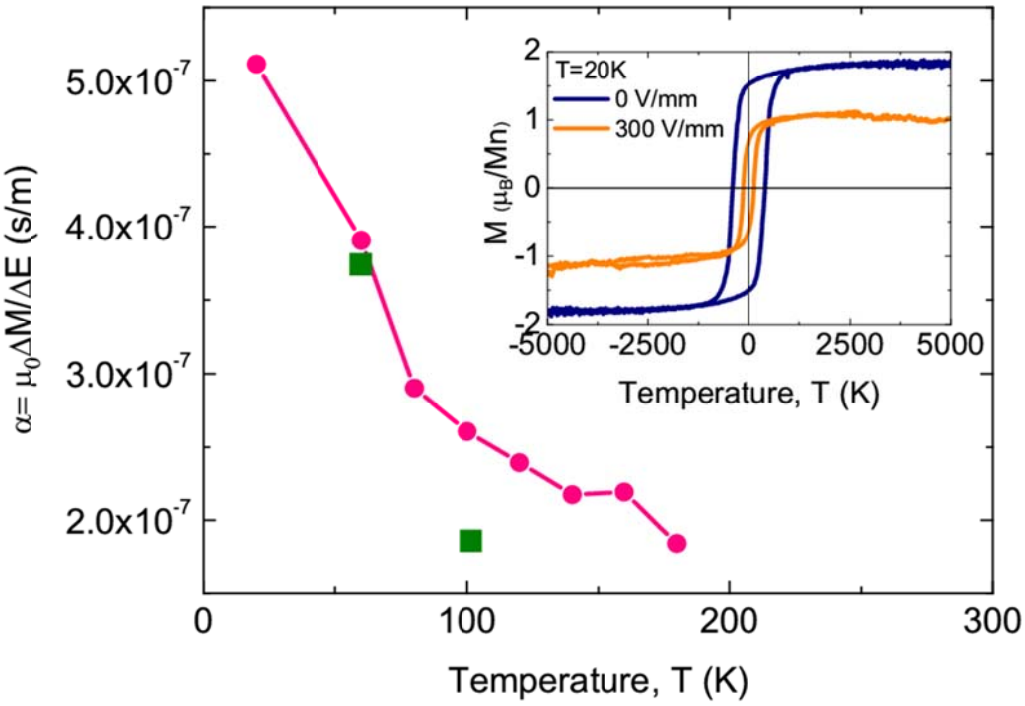

Fig.12. Calculated magnetoelectric coupling constant according to Eq. [1]. ΔM is the difference between saturation moments with applied electric fields of 0 and 3 kV/cm. Green squares correspond to the calculated values for another sample in which the same electric field was applied in the opposite sense. Inset: Magnetic hysteresis loops at 20 K with no applied electric field (initial ferroelectric depolarized state) and 3 kV/cm.

MAGNETOELECTRIC COUPLING IN CASE OF UNPOLED $BaTiO_3$ SUBSTRATES

The scenario observed in $La_{0.7}Ca_{0.3}MnO_3$ thin films grown on unpoled $BaTiO_3$ substrates is completely different upon applying an electric field to the substrate. Although we do observe a magnetoelectric effect, it is one order of magnitude weaker ($\alpha \approx 5 \cdot 10^{-8}$ s/m) compared to films grown on pre-poled substrates. Figure 13 shows α as a function of temperature calculated from two samples, in various magnetic fields (as indicated).

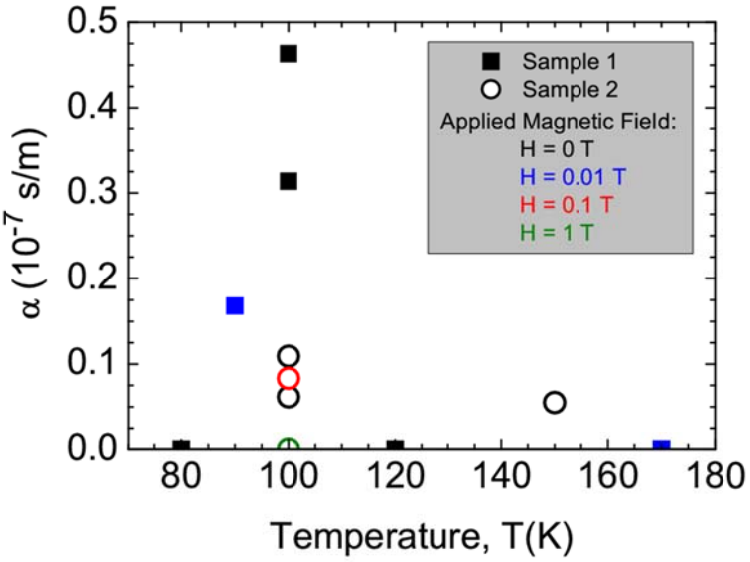

Fig.13. Magnetoelectric coupling constant vs. temperature for two equivalents $La_{0.7}Ca_{0.3}MnO_3$//$BaTiO_3$ (unpoled) samples. Different colors indicate different applied magnetic fields, as indicated.

The remarkable difference with the samples grown on poled substrates, is the dependence with temperature and applied magnetic fields: no magnetoelectric effect (i.e. $\alpha < 10^{-9}$ s/m) was observed in these samples at temperatures below 80 K or at magnetic fields higher than 0.1 T. It was, in fact, impossible to observe magnetoelectric coupling while measuring magnetic hysteresis loops or magnetization vs. temperature curves (in contrast with our thin films grown on poled substrates), and a procedure established in Ref. [Eerenstein2007] was followed instead. First, the sample was cooled in a small (or zero) magnetic field. Then, magnetic moment versus time was recorded: at a certain time, t_0, an electric field higher than the coercive field of the substrate was applied suddenly (typically, 1-3 kV/cm) and a "jump" in the magnetization was observed. This jump was always sharp and persistent and implied a reduction of the magnetization. Figure 14 shows an example of this process.

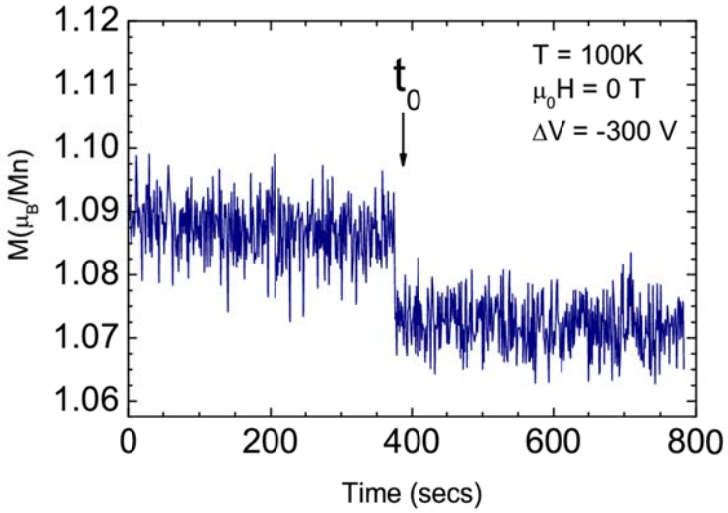

Fig.14. Magnetic moment vs. time, after field cooling in 0.1T, and in magnetic remanence. t_0 indicates the time in which an electric field of 300 V/mm (pointing away of the thin film) is applied to the ferroelectric substrate resulting in a decrease in magnetization (magnetoelectric effect).

In addition, the change in magnetic moments upon applied electric fields was only observed in a limited sequence of "switching" events (typically, less than 5) as ΔM quickly reduced when consecutively applying the same electric field, until no effect was indeed observed. Nevertheless, the effect was persistent and "turning off" the electric field usually resulted in a recovery of the previous magnetic state. Several attempts to recover the initial state of the sample, and therefore, the possibility of observing the magnetoelectric effect again, were investigated (as, for example, depolarizing electrically and magnetically the samples at room temperature or heating the substrates over the ferroelectric Curie temperature in O_2 atmosphere), to no avail.

DISCUSSION

$BaTiO_3$ QUALITY

The differences presented in this chapter between thin films grown on unpoled and poled substrates can be understood in terms of the substrate nature.

In Chapter 2 we considered the effects of domain configuration on the piezoelectric response of $BaTiO_3$. In general, three contributions are expected: intrinsic contribution, domain rotation, and polarization rotation. Particularly relevant is the fact that $BaTiO_3$ substrates exhibit enhanced piezoelectric effects when the electric field is applied in directions different than the polar axis [Fu2000b, Fu2000, Budimir2005, Damjanovic2006]. However, this effect is observed in coarse grained or engineered states of $BaTiO_3$ single crystals where the dominant mechanism that contributes to piezoelectricity is polarization rotation [Park1997].
In fact, the piezoelectric strains expected in the case of fine grained substrates, (such as our unpoled $BaTiO_3$ substrates) in the rhombohedral phase are small (<<1%) compared with those in the tetragonal phase (when ferroelectric domains are rotated from a "a"-type domains to a "c"-type domains the strain changes a 1%). In this sense, although unpoled $BaTiO_3$ can be used in room temperature heterostructures [Eerenstein2007], in order to enhance the piezoelectric effect and, consequently, the magnetoelectric effect in the heterostructure, high substrate homogeneity, as in pre-poled substrates, is required.

It is worth noticing that although high piezoelectric strains are expected to be at the origin of the enhanced magnetoelectric effect observed in $La_{0.7}Ca_{0.3}MnO_3$ on poled $BaTiO_3$, the actual path followed by the polarization vector in the rhombohedral phase is unknown as the calculations usually do not involve changes in temperature (see, for instance, Ref. [Fu2000b]), thus, the values of these piezoelectric strains in $BaTiO_3$ substrates are unknown.

MAGNETOELECTRIC COUPLING MECHANISM

Let us now discuss the possible processes that lead to magnetization reduction upon applying electric fields to the ferroelectric substrate. The mechanisms that allow magnetoelectric coupling (described in Chapter 1) are, basically: polarization (charge accumulation/depletion at the interface) and structural (phase separation mediated by strain) mechanisms [Velev2011].

A relevant aspect that allows us to discern between polarization and structural mechanisms is the "symmetric" nature of the magnetoelectric effect in $La_{0.7}Ca_{0.3}MnO_3$//$BaTiO_3$: we observed exactly the same effect when polarizing the substrate with polarization vector pointing towards the thin film or away from it. Then, if we hypothetically consider the magnetoelectric effect discussed here as a polarization effect, either poling with

holes or electrons has the same consequence on the magnetic thin film, which is in disagreement with all proposed mechanisms of this type [Hajo2009]. Therefore, the magnetoelectric effect (see below) in $La_{0.7}Ca_{0.3}MnO_3$//$BaTiO_3$ is largely dominated by structural changes.

For example, a shift in the manganite phase diagram can only be understood if the effect favours FM ordering when increasing the doping level x (for small changes in x), and the AF ordering when decreasing x (see $La_{1-x}Ca_xMnO_3$ phase diagram in Chapter 2). Note, that an increase in x would imply an increase in the T_c and a reduction of the magnetization –given by $(4-x)\mu_B$– and *vice versa*. Then, a change in the doping level induced by charge depletion fails to explain the magnetoelectric effect observed in $La_{0.7}Ca_{0.3}MnO_3$//$BaTiO_3$. Other possibilities, like Ca segregation near the interface would *only* favour the antiferromagnetic ordering in accumulation, and for the same reason are ruled out [Hajo2009].
Moreover, changes in carrier density would favour non-parallel spin arrangement [Burton2009, Dagotto2011, Sohrab2012] by inducing deformation in the Mn octahedra, but the calculated phase diagrams show a preference for AF only in one of the polarization states of the ferroelectric. Besides, these effects require high interface quality and, generally, only involve a few unit cells near the ferroelectric (with magnetic modulations of ~10% [Lu2012]).

Hence, only structural deformations are left to explain the giant magnetoelectric effect observed in $La_{0.7}Ca_{0.3}MnO_3$//$BaTiO_3$. To address this mechanism, we rely on the strain-driven phase separation in $La_{0.7}Ca_{0.3}MnO_3$ as the most plausible explanation (as we already did in Chapters 5 and 6). The ingredients that lead to strong magnetoelastic coupling in $La_{0.7}Ca_{0.3}MnO_3$//$BaTiO_3$ are large and inhomogeneous strains induced by lattice mismatch and corrugation. These result in the coexistence of two magnetic phases in the thin film in the depolarized state of the substrate. One phase is metallic, ferromagnetic and behaves as expected for low tensile strains; the other one is insulating, antiferromagnetic and is highly affected by strain. These phases are vertically segregated and distributed in patches near the interface. When electric fields are applied to $BaTiO_3$ the strain distribution drastically changes, modifying the sensitive structural distortions present in the $La_{0.7}Ca_{0.3}MnO_3$ and enhancing/favouring the AF phase. Presumably, corrugation is smoothed by the electric fields leading to a more uniformly distributed FM and AF phases that would lead to reduced anisotropy in the system.

MAGNETIC ANISOTROPY

The changes in the magnetic anisotropy and magnetic granularity of the thin film give a positive insight to the picture considered above. First, the behaviour observed in $La_{0.7}Ca_{0.3}MnO_3$ grown on pre-poled $BaTiO_3$ when no electric fields are applied, is similar to that observed in samples grown on unpoled $BaTiO_3$: linear dependence with coercive fields (Fig. 6) and high blocking and closure temperatures (Fig. 3). As we showed in Chapter 7, the magnetic anisotropy can be seen in those samples as a footprint of the coexistence of AF and FM clusters near the interface. Nevertheless, when the electric fields are applied this behaviour changes drastically and at all temperatures we observe a noticeable reduction of coercive fields and saturation moments (see inset in Fig. 12). Below 100K, the granular character of these systems is lessened and the whole thin film behaves similarly to a less strained, homogeneous and thinner layer, suggesting a higher concentration of AF clusters near the $BaTiO_3$ and clusters more uniformly distributed.
Also, in line with previous considerations in Chapters 5 and 6, this reduced anisotropy is consistent with the less corrugated interface. This idea comes from the enhanced piezoelectric effect expected in these substrates with a rotation of the polarization vector from the [111] rhombohedral diagonal to the [100] parallel to the electric field (the in plane parameter of the $BaTiO_3$ may be reduced, and thus the strain induced in the thin film). In this sense, a future study of the topography at low temperature of these substrates with applied electrics fields seems to be in order.

CONCLUSIONS

In this chapter, we demonstrated strong magnetoelectric coupling in $La_{0.7}Ca_{0.3}MnO_3$//$BaTiO_3$ ultra-thin films. This coupling is strain mediated and even in partially relaxed thin films can be appreciated. However, as our study with different substrates has shown, magnetoelectric coupling is highly affected by the substrate nature. In fact, $La_{0.7}Ca_{0.3}MnO_3$ grown on unpoled substrates with generally small size grains systematically exhibited weak magnetoelectric coupling constant and low reproducibility. On the other hand, thin films grown on poled substrates with mainly "c"-type ferroelectric domains and high quality (coarse grains), exhibited high magnetoelectric coupling at all temperatures measured. The strong magnetoelectric coupling in these samples can only be understood as the effect of polarization rotation from the [111] direction to the [100] (parallel to the applied electric field) and the consequent large strain involved. One relevant aspect of this coupling is the effect of ferroelectric polarization in the thin film magnetic anisotropy, with reduced coercive fields. In addition, the magnetic granularity, observed in all $La_{0.7}Ca_{0.3}MnO_3$//$BaTiO_3$, is affected by the electric fields as the blocking temperature is shifted by 5K and the linear dependence with temperature of the coercive fields is broken below 100K.

In conclusion, magnetoelectric coupling is possible in $La_{0.7}Ca_{0.3}MnO_3$//$BaTiO_3$ mediated by the strong magnetoelastic coupling between thin film and substrate in high quality substrates where polarization rotation yields large piezoelectric strains.

REFERENCES

[Alberca2011] Alberca, A., et al. "Exotic magnetic anisotropy map in epitaxial La0.7Ca0.3MnO3 films on BaTiO3." Physical Review B 84.13 (2011): 134402.

[Alberca2012] Alberca, A., et al. "Ferroelectric substrate effects on the magnetism, magnetotransport, and electroresistance of La0.7Ca0.3MnO3 thin films on BaTiO3." Physical Review B 86.14 (2012): 144416.

[Alberca2013] A. Alberca et al., "Magnetoelastic coupling in La0.7Ca0.3MnO3/BaTiO3 ultrathin films" submitted to Phys. Rev. B (2013)

[Budimir2005] Budimir, Marko, Dragan Damjanovic, and Nava Setter. "Enhancement of the piezoelectric response of tetragonal perovskite single crystals by uniaxial stress applied along the polar axis: A free-energy approach." Physical Review B 72.6 (2005): 064107.

[Burton2009] Burton, John D., and Evgeny Y. Tsymbal. "Prediction of electrically induced magnetic reconstruction at the manganite/ferroelectric interface." Physical Review B 80.17 (2009): 174406.

[Dagotto2011] Dong, Shuai, et al. "Microscopic model for the ferroelectric field effect in oxide heterostructures." Physical Review B 84.15 (2011): 155117.

[Damjanovic2006] Damjanovic, D., et al. "Piezoelectric anisotropy: Enhanced piezoelectric response along nonpolar directions in perovskite crystals." Journal of materials science 41.1 (2006): 65-76.

[Eerenstein2007] Eerenstein, W., et al. "Giant sharp and persistent converse magnetoelectric effects in multiferroic epitaxial heterostructures." Nature materials 6.5 (2007): 348-351.

[Fu2000] Fu, Huaxiang, and Ronald E. Cohen. "Polarization rotation mechanism for ultrahigh electromechanical response in single-crystal piezoelectrics." Nature 403.6767 (2000): 281-283.

[Fu2000b] Fu, Huaxiang, and R. E. Cohen. "Piezoelectric response from rotating polarization." AIP Conference Proceedings. Vol. 535. (2000)

[Hajo2009] Molegraaf, Hajo JA, et al. "Magnetoelectric effects in complex oxides with competing ground states." Advanced Materials 21.34 (2009): 3470-3474.

[Lu2012] Lu, H., et al. "Electric modulation of magnetization at the BaTiO3/La0.67 Sr0.33MnO3 interfaces." Applied Physics Letters 100.23 (2012): 232904-232904.

[Park1997] Park, Seung-Eek, and Thomas R. Shrout. "Ultrahigh strain and piezoelectric behavior in relaxor based ferroelectric single crystals." Journal of Applied Physics 82 (1997): 1804.

[Sohrab2012] Chen, Hanghui, and Sohrab Ismail-Beigi. "Ferroelectric control of magnetization in La_ {1− x} Sr_ {x} MnO_ {3} manganites: A first-principles study." Physical Review B 86.2 (2012): 024433.

[Thiele2007] Thiele, C., et al. "Influence of strain on the magnetization and magnetoelectric effect in La_{0.7}A_{0.3}MnO_{3}/ PMN-PT (001)(A= Sr, Ca)." Physical Review B 75.5 (2007): 054408.

[Velev2011] Velev, J. P., S. S. Jaswal, and E. Y. Tsymbal. "Multi-ferroic and magnetoelectric materials and interfaces." Philosophical Transactions of the Royal Society A: Mathematical, Physical and Engineering Sciences 369.1948 (2011): 3069-3097.

CHAPTER 9
SUMMARY AND FUTURE

In this thesis we have studied the interfacial effects appearing in $La_{0.7}Ca_{0.3}MnO_3$//$BaTiO_3$ multiferroic heterostructures. These systems exhibit exotic magnetic and transport properties and can be described as a vertically segregated structure with coexistence of two $La_{0.7}Ca_{0.3}MnO_3$ magnetic phases. The key to understand this phenomenology is the strong magnetoelastic coupling between thin film and substrate that arises from high inhomogeneous strain and corrugation.

We observed giant magnetoelectric coupling between the magnetic thin film and ferroelectric substrate, resulting from strain effects (magnetoelastic effect). The large value of the magnetoelectric coupling constant obtained in thin films can only be understood in terms of the high strains that may result from a ferroelectric polarization rotation in the high-quality $BaTiO_3$ substrates.

Below, we summarized these conclusions and propose future experiments.

GENERAL PROPERTIES OF $La_{0.7}Ca_{0.3}MnO_3$//$BaTiO_3$

$BaTiO_3$ substrates have a complex surface with a typical roughness of 40 Å, corrugation angles varying from 0.27º in the rhombohedral phase to 0.6º in the tetragonal phase, and with ferroelectric domain patterns that change with thermal and electric history. In addition, the lattice parameter misfit between thin film and substrate is over 3%, resulting in partially relaxed thin films (Chapter 4) with inhomogeneous strain distribution. The $BaTiO_3$ corrugation is enormous compared with the non-ferroelectric $SrTiO_3$ that has a typical roughness of only 4-9 Å and small lattice parameter misfit (less than 1%) with $La_{0.7}Ca_{0.3}MnO_3$. The latter system was taken as the reference.

The structural and morphological characteristics of $BaTiO_3$ lead to the enhancement of interfacial effects in ultra-thin films of $La_{0.7}Ca_{0.3}MnO_3$//$BaTiO_3$ (with thicknesses below 120 Å) that involve approximately the 30-40% of the $La_{0.7}Ca_{0.3}MnO_3$ film.

$La_{0.7}Ca_{0.3}MnO_3$//$BaTiO_3$ exhibit depressed saturation moments, broad paramagnetic-ferromagnetic transitions, high coercive fields with linear temperature dependence and elevated blocking temperatures. Furthermore, Matteucci magnetic hysteresis loops have been observed between 40 K and 150 K indicating two relevant aspects: 1) an important fraction of the ”missing”, non-ferromagnetic, moments participate actively in the overall properties of $La_{0.7}Ca_{0.3}MnO_3$ thin films, and 2) large magnetoelastic energy (due to high strains) is at the origin of these anomalies (Chapter 5). Consistently, large magnetoresistance and electroresistance and an atypical second percolative metal-insulator transition appear in the same temperature interval, indicating the coexistence of two $La_{0.7}Ca_{0.3}MnO_3$ magnetic phases (Chapter 6).

MAGNETOELASTIC COUPLING

The study of the strong magnetoelastic coupling in $La_{0.7}Ca_{0.3}MnO_3$//$BaTiO_3$ was done using Polarized Neutron Reflectometry (PNR) and Ferromagnetic Resonance (FMR) techniques supported with magnetic anisotropy theory (Chapter 7), which in $La_{0.7}Ca_{0.3}MnO_3$//$BaTiO_3$ predicts high magnetoelastic energies.

The analysis of FMR in terms of magnetic anisotropy energy densities allowed us to link the complex spectra and the large negative anisotropy observed to magnetoelastic coupling. We used a basic model of two layers with different anisotropy constants. One layer is considered relaxed (low strains) with anisotropy coefficients similar to those in $La_{0.7}Ca_{0.3}MnO_3$//$SrTiO_3$. The second accounts for the $La_{0.7}Ca_{0.3}MnO_3$ highly affected by strain near the interface. Using this vertically segregated structure with thickness obtained from the PNR analysis, we simulated the FMR spectra and estimated the various magnetoelastic anisotropy constants.

The success of this manageable model to explain the FMR spectra is interpreted as a confirmation of the strong magnetoelastic coupling between thin film and substrate. In addition, magnetoelastic coupling may be at the origin of the second magnetic phase suggested in Chapters 5 and 6 which is also favored by $La_{0.7}Ca_{0.3}MnO_3$ tendency to phase separation. Although, the direct observation of the second magnetic phase was not possible, the antiferromagnetic ordering near the interface is most likely at the origin of the high negative anisotropy observed in FMR and explains the high resistance observed at low temperatures. Matteucci magnetic loops can result from the interaction between these two magnetic phases in a magnetostrictive process and may involve spins in the magnetic interface between FM and AF moments.

MAGNETOELECTRIC COUPLING

We observed magnetoelectric coupling in $La_{0.7}Ca_{0.3}MnO_3$//$BaTiO_3$ heterostructures with magnetoelectric coupling constant α, on the order of $(2\text{-}5)\cdot10^{-7}$ s/m (Chapter 8). This coupling affects nearly 50% of magnetic moments at low temperatures. Two factors determine the magnitude of this effect: 1) the change in strain between thin film and substrate and 2) substrate nature. In $BaTiO_3$, these two factors are related. When using pre-poled substrates with mainly "c"-type domains higher magnetoelectric coupling constants were measured and the effect was more reproducible (since these substrates are generally of better quality and have larger ferroelectric domains). In addition, by keeping the electric field applied while cooling into the rhombohedral phase this almost "single domain" state was preserved, thus favouring the polarization rotation mechanism over domain rotation. This switching process may involve strains exceeding 1%, explaining the magnitude of the magnetoelectric effect. The effect is systematically smaller in samples grown on unpoled substrates. Again, the explanation for such weak effects comes from the substrate nature: unpoled substrates are fine grained and the switching process is dominated by domain rotation and the intrinsic piezoelectric effect, resulting in smaller piezo-strains.

In conclusion, the magnetoelectric effect in $La_{0.7}Ca_{0.3}MnO_3$//$BaTiO_3$ is strain mediated and the magnitude of the effect depends of the magnitude of the strains involved. The magnetoelectric effect in $La_{0.7}Ca_{0.3}MnO_3$//$BaTiO_3$ can be enhanced by using high quality pre-poled substrates by virtue of the increased piezoelectric effect for applied electric fields in directions other than the spontaneous polarization direction.

FUTURE

In this Thesis, we have studied the simplest nanostructured combination of two prototypical materials, that is thin layers of optimally doped manganite $La_{0.7}Ca_{0.3}MnO_3$ and bulk ferroelectric $BaTiO_3$ crystals, with a view to enhance interfacial effects. A rich, hitherto unreported, phenomenology has been unveiled and we have shown that this combination of materials offers excellent possibilities for the study of the underlying physics of the

manganite/ferroelectric interface and of the phase segregation-prone manganite films under high strains. In fact, one of the most relevant results of this thesis is the enhancement of interfacial effects arising from lattice mismatch and highly strained thin films caused by the substrate.

As a result of the contribution presented in this Thesis, some directions for the future work in this field can be formulated:

1) From the point of view of achieving real-world applications, the systematic study of ultra-thin films of manganites of different composition which remain ferromagnetic at room temperature is an obvious route.

2) Developing thermal and electric field cycles in order to control the domain pattern in the ferroelectric substrate ("the engineering of ferroelectric domains") is a requirement of importance from both the fundamental and the applied points of view. To a large extent, miniaturization techniques can alleviate this problem by selecting specific sample areas with a uniform electrical polarization but currently an extensive suite of experimental characterization techniques cannot yet be implemented at the micron or sub-micron scale. With bulk substrates, larger domain widths are expected than with thin ferroelectric films (the latter are prone to exhibiting large leakage currents).

3) Alternatively to 2), the thin ferroelectric film route should be pursued by studying bilayered heterostructures of the types $La_{0.7}Ca_{0.3}MnO_3/BaTiO_3//SrTiO_3$ or $BaTiO_3/La_{0.7}Ca_{0.3}MnO_3//SrTiO_3$ combined with nanopattering techniques on the ferroelectric film that may induce inhomogeneous strain in the manganite and, therefore, give rise to enhanced interfacial effects.

RESUMEN EN ESPAÑOL

Una de las aplicaciones más interesantes de la espintrónica es el desarrollo de nuevas arquitecturas para la mejora de memorias de tipo RAM (del inglés, *Random Access Memory*). Hoy en día, este problema se aborda utilizando, entre otros métodos, campos eléctricos con el propósito de modificar el ordenamiento magnético, permitiendo así escribir datos eléctricamente y leerlos magnéticamente en un bit multiferroico. Esto se puede conseguir, por ejemplo, modificando la anisotropía magnética de sistemas basados en estructuras de Fe o explotando la interacción entre órdenes ferroicos acoplados en heteroestructuras multiferroicas basadas en óxidos. La ventaja de este método, comparado con los utilizados para otras RAM es la reducción considerable de consumo energético en el proceso de polarización magnética, a lo que hay que añadir el hecho de que el carácter no-local de los campos magnéticos utilizados en otros dispositivos puede afectar a los bits de memoria circundantes, con lo que el uso de campos eléctricos (generados con voltajes locales) se convierte en una ventaja.

Una de las arquitecturas más prometedoras que se pretende alcanzar es la de las memorias de cuatro estados lógicos. En este tipo de memorias, sería posible codificar la información cuaternaria en un dispositivo donde los órdenes ferroeléctrico y ferromagnético estuvieran acoplados. En estos dispositivos, se obtienen cuatro estados de resistencia combinando el alineamiento paralelo y anti-paralelo de las láminas magnéticas de una MTJ (del inglés *Magnetic Tunnel Junction*) y los dos posibles estados de polarización ferroeléctrica de la barrera (véase Capítulo 1).

Con esta motivación en mente, en esta tesis hemos estudiado un tipo particular de heteroestructura multiferroica que consiste en una lámina ferromagnética de manganita ($La_{0.7}Ca_{0.3}MnO_3$) crecida sobre sustratos de $BaTiO_3$ ferroeléctrico. La elección de estos materiales está motivada por sus propiedades intrínsecas. Esta manganita en el dopaje óptimo es un sistema fuertemente correlacionado, muy conocido por exhibir magnetoresistencia colosal (CMR), además de una fuerte tendencia a la segregación de fases, lo que la hace susceptible de ser fuertemente afectada por polarización y *strain*s (deformaciones) debidos al sustrato. Por otro lado, el sustrato de $BaTiO_3$ es uno de los ferroeléctricos más estudiados de la clase de perovskita.

Uno de los objetivos más importantes de esta tesis es explorar los efectos interfaciales que aparecen en láminas ultradelgadas de este tipo y que tienen su origen en la interacción entre órdenes ferroeléctrico y ferromagnético en la discontinuidad entre lámina y sustrato. Nuestro otro objetivo es el estudio del efecto magnetoeléctrico en este sistema, modificando la fase magnética cambiando el estado de polarización del sustrato al aplicar voltajes (efecto magnetoeléctrico inverso). Los resultados mostrados a lo largo de esta tesis revelan nueva e inesperada física que está relacionada, en última instancia, con el fuerte acoplo magnetoelástico entre sustrato y lámina delgada. Este acoplo magnetoelástico es también responsable del acoplo magnetoeléctrico observado en estos sistemas.

PROPIEDADES GENERALES DE $La_{0.7}Ca_{0.3}MnO_3//BaTiO_3$

El sustrato de $BaTiO_3$ muestra una superficie compleja con, típicamente, rugosidades de 40 Å, ángulos de corrugación que varían de 0.27º en la fase romboédrica a 0.6º en la fase tetragonal, y una configuración de dominios ferroeléctricos que cambia varía debido a la aplicación de ciclados térmicos y eléctricos. Además, la diferencia entre el parámetro de la celda unidad de la lámina delgada y el sustrato es mayor del 3 %, lo que en

general resulta en láminas parcialmente relajadas (Capítulo 4) con una distribución inhomogénea de *strain*. La corrugación del $BaTiO_3$ es enorme si se compara con sustratos no ferroeléctricos como el $SrTiO_3$ que también tienen una estructura de *perovskita* y parámetro de celda unidad similar. Los sustratos de $SrTiO_3$ exhiben una rugosidad media de 4-9 Å y menor diferencia entre parámetros con la manganita (menos del 1%). En esta tesis utilizamos láminas de $La_{0.7}Ca_{0.3}MnO_3$ crecidas sobre estos sustratos como sistema de referencia.

La principal consecuencia de las características estructurales del $BaTiO_3$ es el aumento de lo que se puede considerar efectos interfaciales en láminas ultra delgadas y que en $La_{0.7}Ca_{0.3}MnO_3$//$BaTiO_3$ (con grosores menores que 120Å) implica aproximadamente el 30-40% de la muestra.

El sistema $La_{0.7}Ca_{0.3}MnO_3$//$BaTiO_3$ exhibe momentos magnéticos de saturación deprimidos, una transición de la fase paramagnética a la ferromagnética ancha, altos campos coercitivos que dependen linealmente de la temperatura, y una temperatura de bloqueo alta (típicamente 120K). Además, se han observado ciclos magnéticos de tipo Matteucci en el rango de temperaturas que va de 40K a 150K indicando dos aspectos relevantes en este sistema: 1) una importante parte de los espines no observados en saturación, no ferromagnéticos, participan activamente en las propiedades generales de estas láminas delgadas, y 2) debido al alto nivel de *strain*, el origen de estas anomalías está relacionado con la energía magnetoelástica que es relativamente más alta (Capítulo 5). De forma consistente, se han observado alta electroresistencia y una segunda transición metal-aislante de carácter percolativo en el mismo intervalo de temperaturas, indicando la coexistencia de dos fases magnéticas de $La_{0.7}Ca_{0.3}MnO_3$ (Capítulo 6).

ACOPLO MAGNETOELÁSTICO

Para estudiar el acoplo magnetoelástico en las muestras de $La_{0.7}Ca_{0.3}MnO_3$//$BaTiO_3$ recurrimos a las técnicas de Reflectometría de Neutrones Polarizados (PNR) y Resonancia Ferromagnética (FMR), y a la teoría de anisotropía magnética (Capítulo 7), que en estas muestras predice alta energía magnetoelástica, dado que el *strain* en $La_{0.7}Ca_{0.3}MnO_3$//$BaTiO_3$ es mayor que el 1%.

Se han analizado los datos de FMR utilizando densidades de energía de anisotropía magnética, lo que nos ha permitido relacionar los espectros medidos con el acoplo magnetoelástico. Para ello utilizamos un modelo sencillo de dos láminas con diferentes constantes de anisotropía. Una lámina relajada (con bajo *strain*) con constantes de anisotropía similares a aquellos medidos en las muestras de control crecidas sobre $SrTiO_3$. Y una segunda lámina, que está localizada cerca de la interface con el sustrato y que, por tanto, está muy afectada por el *strain*. Considerando esta estructura vertical con parámetros extraídos del análisis de PNR, realizamos simulaciones de los mapas de FMR que describen de forma satisfactoria los espectros de FMR medidos.

El éxito de este sencillo modelo para explicar los espectros de FMR es considerado como una confirmación del fuerte acoplo magnetoelástico entre lámina delgada y sustrato. Además, el acoplo magnetoelástico puede estar en el origen de la formación de la segunda fase magnética en el $La_{0.7}Ca_{0.3}MnO_3$ (Capítulos 5 y 6), favorecida por la tendencia de esta manganita a la segregación de fases. Aunque la observación directa de esta segunda fase magnética ha sido imposible, debido probablemente a su carácter de corto alcance, el ordenamiento antiferromagnético cerca de la interfaz puede estar en el origen de la anisotropía negativa medida en FMR y explicar a su vez la gran resistencia observada a bajas temperaturas. Los ciclos de histéresis de tipo Matteucci pueden tener su origen en la interacción entre estas dos fases magnéticas en un proceso magnetostrictivo que debe implicar espines localizados en la interfaz entre momentos ferromagnéticos y antiferromagnéticos.

ACOPLO MAGNETOELÉCTRICO

El carácter multiferroico de las láminas de $La_{0.7}Ca_{0.3}MnO_3$ sobre $BaTiO_3$ resulta clave para entender la fenomenología observada. En este sistema hemos podido observar el acoplo magnetoeléctrico entre lámina ferromagnética y sustrato ferroeléctrico con constantes de acoplo magnetoeléctrico α del orden de $(2\text{-}5)\cdot 10^{-7}$ s/m (Capítulo 8). Este acoplo afecta a cerca del 50 % de los momentos implicados, a bajas temperaturas. Dos factores determinan la magnitud de este efecto: 1) el cambio de *strain* entre lámina y sustrato y 2) la calidad del sustrato. En $BaTiO_3$, estos dos factores están relacionados. Al usar sustratos pre-poleados, principalmente con dominios de tipo "c", se observaron mayores constantes de acoplo magnetoeléctrico y el efecto es más reproducible. Esto es debido a que estos sustratos son en general de mayor calidad y tiene mayores dominios ferroeléctricos. A esto hay que sumar el hecho de que se mantenía fijado el campo eléctrico aplicado durante el proceso de enfriado de las muestras hasta llegar a la fase romboédrica del sustrato de modo que este estado cercano al de "mono-dominio" se puede conservar, favoreciendo al mismo tiempo el mecanismo de rotación de la polarización ferroeléctrica en vez del de rotación de dominios. Este mecanismo de polarización ferroeléctrica implica *strains* mayores que 1 %, explicando así la magnitud del efecto observado. En contraposición a esto, las muestras crecidas sobre sustratos no polarizados de $BaTiO_3$ exhiben un efecto mucho menor con $\alpha \approx 10^{-8}$ s/m. De nuevo, la explicación reside en la naturaleza del sustrato: los dominios ferroeléctricos son mucho más pequeños en sustratos no polarizados y, en consecuencia, el proceso de polarización está dominado por rotación de dominios y efecto piezoeléctrico intrínseco, resultando en *strains* piezoeléctricos mucho menores del 1 %.

En definitiva, el efecto magnetoeléctrico medido en las muestras de $La_{0.7}Ca_{0.3}MnO_3$//$BaTiO_3$ está mediado por el *strain* y su magnitud depende estrechamente del proceso de polarización ferroeléctrica dominante en el sustrato, y este, a su vez, depende de la calidad del sustrato. Solamente utilizando sustratos de $BaTiO_3$ de gran calidad es posible alcanzar cambios de *strain* suficientemente altos como para mejorar el efecto magnetoeléctrico, ya que solo en estos casos, es posible aprovechar el *strain* piezoeléctrico alcanzable cuando el campo eléctrico es aplicado en direcciones distintas a la dirección de polarización espontánea del sustrato.